Failure Prediction of Fiber Reinforced Composites Using Reduced Order Multiscale Models

By

Michael James Bogdanor

Dissertation

Submitted to the Faculty of the

Graduate School of Vanderbilt University

in partial fulfillment of the requirements

for the degree of

DOCTOR OF PHILOSOPHY

in

Civil Engineering

December, 2015

Nashville, Tennessee

Approved:

Dr. Caglar Oskay

Dr. Douglas Adams

Dr. Prodyot K. Basu

Dr. Stephen B. Clay

Dr. Haoxiang Luo

Dr. Sankaran Mahadevan

To my loving and supportive wife, Merissa,

for endeavoring on this journey with me

and our wonderful daughter, Mikayla,

for bringing us more joy than I could have imagined.

ACKNOWLEDGMENTS

First, I would like to thank my advisor, Dr. Caglar Oskay, for his consistent and valuable guidance and advice. Thank you for bringing me into your research group, guiding me through the fellowship application process, and entrusting me with exciting research projects to pursue. I owe a debt of gratitude to the members of the Multiscale Computational Mechanics Laboratory for their friendship and helpful critique of this work. Thank you to Dr. Robert Crouch for the strong foundation of work you set before me and for passing on the torch of this project.

Thank you to Dr. Stephen Clay of the Air Force Research Laboratory for your collaboration, for granting us the flexibility in the research paths we pursued, and for supporting our research with invaluable experimental data. I would also like to thank Philip Knoth from the AFRL for performing the experiments and providing expertise in interpreting that data which greatly enriched this work. I gratefully acknowledge the financial support provided by the Aerospace Systems Directorate of the Air Force Research Laboratory and the Department of Defense through the National Defense Science & Engineering Graduate Fellowship Program.

I would like to thank Drs. Adams, Basu, Luo, and Mahadevan for serving on my doctoral committee and for the guidance, motivation, and direction they have provided in the completion of this dissertation. Thank you Dr. Basu for encouraging me to finish my half-completed application to Vanderbilt and be able to join this great institution and its incredible staff, faculty, and students. Thank you Dr. Mahadevan for presenting statistics and probabilistic analysis in a new way that finally started to click with me and for your help on the uncertainty quantification aspects of this work. Dr. Adams, thank you for taking the time to encourage me on the broader aspects of this work and for starting me on the path to my next endeavor with IACMI. Dr. Luo, it has been a pleasure sharing an office with you and your group for the past few years - thank you for the diverse perspective you bring to my research. Thank you as well to Beverly Piatt, Karen Fuller, and Karen Page for all of your administrative help throughout my time at Vanderbilt.

To my father, Dr. James Bogdanor and mother, Lyric Bogdanor, thank you for raising me to

pursue my endeavors with hard work and diligence, for instilling a love for mathematics, problem solving, and engineering, and for providing a great environment for me to grow up and thrive in. Thank you to my brother, Joshua Bogdanor, for being my role model and always supporting and encouraging me. Mike and Annette, thank you for your interest in my work, for encouraging me, and supporting our family through this chapter. Thank you as well to our friends in Nashville who have made this town a home that we are not eager to leave. In particular, thank you to Andrew Smith for your friendship and curiosity in my work, my ability to communicate what I do would be greatly diminished if it were not for our conversations.

Merissa, my wife, thank you for all the support you have given me through this journey. I greatly appreciate your willingness to follow me to Nashville to pursue this degree, for always loving me and encouraging me, and for the hard work you have put into our home and our family. Thank you for putting up with the challenges of working from home with a toddler and all of the traveling for your work which allowed me to complete my graduate studies. Thank you Mikayla for giving me the encouragement to get this dissertation done.

TABLE OF CONTENTS

LIST OF TABLES

LIST OF FIGURES

Chapter 1

INTRODUCTION

1.1 Motivation

Fiber reinforced polymer (FRP) composites present a significant opportunity for increasing performance and improving energy efficiency in a number of technology sectors, most notably the automotive and aerospace industries. While great strides have been made in the advancement of FRP materials in recent years, widespread application of these composite materials has been elusive. This is in part due to the high costs of manufacturing and material research required to characterize new material systems. The flexibility of composite design is both a boon and a bane to development of these materials. The highly customizable nature of the composite allows for tailored design and nearly limitless configurations to meet the specific requirements of a given application. This, however, leads to a limited amount of direct carryover from the behavior of one composite system to another, at least in terms of traditional mechanical and statistical approaches. Furthermore, reliability studies, which require a large amount of experimental data in order to accurately describe the probabilistic nature of a given material system, exacerbate the costs of development as each new material system requires its own extensive set of experiments to define stochastic and low-probability effects. While two separate composite material systems could be comprised of the same constituent materials, differences in composite layup and microstructural characteristics, such as fiber volume fraction, often lead to dramatically different material behaviors. Better predictive modeling capabilities are required to accurately discern the behavior of the composite material system based on its constituent materials and the morphology of the composite, rather than relying solely on homogeneous material behavior, such as that which defines metals. This would allow experiments of different material systems to be more effectively compared and utilized in the characterization of new composites. The improved ability to define the effective

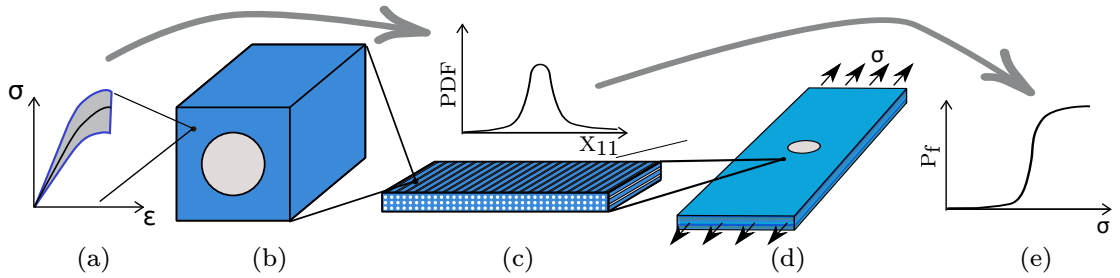

Figure 1.1: Multiple Scales of Composite Materials: a) Random Constituent Material, b) Representative Volume Element, c) Single Ply or Lamina with Random Effective Composite Properties, d) Laminate or Component, e) Failure Probability of Component Subjected to Random Load.

composite response from the constituent materials and composite morphology will allow greater synergy between the design and characterization of composite materials, increasing predictive accuracy and reducing the costs associated with material development.

Failure prediction of composite materials is an inherently multiscale problem from the mechanical and probabilistic standpoints. The physical mechanisms that govern failure in composites operate at multiple spatial scales. For instance, diffuse damage in the form of microcracks and voids incubates at the scale of the material's microstructural constituents, grows and coalesces at the scale of the mesostructure (i.e., representative volume (RVE)), and ultimately leads to failure at the scale of the macrostructure (i.e., a coupon or component). An illustration of the physical size scales in an FRP composite is given in Figure 1.1, along with the associated probabilistic effects at each scale. Accurate and reliable predictions of composite material performance require methods of communicating information between these disparate scales of interest, while maintaining computational efficiency. In this dissertation, a multiscale modeling approach is presented which utilizes computational homogenization with reduced order microscale models to predict the performance of FRP composites under static and fatigue loading, as well as a probabilistic approach for calibrating constituent material properties from random lamina and laminate scale information.

1.2 Literature Review

It is readily apparent that the constituent materials that make up the microstructure of a heterogeneous material directly impact the structural performance of the composite. Early predictive methods for fiber reinforced composites relied on analytical methods to determine composite effective stiffness and failure criteria at the lamina scale. Many effective stiffness methods such as the Mori-Tanaka method [65], Hashin-Shtrikman bounds [41], and the self-consistent method [43] have been presented, along with failure criteria for the anisotropic plies such as the maximum stress, maximum strain, Hoffman [44], Tsai-Hill [101], Tsai-Wu [102], and Chamis criteria [22]. Such analytical methods represent a pseudo-multiscale approach in that there is no concurrent analysis of the micro- and macroscales. While these methods rely on information regarding the strength of the constituent materials and can include the type of failure associated with a loading state, they lack a high degree of resolution to microscale phenomena.

Multiscale computational modeling has shown tremendous promise for failure prediction of composite materials and structures. While a number of mathematically robust multiscale computational modeling methodologies have been proposed (e.g., the multiscale finite element method [46], generalized method of cells [1], and Voronoi cell finite element method [38]), computational homogenization (CH) based methods remain among the most popular [34]. Rooted in the mathematical homogenization theory [12, 13, 97, 85], CH has been employed to study failure in various composite material applications [98, 36, 64, 52, 47, 104]. In CH based approaches, the response at the scale of the composite RVE or the unit cell is strongly coupled to the macroscopic structure and the two scales are numerically evaluated in a concurrent fashion. Since these approaches rely on explicit resolution of the material microstructure and numerical treatment of the fine scale, composites with arbitrarily complex microstructures (e.g., woven, braided, 3D textile, etc.) can be modeled within the same framework. One important drawback of CH is that it is computationally very expensive and evaluation of large structural systems using direct CH is typically not feasible.

The eigendeformation-based homogenization method (EHM) [70, 26] is a CH based modeling approach that has been developed to overcome the issue of high computational cost. EHM is rooted

in the transformation field analysis pioneered by Dvorak and coworkers [30, 31], and employs the idea of precomputing certain microstructural information, (e.g., localization operators, concentration tensors, and influence functions) collectively referred to as the coefficient tensors, before the progressive damage and failure analysis at the scale of a structural subelement, element or a component. The nonlinear microstructural analyses (defined over a unit cell or an RVE), which are coupled to the structural analysis, are then concurrently evaluated for a small subset of unknowns. The precomputed coefficient tensors, along with the state variables evaluated on-the-fly, are employed to upscale (homogenize) or downscale (localize) the stress and strain fields. EHM can also account for progressive debonding between fiber and matrix at the scale of the microstructure, and is equipped with an adaptive model improvement capability to hierarchically increase model fidelity during a simulation [70]. EHM has been successfully employed in the prediction of failure under static loading [27, 16], blast [47], compression-after-impact [104], and fatigue loading [28], as well as failure in thin composite plates [72, 68], and in the presence of environmental effects [53].

Robust predictive models for composite material performance not only require accurate modeling strategies, but also the ability to account for the presence of uncertainty in material behavior at multiple scales. Natural material variability and manufacturing process-induced defects at each size scale cause composites to exhibit significant variations in structural strength, failure response and other mechanical properties. For instance, defects within the microstructural constituents (i.e., matrix and fiber); variability in the morphology at the scale of the RVE; and ply misalignment, thickness variability and interlaminar defects at the lamina scale all lead to the uncertainty and randomness observed at the macroscale of the composite. A number of approaches have been proposed in the literature for the incorporation and propagation of uncertainty across these spatial scales. A comprehensive overview of the literature in this area is presented by Sriramula and Chryssanthopoulos in Reference [96]. The effect of random constituent elastic properties on the effective composite elastic moduli has been investigated by Kamiński and Kleiber [50] and Sakata et al. [83] using the stochastic finite element method (SFEM). Shaw et al. [88] estimated effec-

tive composite properties based on random constituent strength and stiffness using Monte Carlo (MC) simulation and applied first and second order reliability methods (FORM and SORM) to predict the failure of a laminated plate based on the Tsai-Hill failure criterion. Reliability of laminated composites based on random composite properties and layer thicknesses was investigated using SFEM and MC, β, and first order second moment reliability methods [60], the Edgeworth expansion method [55], and FORM and MC with trained neural networks [62].

In the context of multiscale computational methods, the variability in the composite response at the lamina scale can be propagated up from the microstructure using methods such as the Δ-criterion [40], the non-concurrent multiscale stochastic method [25], and perturbation based stochastic finite elements [89, 23], as well as homogenization-based methods such as the generalized method of cells [1], stochastic finite elements [50], perturbation-based homogenization [82], and multiscale spectral stochastic method [100], among others. CH provides a rigorous basis for linking the fine and coarse scale response of heterogeneous and composite materials, and as such provides a strong foundation for investigating the effects of uncertainty at multiple spatial scales. While the extensions of CH to compute the variability in homogenized elastic properties from known variability at the scale of the microstructure to study stochastic problems have been proposed [50, 82, 100], the application of this approach to study the uncertainty in inelastic behavior and failure properties has proven more difficult. This difficulty is largely computational – additional dimensions introduced into the problem by the random treatment of microstructural material and morphological parameters lead to computational intractability when the material response includes damage and nonlinearity. The EHM method presents a multiscale CH approach with the computational efficiency to account for the added computational expense in the probabilistic analysis.

In each of the previously discussed probabilistic studies, the propagation of uncertainty is a forward problem, where uncertainty at smaller scales leads to randomness at the larger scales. However, the propagation of uncertainty from larger scales, such as homogeneous effective composite properties, to randomness in the constituent materials has not received much attention. Whereas

deterministic calibration of constituent material properties in composites has been conducted in a number of investigations using gradient-based and genetic algorithm approaches [71, 33], these calibration methods, however, do not capture the uncertainty in constituent properties coming from the natural variability of the material, sparse data, errors in the model, or the possibility of multiple solutions due to the nonlinearity of the model. In contrast to the deterministic approach, Bayesian calibration is able to quantify the uncertainty in the model parameters based on sparse and incomplete date from multiple sources [79, 105]. Due to the high costs of manufacturing composite materials, large experimental data sets are either non-existent or not available for public access. As such, data which is available tends to be limited to a small number of replicates over a suite of different experiments. Resources are typically allocated to characterize a wide range of physical characteristics, and not necessarily account for stochastic effects. While it is difficult to accurately quantify randomness over a small number of replicates for a single test, when the data is able to be considered on aggregate, better quantification of randomness can be achieved.

Bayesian calibration methods can utilize this data from multiple sources and include point data, interval data, data on statistical distributions, or any combination of these. Bayesian methods are also desirable due to their ability to quantify uncertainty from sources beyond model parameter uncertainty, including model form uncertainty, solution approximation error, and measurement error. Markov chain Monte Carlo (MCMC) simulation is commonly used in implementing Bayesian calibration. Several MCMC algorithms are available, such as the Metropolis-Hastings algorithm [63, 42], Gibbs sampling [37], and slice sampling [66]. MCMC simulation requires several thousands of sets of samples to be evaluated using the numerical model. It quickly becomes computationally impractical to evaluate a finite element model for each set of input parameters required in the calibration process, and therefore a surrogate model must be introduced. The surrogate model approximates the predicted response of the original model using an inexpensive function. Gaussian Process (GP) modeling is a popular choice due to its versatility in handling nonlinear relationships and the ability to estimate prediction uncertainty in the model [86, 45, 77]. In GP models, the prediction output is a Gaussian random field, defined by a mean and covariance function. Imple-

menting Bayesian calibration within the framework of the EHM multiscale approach represents a robust approach to accurately characterizing composite material reliability, which is dependent both on the physical phenomenology of the material and the stochastic effects which are present.

1.3 Research Objectives

The goal of this dissertation is to advance the state of the art in composite life prediction in the following areas:

1. gain additional fundamental understanding on the way in which microscale failure is propagated to discrete lamina and laminate failure in FRP composites,
2. predict the mechanical response of multiple FRP composites laminates under a range of static and fatigue loading conditions, and
3. quantify the effect of random constituent material properties of FRP composites on effective composite properties and laminated composite behavior.

1.4 Dissertation Organization

In Chapter 2, the continued development of the EHM multiscale model is presented. Amongst the novel contributions to this method presented are the development of an approach to address the tension-compression stiffness anisotropy in unidirectional FRP tape and a novel parameter weighting approach to capture the disparate damage evolution characteristics under uniaxial and shear loading. The development of these methods was essential to extending the predictive capability of the EHM approach to concurrently predict laminated composite response under tension, compression, and shear loading conditions, which satisfies the first research objective. Additionally, the computational improvements gained by transitioning the EHM code from a serial to a parallel implementation are discussed. The second research objective is accomplished in Chapter 3, which presents the blind prediction of static and fatigue performance of laminated IM7/977-3 composites using the EHM approach. The results in Chapter 3 represent the first application of the EHM

model with a single set of consistent material parameters to predict shear, compression, tension, and delamination behavior. Two additional layups which had not previously been considered using the EHM approach were included as well. The third research objective is addressed in Chapters 4 and 5. In Chapter 4, the methods employed in the Bayesian model parameter calibration approach within the multiscale computational framework are presented. Chapter 5 demonstrates the proposed probabilistic framework in the calibration of random constituent material parameters from lamina scale experimental data using Bayesian calibration and predicts the probabilistic behavior of laminate composite specimens subject to strain rate dependence effects. This probabilistic calibration study is a novel approach to parameter calibration applied to laminated composite materials. Conclusions from this research and suggestions for future research are provided in Chapter 6.

Chapter 2

MULTISCALE PROGRESSIVE DAMAGE ACCUMULATION MODEL

One of the primary challenges in the prediction of composite material behavior is in accurately accounting for the complexity in which the accumulation of damage occurs. FRP composites exhibit damage in a significantly different manner than metals. In a laminated composite, many interacting failure modes can be present, as seen in Fig. 2.1. Three primary modes of damage accumulation are witnessed in laminated composite specimens - matrix cracking, delamination, and fiber failure. Matrix cracking is an in-plane failure of the weaker matrix material, and is indicted by fine white striations in the X-ray images. In the case of 0° plies, in which the fiber is oriented in the loading direction, matrix cracking is often referred to as "fiber splitting" in that in-plane transfer of load is inhibited due to the crack. Delamination, which presents as a wider white region, indicates the failure of the matrix material between two adjacent plies in the laminate. Fiber failure is the breakage of the reinforcing material in the composite, and typically occurs shortly preceding global failure. Each of these failure modes initiates at the scale of the heterogeneity between constituent materials, or the *microscale*. In contrast, structural performance or the behavior of experimental coupons is typically measured at the *macroscale* where the material exhibits more homogeneous characteristics. This disparity between scales necessitates a multiscale analysis method which is able to provide meaningful results at the macroscale while retaining fidelity to the microscale behavior. This multiscale problem setting is discussed in Section 2.1.

In classical computational homogenization, the effective composite stress-strain behavior at a quadrature point of a nonlinear macroscale analysis is not available in closed form, but is computed by numerically solving a boundary value problem defined over the RVE or unit cell of the composite. No explicit failure criteria is defined at the lamina or laminate scale, but rather, macroscale failure is a consequence of the coalescence of damage in the constituent materials within the microstructure. Due to the nonlinearity of the constituents induced by damage accumulation, each

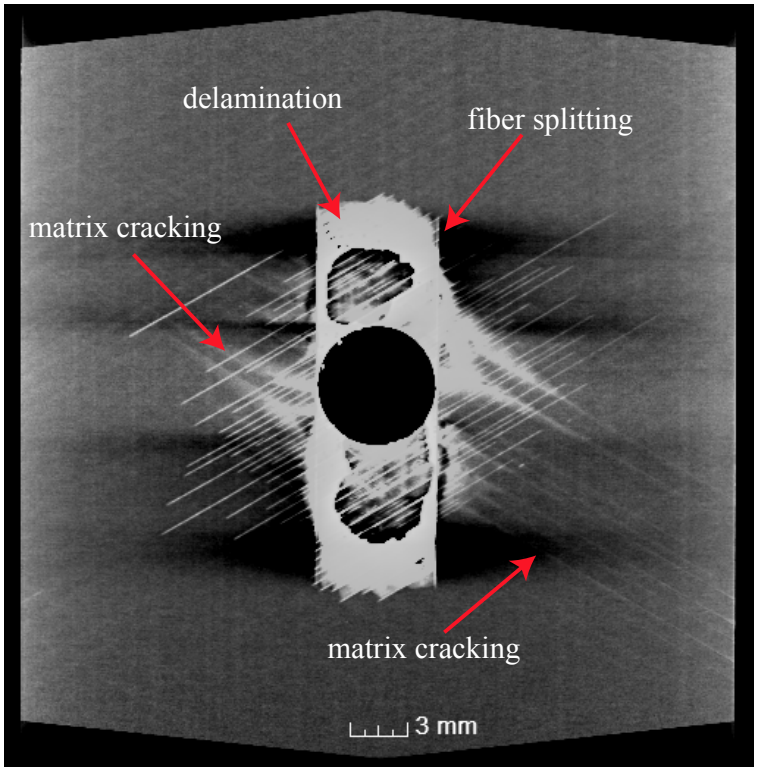

Figure 2.1: X-ray CT Image of Damage in a $[60,0,-60]_{3S}$ Specimen After Fatigue.

quadrature point of the macroscale mesh is associated with a separate RVE, within which equilibrium and damage evolution must be evaluated, stored, and passed on to the solver of the macroscale problem. EHM introduces a reduced order approximation to the microstructure problem, where a much reduced approximation basis is employed compared to a standard direct numerical (e.g. finite element) solution [26, 29]. The resulting system is computationally much more efficient since the number of unknowns associated with the numerical solution of the microscale RVE problem is much larger than the algebraic system size. Section 2.2 presents the overview of the multiscale EHM method. Furthermore, the fatigue analysis of a laminated composite specimen is not only multiscale in space, but also in time. As such, multitemporal homogenization is also required to predict fatigue life performance, as direct analysis of all loading cycles is a computationally intractable problem. This time stepping approach is described in Section 2.2.1. In order to model the progressive growth of damage, continuum damage mechanics (CDM) is employed. CDM has been previously implemented with good results both at the macroscale [78, 21, 94] and more recently at

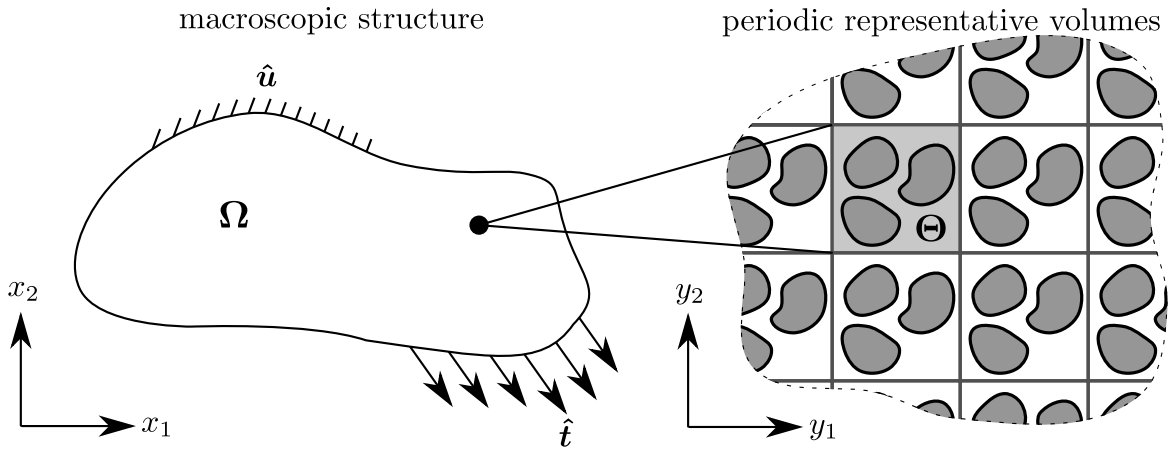

Figure 2.2: Schematic Illustration of the Composite Volume.

the microscale [57]. The mathematical forms of damage evolution employed within this work are presented in Section 2.3. Additional details of the computational implementation of these methods are included in Section 2.4.

2.1 Multiscale Problem Setting

Consider a macroscopic domain of interest, $\boldsymbol{\Omega} \subset \mathbb{R}^d$ ($d = 2$ or 3 indicates the number of spatial dimensions), made of a heterogeneous, periodically repeating microscale RVE, $\boldsymbol{\Theta} \subset \mathbb{R}^d$, which consists of two or more constituent material phases. The macroscale domain is parameterized by the spatial coordinate, $\mathbf{x}$. The scale of material heterogeneity is captured by introducing a scaled coordinate system, $\mathbf{y} = \mathbf{x}/\zeta$, to parameterize the microscale, in which $0 < \zeta \ll 1$ is the scaling parameter. This multiscale structure is schematically illustrated in Fig. 2.2. The failure response of the structure under quasi-static conditions (i.e. inertial effects are taken to be small and therefore ignored) is governed by equilibrium, the constitutive relationship, and strain-displacement relationship, respectively, as follows:

$$\nabla \cdot \boldsymbol{\sigma}(\mathbf{x}, \mathbf{y}, t) + \mathbf{b}(\mathbf{x}, \mathbf{y}) = 0 \tag{2.1}$$

$$\boldsymbol{\sigma}(\mathbf{x}, t) = \Big[1 - \omega(\mathbf{x}, \mathbf{y}, t)\Big]\mathbf{L}(\mathbf{y}) : \boldsymbol{\epsilon}(\mathbf{x}, \mathbf{y}, t) = \mathbf{L}(\mathbf{y}) : \Big[\boldsymbol{\epsilon}(\mathbf{x}, \mathbf{y}, t) - \boldsymbol{\mu}(\mathbf{x}, \mathbf{y}, t)\Big] \tag{2.2}$$

$$\boldsymbol{\epsilon}(\mathbf{x}, \mathbf{y}, t) = \nabla^s \mathbf{u}(\mathbf{x}, \mathbf{y}, t) \tag{2.3}$$

in which $\boldsymbol{\sigma}$ is the Cauchy stress, t the time coordinate, $\mathbf{b}$ the body force, ω the scalar damage variable such that $\omega \in [0, 1)$, $\mathbf{L}$ the tensor of elastic moduli, $\boldsymbol{\epsilon}$ the total strain, $\boldsymbol{\mu} = \omega\boldsymbol{\epsilon}$ the inelastic strain, and $\mathbf{u}$ the displacement field. $\nabla \cdot (\cdot)$ and $\nabla^s(\cdot)$ are the divergence and symmetric gradient operators, respectively. The macroscale domain is subjected to the boundary conditions:

where $\hat{\mathbf{u}}$ and $\hat{\mathbf{t}}$ are the prescribed displacements and tractions on the boundaries $\boldsymbol{\Gamma}_{\mathrm{u}}$ and $\boldsymbol{\Gamma}_{\mathrm{t}}$ with $\boldsymbol{\Gamma} = \boldsymbol{\Gamma}_{\mathrm{u}} \cup \boldsymbol{\Gamma}_{\mathrm{t}}$ and $\boldsymbol{\Gamma}_{\mathrm{u}} \cap \boldsymbol{\Gamma}_{\mathrm{t}} = \emptyset$, and $\mathbf{n}$ is the unit normal to $\boldsymbol{\Gamma}$; t_f is the time to failure.

Equation 2.2 implies a damage-elastic constitutive behavior for the composite constituents. In the functional form,

$$\dot{\omega}(\mathbf{x}, \mathbf{y}, t) = f_{\omega}(\boldsymbol{\sigma}(\mathbf{x}, \mathbf{y}, t), \boldsymbol{\epsilon}(\mathbf{x}, \mathbf{y}, t), \mathbf{s}(\mathbf{x}, \mathbf{y}, t); \boldsymbol{\psi}(\mathbf{y})). \tag{2.4}$$

where the superimposed dot indicates the derivative with respect to time, $\mathbf{s}$ is the set of internal state variables which dictate the history dependence of damage evolution, and $\boldsymbol{\psi}$ are the material constituent parameters, which govern the damage evolution law. The form for the damage evolution, f_{ω}, is discussed in Section 2.3.

In the multiscale system, response fields (i.e. stress, strain, inelastic strain, and damage) fluctuate at the scale of the microstructure due to the heterogeneity of the constituent materials in $\boldsymbol{\Theta}$. The response fields are written in terms of both macroscale and microscale coordinates as:

$$\varphi(\mathbf{x}, t) = \hat{\varphi}(\mathbf{x}, \mathbf{y}(\mathbf{x}), t) \tag{2.5}$$

in which φ denotes an arbitrary response field. The displacement field is decomposed through a two-scale asymptotic expansion with contributions from micro- and macroscopic scales as:

$$\mathbf{u}(\mathbf{x}, \mathbf{y}, t) = \bar{\mathbf{u}}(\mathbf{x}, t) + \zeta \mathbf{u}^1(\mathbf{x}, \mathbf{y}, t) \tag{2.6}$$

where $\bar{\mathbf{u}}$ is the macroscopic displacement field and $\mathbf{u}^1$ is the microscopic displacement field. Asymptotic expansion of the displacements allows the micro- and macroscale problems to be posed in a separate, but coupled manner.

Considering the strain-displacement relationship in Equation 2.3, the overall strain field con-

tains contributions from the macroscale strain state and the locally fluctuating microscale strains,

$$\boldsymbol{\epsilon}(\mathbf{x},\mathbf{y},t) = \bar{\boldsymbol{\epsilon}}(\mathbf{x},t) + \nabla_y^s \mathbf{u}^1(\mathbf{x},\mathbf{y},t) \tag{2.7}$$

where ∇_y^s denotes the symmetric gradient operator with respect to the microscopic coordinates and $\bar{\boldsymbol{\epsilon}}$ is the macroscale strain obtained by spatial averaging of the microscale strain field over the RVE:

$$\bar{\boldsymbol{\epsilon}}(\mathbf{x},t) = \frac{1}{|\boldsymbol{\Theta}|}\int_{\boldsymbol{\Theta}} \boldsymbol{\epsilon}(\mathbf{x},\mathbf{y},t)d\mathbf{y} \tag{2.8}$$

in which $|\boldsymbol{\Theta}|$ is the volume of the RVE. Equation 2.8 is a consequence of the periodicity of the response fields (e.g. $\mathbf{u}^1$) over the boundaries of the microstructural domain. Using the damage-elastic constitutive law in Equation 2.2, the stress in the microscale is given as:

$$\boldsymbol{\sigma}(\mathbf{x},\mathbf{y},t) = \mathbf{L}(\mathbf{y}) : \left[\bar{\boldsymbol{\epsilon}}(\mathbf{x},t) + \nabla_y^s \mathbf{u}^1(\mathbf{x},\mathbf{y},t) - \boldsymbol{\mu}(\mathbf{x},\mathbf{y},t)\right] \tag{2.9}$$

in which the tensor of elastic moduli is taken to vary as a function of the microscopic coordinate only. The homogenized macroscale stress is expressed as:

$$\bar{\boldsymbol{\sigma}}(\mathbf{x},t) = \frac{1}{|\boldsymbol{\Theta}|}\int_{\boldsymbol{\Theta}} \boldsymbol{\sigma}(\mathbf{x},\mathbf{y},t)d\mathbf{y}. \tag{2.10}$$

Substituting the displacement decomposition and strain and stress expressions into the equilibrium equation (Equation 2.1), along with the scaling relationship, the equilibrium equations at $\mathcal{O}(\zeta^{-1})$ and $\mathcal{O}(1)$ are obtained:

$$\mathcal{O}(\zeta^{-1}): \qquad \nabla_y \cdot \left[\mathbf{L}(\mathbf{x},\mathbf{y}) : [\bar{\boldsymbol{\epsilon}}(\mathbf{x},t) + \nabla_y \mathbf{u}^1(\mathbf{x},\mathbf{y},t) - \boldsymbol{\mu}(\mathbf{x},\mathbf{y},t)]\right] = 0 \tag{2.11}$$

$$\mathcal{O}(1): \qquad \nabla_x \cdot \boldsymbol{\sigma}(\mathbf{x},\mathbf{y},t) = 0 \tag{2.12}$$

Equation 2.11 constitutes the microscale equilibrium equation applied over the domain of the RVE, $\boldsymbol{\Theta}$. Equation 2.12 is averaged over $\boldsymbol{\Theta}$ to obtain the macroscopic equilibrium equation defined over the macroscale problem domain, $\boldsymbol{\Omega}$.

2.2 Eigendeformation Based Homogenization

The above procedure leads to the standard computational homogenization (also known as FE^2) method. While accurate, direct implementation of this approach is computationally costly. Instead, the eigendeformation-based reduced order homogenized method (EHM) originally proposed by Crouch and coworkers in References [26, 29], is employed herein. In the EHM approach, the microscale displacement field is defined by the applied macroscopic strain and the inelastic strain at the microscale as:

$$\mathbf{u}^1 = \mathbf{H}(\mathbf{y}) : \bar{\boldsymbol{\epsilon}}(\mathbf{x}, t) + \int_{\Theta} \mathbf{h}(\mathbf{y}, \hat{\mathbf{y}}) : \boldsymbol{\mu}(\mathbf{x}, \hat{\mathbf{y}}, t) d\hat{\mathbf{y}} \tag{2.13}$$

where $\mathbf{H}$ is the elastic influence function and $\mathbf{h}$ is the phase damage induced influence function obtained from the elastic behavior of the microstructure in the absence and presence of damage, respectively. Numerical Green's functions are employed to compute these influence functions by solving linear-elastic problems defined over the RVE using transformational field analysis [30]. The influence functions are computed prior to a progressive damage analysis since they depend only on elastic properties of constituents and microstructure geometry. In order to achieve the desired model order reduction, the damage-induced inelastic strain fields in the RVE are approximated with coarse shape functions over a small number of subdomains. The RVE domain, $\boldsymbol{\Theta}$, is partitioned into n non-overlapping subdomains, $\boldsymbol{\theta}^{(\gamma)}$, referred to as parts, where $\gamma = 1, 2, \ldots, n$ indicates the part number. These parts comprise the reduced order model (ROM) of the microstructure. Each part is occupied by a single constituent material and the union of all the parts spans the domain, $\boldsymbol{\Theta}$. Phase shape functions, $N^{(\gamma)}$, are defined as piecewise constant functions which form a partition of unity in the RVE (i.e. $N^{(\gamma)} = 1$ if $\mathbf{y} \in \boldsymbol{\theta}^{(\gamma)}$ and 0 otherwise). The inelastic strains and scalar damage values are taken to be constant over a given part - thereby the inelastic strains and scalar damage values at any point in the partitioned microstructure are given by:

$$\boldsymbol{\mu}(\mathbf{x}, \mathbf{y}, t) = \sum_{\gamma} N^{(\gamma)}(\mathbf{y}) \boldsymbol{\mu}^{(\gamma)}(\mathbf{x}, t). \tag{2.14}$$

and

$$\omega(\mathbf{x}, \mathbf{y}, t) = \sum_{\gamma} N^{(\gamma)}(\mathbf{y}) \omega^{(\gamma)}(\mathbf{x}, t). \tag{2.15}$$

where $\boldsymbol{\mu}^{(\gamma)}$ and $\omega^{(\gamma)}$ indicate the inelastic strain and damage value, respectively, associated with part γ. The RVE is partitioned so as to group the similar regions of the microstructure corresponding to the macroscopic failure modes [93]. The specific form of the ROM model implemented in the investigations described in this work is presented in Section 3.1.2.1.

The homogenized macroscale stress is expressed in terms of the macroscale strain, $\bar{\boldsymbol{\varepsilon}}$, the phase averaged damage induced inelastic strains (or eigenstrains), $\boldsymbol{\mu}^{(\alpha)}$, and the phase damage, $\omega^{(\alpha)}$, as:

$$\bar{\boldsymbol{\sigma}} = \sum_{\Delta=1}^{n} \left\{ \left(1 - \omega^{(\Delta)}\right) \left(\mathbf{J}^{(\Delta)} : \bar{\boldsymbol{\varepsilon}} + \sum_{\alpha=1}^{n} \mathbf{H}^{(\Delta\alpha)} : \boldsymbol{\mu}^{(\alpha)} \right) \right\} \tag{2.16}$$

The eigenstrains, $\boldsymbol{\mu}^{(\alpha)}$, are obtained by solving the following nonlinear system of equations:

$$\sum_{\Delta=1}^{n} \left\{ \left(1 - \omega^{(\Delta)}\right) \left(\mathbf{A}^{(\alpha\Delta)} : \bar{\boldsymbol{\varepsilon}} + \sum_{\beta=1}^{n} \mathbf{B}^{(\alpha\Delta\beta)} : \boldsymbol{\mu}^{(\beta)} \right) \right\} = \mathbf{0}, \quad \alpha = 1, ..., n \tag{2.17}$$

in which the coefficient tensors $\mathbf{A}^{(\alpha\Delta)}$, $\mathbf{B}^{(\alpha\Delta\beta)}$, $\mathbf{H}^{(\Delta)}$, and $\mathbf{J}^{(\Delta\alpha)}$ are expressed as:

$$\mathbf{A}^{(\eta\Delta)} = \int_{\Theta^{(\Delta)}} \mathbf{P}_{\intercal}^{(\eta)}(\mathbf{y}) : \mathbf{L}(\mathbf{y}) : (\mathbf{I} + \mathbf{G}(\mathbf{y}))\, d\mathbf{y} \tag{2.18}$$

$$\mathbf{B}^{(\eta\Delta\gamma)} = \int_{\Theta^{(\Delta)}} \mathbf{P}_{\intercal}^{(\eta)}(\mathbf{y}) : \mathbf{L}(\mathbf{y}) : \mathbf{P}^{(\gamma)}(\mathbf{y}) d\mathbf{y} \tag{2.19}$$

$$\mathbf{H}^{(\Delta\gamma)} = \frac{1}{|\Theta|} \int_{\Theta^{(\Delta)}} \mathbf{L}(\mathbf{y}) : \mathbf{P}^{(\gamma)}(\mathbf{y}) d\mathbf{y} \tag{2.20}$$

$$\mathbf{J}^{(\Delta)} = \frac{1}{|\Theta|} \int_{\Theta^{(\Delta)}} \mathbf{L}(\mathbf{y}) : (\mathbf{I} + \mathbf{G}(\mathbf{y}))\, d\mathbf{y} \tag{2.21}$$

$$\mathbf{P}^{(\Delta)}(\mathbf{y}) = \int_{\Theta^{(\Delta)}} \mathbf{g}_{\mathrm{ph}}(\mathbf{y}, \hat{\mathbf{y}}) d\hat{\mathbf{y}} \tag{2.22}$$

where $\mathbf{g}_{\mathrm{ph}}$ and $\mathbf{G}$ are the damage-induced and elastic polarization functions computed from particular solutions of the unit cell problem, $\mathbf{I}$ is the identity tensor, and subscript $\intercal$ denotes the transpose operator. Further details of the derivation and computation of these coefficient tensors for the EHM analysis can be found in Reference [26].

2.2.1 Multitemporal Homogenization

Under cyclic fatigue loading, a microchronological scale exists on the order of a single load cycle and a macrochronological scale exists on the order of the fatigue life of the component. The microtime coordinate is parameterized as $\tau = t/\eta$, where $0 < \eta \ll 1$ is the scaling parameter, similar to that scaling employed in the multispatial homogenization. In microtime, the fast oscillations of the loading cycle lead to damage similar to a static analysis. In macrotime, the accumulation of damage over multiple loading cycles leads to a redistribution of stress through the component, leading to changes in the characteristic nature of damage accumulation macroscopically. For fatigue life analyses on the order of thousands and hundreds of thousands of load cycles, it is infeasible to resolve each microchronological load cycle to follow this stress redistribution. The need to resolve each individual load cycle is eliminated through the use of adaptive cycle-jumping [73, 29]. In the cycle-jumping approach, the rate of damage growth over a single load cycle is used to approximate the rate of damage evolution over subsequent cycles. Adaptive cycle-jumping selects the number of cycles to jump based on comparing the average damage evolution throughout the component for the cycle with a damage criterion. This ensures that the effect of load redistribution is minimal from resolved cycle to resolved cycle and also ensures thermodynamic equilibrium is satisfied throughout the macrotemporal analysis.

Due to the irreversibility of damage evolution over a single step, the traditional concept of periodicity used in multispatial homogenization is not directly applicable to the multitemporal homogenization. Because the change in damage at a material point over a microchronological cycle is taken to be small but non-zero, the response fields over the component are considered to be almost-periodic with respect to the homologous microtemporal point on successive load cycles. In order to upscale the microtemporal response to the macrotemporal scale, a homogenization operator must be employed. In the context of multiple scales in space, a spatial averaging operator is typically used. Due to the cyclic nature of the fatigue loading, it is preferable from a computational standpoint to employ a fixed-point temporal homogenization operator, $\tilde{(\cdot)}$, where for an arbitrary response field, φ, $\tilde{\varphi} = \varphi(\tau^*)$ [28]. In this approach, an arbitrary but fixed point in the

microchronological cycle, τ^* is considered throughout the macrochronological analysis. In what follows, a general description of the boundary value problems solved through coupled multispatial/multitemporal analysis is provided.

Microchronological - microscopic problem: The homogenized macroscale stress is computed as:

$$\bar{\boldsymbol{\sigma}}(\tau,\breve{t}) = \sum_{\Delta=1}^{n}\left[1-\omega^{(\Delta)}(\tau^*,\breve{t})\right]\left[\mathbf{J}^{(\Delta)} : \bar{\boldsymbol{\epsilon}}(\tau,\breve{t}) + \sum_{\alpha=1}^{n}\mathbf{H}^{(\alpha\Delta)} : \boldsymbol{\mu}^{(\alpha)}(\tau,\breve{t})\right], \tag{2.23}$$

in which τ varies over the microchronological scale while t is constant at the fixed macrochronological point (i.e., load cycle), $\breve{t}$, of interest. Due to almost-periodicity, the damage state throughout the microchronological step is taken to be equal to the damage state at the fixed point, τ^*. The evolution of damage with respect to microtime is computed according to the damage evolution law:

$$\omega^{(\gamma)}_{,\tau}(\tau,\breve{t}) = f^1(\boldsymbol{\sigma}(\tau,\breve{t})^{(\gamma)}, \boldsymbol{\epsilon}(\tau,\breve{t})^{(\gamma)}, \mathbf{s}^{(\gamma)}(\tau,\breve{t}), \boldsymbol{\psi}^{(\gamma)}) \tag{2.24}$$

where f^1 is the functional form of damage evolution with respect to microtime.

Microchronological - macroscopic problem: At the macroscale, equilibrium is satisfied over the load cycle as:

$$\nabla\cdot\bar{\boldsymbol{\sigma}}(\mathbf{x},\tau,\breve{t}) = 0; \quad \mathbf{x}\in\boldsymbol{\Omega}; \;\; \tau\in[0,\tau_0] \tag{2.25}$$

Where the applied boundary conditions are represented as:

$$\hat{\mathbf{u}}(\mathbf{x},\tau,\breve{t}) = \hat{\mathbf{u}}^0(\mathbf{x},\breve{t}) + \hat{\mathbf{u}}^1(\mathbf{x},\tau); \qquad \mathbf{x}\in\boldsymbol{\Gamma}_{\mathrm{u}}; \qquad \tau\in[0,\tau_0] \tag{2.26}$$

$$\hat{\mathbf{t}}(\mathbf{x},\tau,\breve{t}) = \hat{\mathbf{t}}^0(\mathbf{x},\breve{t}) + \hat{\mathbf{t}}^1(\mathbf{x},\tau); \qquad \mathbf{x}\in\boldsymbol{\Gamma}_{\mathrm{t}}; \qquad \tau\in[0,\tau_0] \tag{2.27}$$

where $\hat{\mathbf{u}}^0$ and $\hat{\mathbf{t}}^0$ are the slowly varying component of the macroscale displacement and traction boundary conditions over macrotime, and $\hat{\mathbf{u}}^1$ and $\hat{\mathbf{t}}^1$ the fast oscillating components of the displacement and tractions which comprise the loading cycle. As a consequence of almost-periodicity, the solution of the macroscale boundary value problem over microtime reduces to a linear-elastic problem, wherein the stiffness does not change over the microchronological step.

Macrochronological - microscopic problem Over the scale of multiple loading cycles, the

rate of damage evolution with respect to macrotime is given as:

$$\tilde{\omega}_{,t}^{(\gamma)}(t) = f^0(\tilde{\boldsymbol{\sigma}}(t)^{(\gamma)}, \tilde{\boldsymbol{\epsilon}}(t)^{(\gamma)}, \tilde{\mathbf{s}}^{(\gamma)}(t), \boldsymbol{\psi}^{(\gamma)}) + \omega_{\text{ap}}^{(\gamma)}(t) \tag{2.28}$$

where f^0 is the functional form of damage evolution with respect to macrotime and $\dot{\omega}_{\text{ap}}$ is the rate of damage evolution from almost periodicity computed as the amount of damage accumulated over a single microchronological load cycle. Homogenized stress is computed as in Equation 2.23, setting τ to the fixed point τ^* and replacing the stress at an arbitrary τ value, $\bar{\boldsymbol{\sigma}}(\tau, t)$, with the fixed point homogenized stress, $\tilde{\bar{\boldsymbol{\sigma}}}(t)$. In macrotime, because the damage at the fixed point is changing due to the accumulation of almost periodic damage and the long time scale damage evolution, the fixed point inelastic strains will evolve over time. Microscale equilibrium is satisfied as in Equation 2.17, for the fixed point where:

$$\sum_{\Delta=1}^{n} \left\{ \left[1 - \tilde{\omega}^{(\Delta)}(t)\right] \left[\mathbf{A}^{(\alpha\Delta)} : \tilde{\bar{\boldsymbol{\epsilon}}} + \sum_{\gamma=1}^{n} \mathbf{B}^{(\alpha\Delta\gamma)} : \tilde{\boldsymbol{\mu}}^{(\gamma)} \right] \right\} = 0 \quad \forall \alpha = 1, 2, \ldots, n. \tag{2.29}$$

Macrochronological - macroscale problem: In macrotime, equilibrium is satisfied in the presence of evolving damage fields at the microchronological fixed point:

$$\nabla \cdot \tilde{\bar{\boldsymbol{\sigma}}}(\mathbf{x}, t) = 0; \quad \mathbf{x} \in \boldsymbol{\Omega}; \;\; t \in [0, t_f] \tag{2.30}$$

Similarly the boundary conditions are applied at the fixed point:

$$\hat{\mathbf{u}}(\mathbf{x}, t) = \hat{\mathbf{u}}^0(\mathbf{x}, t) + \tilde{\hat{\mathbf{u}}}^1(\mathbf{x}); \qquad \mathbf{x} \in \boldsymbol{\Gamma}_{\text{u}}; \qquad t \in [0, t_f] \tag{2.31}$$

$$\hat{\mathbf{t}}(\mathbf{x}, t) = \hat{\mathbf{t}}^0(\mathbf{x}, t) + \tilde{\hat{\mathbf{t}}}^1(\mathbf{x}); \qquad \mathbf{x} \in \boldsymbol{\Gamma}_{\text{t}}; \qquad t \in [0, t_f] \tag{2.32}$$

As the damage is allowed to evolve at the macrochronological scale, the macrochronological-macroscale problem is a non-linear problem, where thermodynamic consistency is satisfied throughout the macrochronological scale.

2.2.2 Adaptive Cycle Stepping

To improve the computational efficiency of the laminated composite fatigue predictions, adaptive cycle stepping is employed to reduce the number of fully resolved load cycles. Let $\mathbf{D}'(t)$ be the set of all micro-spatial damage accumulation rates, $\omega_m^{(\alpha)}$, computed over a single load cycle:

$$\mathbf{D}'(t) = \begin{bmatrix} \omega_m^{(1)}(\mathbf{x_1}, \mathbf{t}) & \cdots & \omega_m^{(n)}(\mathbf{x_1}, \mathbf{t}) \\ \vdots & \ddots & \vdots \\ \omega_m^{(1)}(\mathbf{x_{n_g}}, \mathbf{t}) & \cdots & \omega_m^{(n)}(\mathbf{x_{n_g}}, \mathbf{t}) \end{bmatrix} \tag{2.33}$$

where n_g is the number of quadrature points over the entire macroscale domain and n is the number of parts in the microscale ROM. A linear macrochronological damage growth is applied starting from the microscale damage state $\mathbf{D}(t_i)$ at time t_i and approximating the damage at time $t_{i+1} = t_i + \Delta t$ as

$$\mathbf{D}(t_{i+1}) = \mathbf{D}(t_i) + \Delta t \mathbf{D}'(t_i) \tag{2.34}$$

The cycle jump, Δt, is adaptively computed at each macrochronological increment such that the mean damage growth over the macrochronological step, $\Delta\bar{\mathbf{D}}(t) = \Delta t\bar{\mathbf{D}}'(t)$ is less than a threshold damage value, D_{max}:

$$\Delta t = \frac{\Delta D_{max}}{\bar{\mathbf{D}}'(t)} \tag{2.35}$$

In this manner, the number of microchonological loading cycles to be jumped in a single macrochronological increment depends on the current state of damage evolution throughout the analysis. When the accumulation of damage over a single loading cycle is low, the adaptive approach jumps over a large number of cycles. When the accumulation of damage in a single cycle is high, the multitemporal analysis resolves a greater number of cycles in order to more fully describe the stress redistribution and damage interaction behavior occurring in the macroscale. For further details on the multichronological time stepping employed, refer to references [29, 27].

2.3 Damage Evolution in Constituent Materials

The primary failure modes in FRP composites are fiber breakage, matrix cracking, and delamination. CDM utilizes internal state variable theory to idealize these failure modes as the accumulation of diffuse microscopic damage within the constituents. A large number of damage evolution models have been proposed in the literature for a variety of materials, see, e.g. the books by Lemaitre [56], Voyiadjis [103], and Kachanov [49]. The fundamental components of the damage evolution frameworks are the state variables which define damage, the physical quantities which drive the damage evolution, and the functional form that relates the "driver" variable to the damage state [20, 91]. Previous works have investigated the behavior of composites using both rate-independent and rate-dependent phenomenological models [91, 3, 2]. Experiments have shown the response of composite materials to exhibit strain-rate dependence under monotonic [76, 99] and fatigue loading [4, 24] for a variety of composite materials. For cases where rate-effects are not considered, however, it is more expedient to use a rate-independent evolution law as fewer parameters are required to be calibrated for the rate-independent model.

2.3.1 Rate Independent Damage Evolution

The evolution of the damage state within part γ of the ROM, $\omega^{(\gamma)}$, is driven by the damage equivalent strain, $\upsilon^{(\gamma)}$, defined as:

$$\upsilon^{(\gamma)} = \sqrt{\frac{1}{2}(\boldsymbol{F}^{(\gamma)}\hat{\boldsymbol{\varepsilon}}^{(\gamma)}) : \hat{\mathbf{L}}^{(\gamma)} : (\boldsymbol{F}^{(\gamma)}\hat{\boldsymbol{\varepsilon}}^{(\gamma)})} \tag{2.36}$$

in which $\hat{\boldsymbol{\varepsilon}}^{(\gamma)}$ is the vector of principal strains within part γ computed as the eigenvalues of the part strain tensor $\boldsymbol{\epsilon}^{(\gamma)}$, $\hat{\mathbf{L}}^{(\gamma)}$ is the rotated elastic moduli tensor for the constituent material in part γ with respect to the principal strains, and $\boldsymbol{F}^{(\gamma)}$ is the strain weighting matrix that accounts for the

tension/compression damage anisotropy. The strain weighting matrix is given as:

$$F^{(\gamma)} = \begin{bmatrix} h_1 & 0 & 0 \\ 0 & h_2 & 0 \\ 0 & 0 & h_3 \end{bmatrix}; \qquad h_\xi = \begin{cases} 1 \text{ if } \hat{\epsilon}_\xi > 0 \\ c^{(\gamma)} \text{ otherwise} \end{cases} \quad \text{for } \xi = 1, 2, 3 \tag{2.37}$$

where $c^{(\gamma)}$ is the tension/compression anisotropy factor for part γ.

The damage potential, Φ, is computed from the damage equivalent strain following the arctangent evolution function [69, 35]:

$$\Phi(\upsilon^{(\gamma)}) = \frac{\arctan(a^{(\gamma)}\langle \upsilon^{(\gamma)} - \upsilon_0^{(\gamma)} \rangle - b^{(\gamma)}) + \arctan(b^{(\gamma)})}{\frac{\pi}{2} + \arctan(b^{(\gamma)})} \tag{2.38}$$

where $a^{(\gamma)}$, $b^{(\gamma)}$ and $\upsilon_0^{(\gamma)}$ control the shape of the damage evolution function and $\langle \cdot \rangle_+$ indicates Macaulay brackets ($\langle \cdot \rangle_+ = \frac{(\cdot)+|\cdot|}{2}$).

A highly non-linear stress-strain response of laminated composites [74, 84] and epoxy resin [39, 61] has been observed under shear loading. This is in contrast to the typically brittle failure of the composite in uniaxial tension. The ductility of the material is controlled by the shape of its damage evolution curve. To account for the discrepancy in damage evolution between shear-dominated and uniaxial-dominated loading, a novel weighting is employed for the parameter controlling the brittleness of failure, $b^{(\gamma)}$, which is computed as:

$$b^{(\gamma)} = k_b b_s^{(\gamma)} + (1 - k_b) b_n^{(\gamma)} \tag{2.39}$$

$$k_b = \frac{\gamma_{max}^{(\gamma)}}{\gamma_{max}^{(\gamma)}/2 + \epsilon_{max}^{(\gamma)}}; \ \in [0, 1] \tag{2.40}$$

where $b_s^{(\gamma)}$ and $b_n^{(\gamma)}$ are parameters controlling strain to failure in part γ for shear and normal loading, respectively, γ_{max} is the maximum engineering shear strain, and ϵ_{max} the maximum absolute principal strain. For purely shear loading, $k_b = 1$, for purely hydrostatic loading, $k_b = 0$.

The rate of damage evolution in the part is defined as:

$$\dot{\omega}^{(\gamma)} = g^p \frac{d\Phi(\upsilon^{(\gamma)})}{d\upsilon^{(\gamma)}} \left\langle \dot{\upsilon}^{(\gamma)} \right\rangle_+ \text{ where } 0 \leq g = \frac{\Phi(\upsilon^{(\gamma)})}{\omega^{(\gamma)}} \leq 1; \quad \gamma = 1, 2, \ldots, n \tag{2.41}$$

where the superimposed dot indicates the first time derivative. The g term is introduced to account for the ratio of the damage potential to the present state of damage at the material point. If the damage potential is equal to or greater than the current state of damage, damage evolves according to the arctangent function. For conditions where $\upsilon^{(\gamma)}$ is increasing, but the damage potential is less than the damage state, such as the case in cyclic loading, damage evolves at a penalized rate governed by the cyclic damage sensitivity parameter, p:

$$p^{(\gamma)} = d_0^{(\gamma)} + d_1^{(\gamma)}\upsilon_{max}^{(\gamma)} + d_2^{(\gamma)}(\upsilon_{max}^{(\gamma)})^2 \tag{2.42}$$

where $d_0^{(\gamma)}$, $d_1^{(\gamma)}$, and $d_2^{(\gamma)}$ are material parameters and $\upsilon_{max}^{(\gamma)}$ is the largest damage equivalent strain value in the part γ experienced over the entire loading history:

$$\upsilon_{\text{max}}^{(\gamma)} = \max_{0\leq\tau\leq t}\{\upsilon^{(\gamma)}(\tau)\}. \tag{2.43}$$

For monotonic loading conditions, i.e. the damage potential is equal to the damage state, Equation 2.41 reduces to:

$$\omega^{(\gamma)} = \Phi(\upsilon_{\text{max}}^{(\gamma)}) \tag{2.44}$$

2.3.2 Rate Dependent Damage Evolution

In cases where it is desired to predict the effect of loading rate-dependence on the performance of structures, an alternative power law damage evolution function is implemented. In the rate-dependent formulation, the accumulation of damage in constituent part $\theta^{(\gamma)}$ is driven by the internal state variables of phase damage equivalent strain, $\upsilon^{(\gamma)}$, and the monotonically increasing phase damage hardening variable, $r^{(\gamma)}$. The damage potential function, Φ_{rd}, is expressed as:

$$\Phi_{rd}(\upsilon^{(\gamma)}, r^{(\gamma)}) = \phi_{rd}(\upsilon^{(\gamma)}) - \phi_{rd}(r^{(\gamma)}) \tag{2.45}$$

in which ϕ_{rd} is the damage evolution function given by the power law relationship

$$\phi_{rd}^{(\gamma)}(v) = a^{(\gamma)}\langle v - \upsilon_0^{(\gamma)}\rangle^{b^{(\gamma)}} \tag{2.46}$$

where $a^{(\gamma)}$ and $b^{(\gamma)}$ are material parameters and v can represent $\upsilon^{(\gamma)}$ or $r^{(\gamma)}$. The parameter $a^{(\gamma)}$ controls the ultimate stress of the material and $b^{(\gamma)}$ controls the ductility of failure. The phase damage equivalent strain, $\upsilon^{(\gamma)}$, is computed as in Equation 2.36. Evolution of the phase damage hardening variable and microscopic damage are expressed as:

$$\dot{r}^{(\gamma)} = \dot{\lambda} \tag{2.47}$$

$$\dot{\omega}^{(\gamma)} = \dot{\lambda}\frac{\partial \phi_{rd}}{\partial \upsilon^{(\gamma)}}. \tag{2.48}$$

For the rate dependent damage law, the consistency parameter $\dot{\lambda}$ is given as:

$$\dot{\lambda} = \frac{1}{q^{(\gamma)}}\left\langle \Phi_{rd}\left(\upsilon^{(\gamma)}, r^{(\gamma)}\right)\right\rangle^{p^{(\gamma)}} \tag{2.49}$$

where $p^{(\gamma)}$ and $q^{(\gamma)}$ are material parameters that govern rate-dependency [91].

2.4 Computational Implementation

2.4.1 Static Prediction Algorithm

Figure 2.3 outlines the computational implementation strategy and procedure for the evaluation of a composite specimen with EHM under static loading. Preprocessing of the composite microstructure is performed using an in house code to generate the parts, the EHM model, and compute the associated coefficient tensors. The inputs to the microstructural analysis are the morphology of the unit cell (e.g., fiber volume fraction, cell type) and the constituent material parameters. The coefficient tensor values and the numerical specimen configuration (i.e., layup, orientations, and mesh) are the inputs to the macroscale finite element analysis performed using the commercially available FEM code, Abaqus. The microscale problem is solved at each quadrature point throughout the macroscale analysis using the user material subroutine (UMAT) functionality. The UMAT computes the homogenized secant stiffness tensor and stress at each point from the macroscale strain given by the FEM solver. Python scripting is utilized to post-process the information present in the Abaqus output database (i.e., *.odb*) files generated from the numerical

simulation. The stress and strain information is extracted from the *.odb* file to produce the stress-strain plots and damage contours are produced through python scripting and the Abaqus GUI.

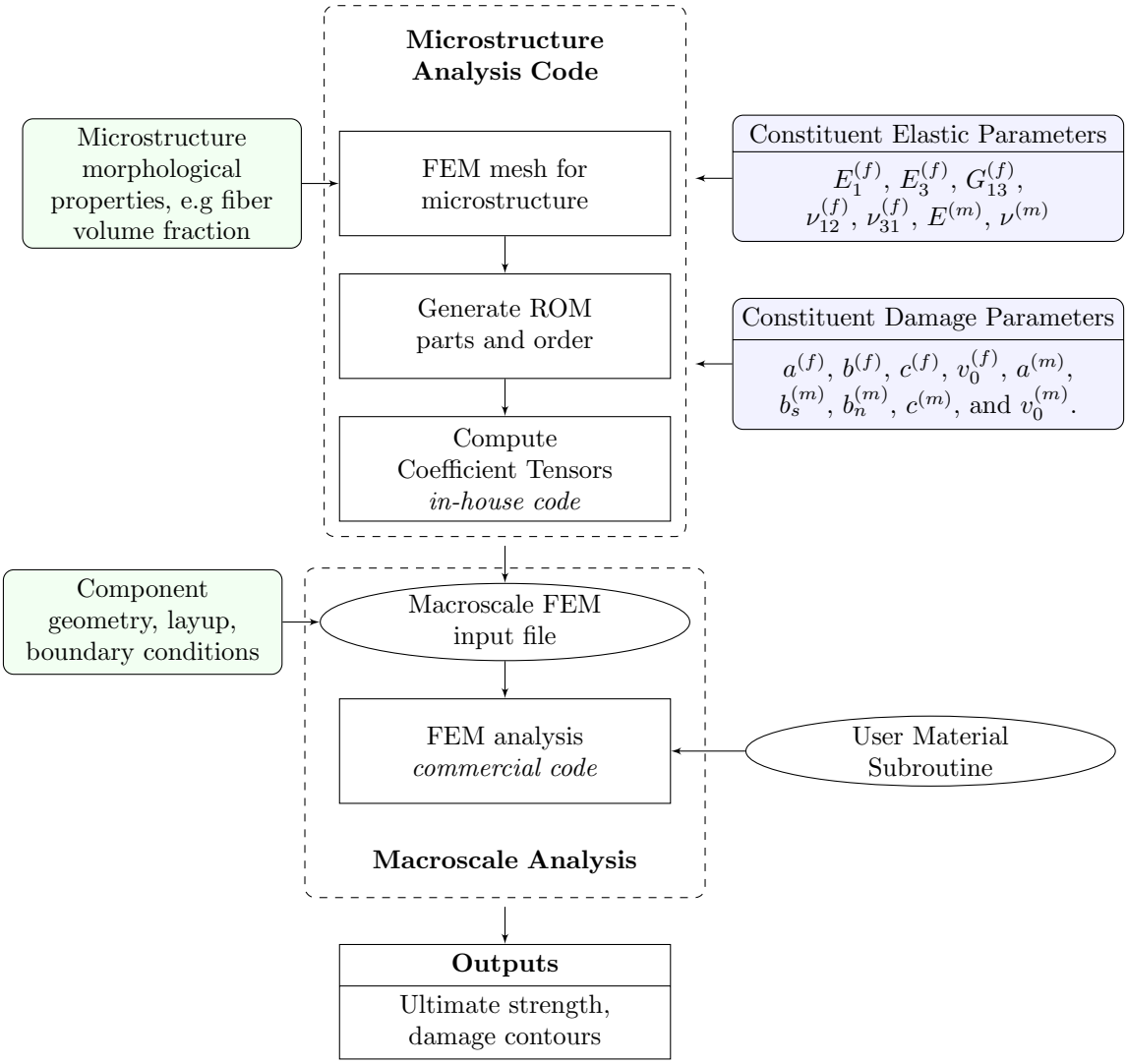

Figure 2.3: Computational Implementation of the EHM model in Static Failure Prediction.

2.4.2 Fatigue Prediction Algorithm

The multitemporal homogenization scheme is implemented through the use of a Python driver script, whose algorithm is presented in Figure 2.4. Before the progressive failure analysis, the microstructure of the composite is preprocessed to generate the ROM and EHM coefficients and assign the constituent material parameters. The macroscale analysis in both micro- and macro-

time is performed in Abaqus. The Abaqus input file is constructed using the coefficients and material parameters of the microstructure and the geometry, layup, and boundary conditions of the specimen. The python driver then uses that input file to perform the multitemporal analysis: evaluating a single microchronological load cycle to determine the rate of damage evolution over the cycle, computing the number of cycles to jump in the macrotemporal analysis, and then solving the macrochronological problem, sequentially until the specimen fails or the maximum number of cycles is reached. In both the micro- and macrochronological problems, the UMAT is called to perform the microscale analysis at each quadrature point. One feature of the EHM method is that the same UMAT is employed for both time scales and is also a consistent subroutine between static and fatigue analysis, providing a great deal of flexibility in the range of loading scenarios which can be predicted with the EHM approach. Python scripting was additionally used to obtain the stress and strain response of the specimens at each resolved step to generate stiffness vs. cycles curves and was used to produce the damage contour plots to demonstrate progressive damage accumulation patterns.

2.4.3 High Performance Parallel Computing

Even with the computational savings achieved by the use of the EHM approach over standard CH, the multiscale analysis of laminated composites still presents significant computational expense. One method to drastically reduce the time required to perform this analysis is the use of high performance parallel computing. This time savings is particularly important in multitemporal analyses where analyses run on the order of weeks for serial analyses. Parallel computing environments are ubiquitous from personal laptop and desktop computers which come with two to eight computing cores up to government sponsored supercomputers with thousands of compute nodes. The ability to leverage this computational capability is essential to predicting FRP composite behavior in a fast manner. Several challenges exist in the transitioning of computer programs from serial processing to a parallel configuration. These include the selection of where to incorporate parallelization, ensuring proper communication between threads so that variables do not interact

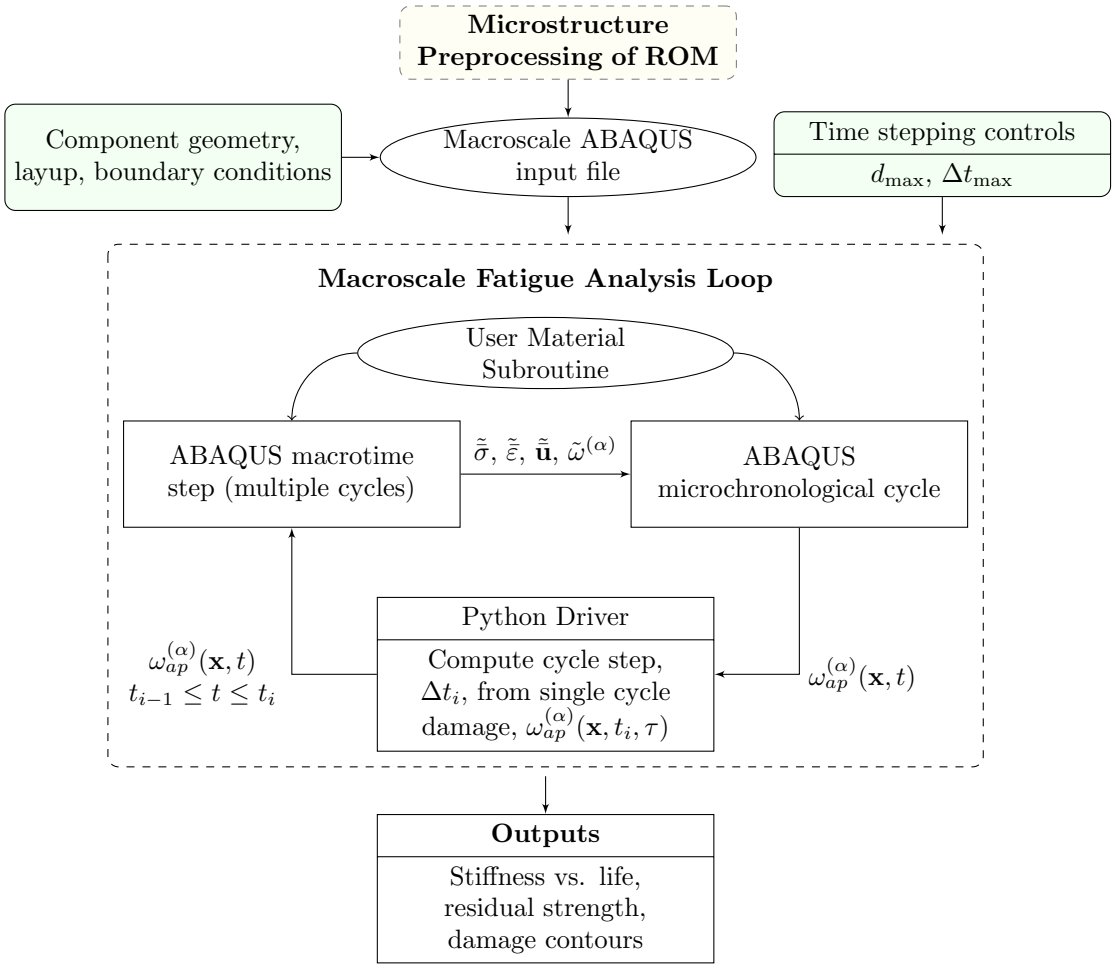

Figure 2.4: Computational Implementation of the EHM model in Fatigue Failure Prediction.

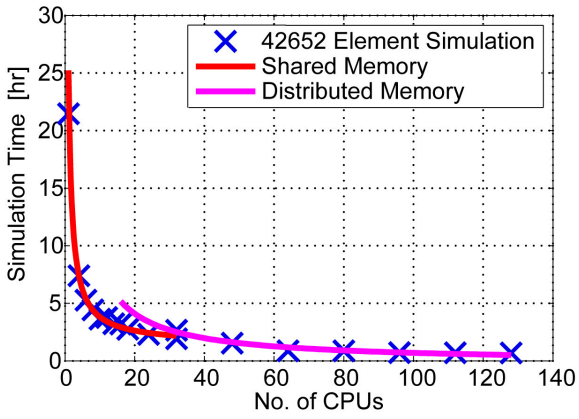

Figure 2.5: Elapsed Wall Time for EHM Analysis vs. Number of CPUs.

in an undesired manner, and coordinating threads in the writing from private variables to shared variables and external sources. In the EHM analysis, parallelization is implemented in two ways. First, the built-in parallel capability of Abaqus was exercised in solving the macroscale finite element problem. Second, the ROM analysis of each quadrature point was performed using a parallel do loop. In order to achieve parallel capability over the quadrature points, the UMAT subroutine was rewritten to significantly reduce the use of global variables, and organize the writing to large global arrays such that race and overwrite conditions were eliminated. Figure 2.5 displays the comparison of simulation wall times for analyses run on 1 to 128 processors performing 100 solution increments of an EHM model for the prediction of a single quasi-isotropic open hole laminate in tensile loading. The finite element mesh consists of 42,652 elements with 8-point quadrature. Parallelization was implemented in such a way as to allow performance both in shared memory and distributed memory parallel configurations. In serial, the analysis required 22 hours of wall time to complete. Employing 4 processors in parallel, a common setup for mid-range modern desktops, the computational time was reduced to about 6 hours. Utilizing resources on the scale of a cluster computing environment, the computational time is further reduced. This time savings is essential in debugging, calibration, and rapid result collection.

To further demonstrate the computational costs of the EHM approach, several laminated composite static failure prediction cases were considered. Simulation of the numerical specimens was

performed using a parallel computing cluster with 16 2.1GHz AMD Opteron(TM) 6272 Processors and 128 GB shared memory on each compute node. Each of the simulations were performed using 8 cpus on a single compute node in a shared memory parallel configuration. The finite element mesh and wall time for each of the twelve prediction cases is shown in Table 2.1. In the description of load cases, UNT stands for unnotched tension, OHT for open hole tension, UNC for unnotched compression, and OHC for open hole compression.

Table 2.1: Numerical Specimen Mesh Sizes and Wall Clock Times for Failure Analysis.

Layup	Case	No. of elements	No. of nodes	Wall time (H:MM)
$[0,45,90,-45]_{2S}$	UNT	29264	61216	1:54
$[30,60,90,-60,-30]_{2S}$	UNT	40498	84412	2:29
$[60,0,-60]_{3S}$	UNT	37131	77370	2:15
$[0,45,90,-45]_{2S}$	OHT	42652	86896	4:34
$[30,60,90,-60,-30]_{2S}$	OHT	53340	108768	4:51
$[60,0,-60]_{3S}$	OHT	47853	97836	4:09
$[0,45,90,-45]_{2S}$	UNC	2744	5876	0:40
$[30,60,90,-60,-30]_{2S}$	UNC	3680	7704	0:50
$[60,0,-60]_{3S}$	UNC	3276	6948	0:47
$[0,45,90,-45]_{2S}$	OHC	42652	86896	6:29
$[30,60,90,-60,-30]_{2S}$	OHC	53340	108768	7:31
$[60,0,-60]_{3S}$	OHC	47853	97836	6:17

Chapter 3

PREDICTIONS OF DAMAGE ACCUMULATION IN CARBON FIBER REINFORCED POLYMER COMPOSITES

To demonstrate the predictive capability of the EHM approach, the model was employed in a recent blind prediction exercise sponsored by the Air Force Research Laboratory (AFRL). In the "Assess and Quantify the Benefits of Applying Damage Tolerant Design Principles to Advanced Composite Aircraft Structure" (DTDP) program the proposed multiscale model was used to predict the static and fatigue behavior of laminated IM7/977-3 carbon FRP composites. The goal of the DTDP program was to assess the current modeling capabilities in commercial software and research codes to accurately predict the strength and progressive damage accumulation in composite materials with various layup and loading conditions. The program was separated into four phases - (1) blind prediction of static response, (2) recalibration of the static model, (3) blind prediction of fatigue response, and (4) recalibration of the fatigue model. Details of the first half of the program for static predictions are presented in Section 3.1 and the results from the second half for fatigue are described in Section 3.2.

3.1 Damage Tolerance Design Principles Program - Static Predictions

In the first phase of the DTDP program, a series of blind predictions of laminated composite strength, stiffness, and damage accumulation were made using EHM on multiple FRP composite layups and loading configurations. A set of lamina-scale experiments was provided by the AFRL to calibrate the EHM model for the blind predictions, the multiscale model was constructed and calibrated, and blind prediction results were submitted to the AFRL. In the second phase, the experimental results for the blind prediction cases were received and the EHM model was recalibrated and additional recalibrated predictions performed. The experiments used in the static prediction

portion of the program are included in Section 3.1.1. Sections 3.1.2.1 and 3.1.2.2 The procedures for the calibration, blind prediction, and recalibration phases are presented below. The results of EHM model in the static prediction portion of the DTDP program were presented in part at the AIAA SciTech 2015 conference [16]. This work is also expected to be published in a forthcoming special issue of the Journal of Composite Materials [18] which will contain additional publications containing the programmatic aspects of the exercise and the results from the remaining participants.

3.1.1 Experiments

Two sets of experiments were provided in the static portion of DTDP program. In the first phase, the data from a suite of experiments made from IM7/977-3 unidirectional tape was released in order to calibrate the multiscale model. These calibration experiments included 0° tension and compression, 90° tension and compression [5, 8], 90° three point bending [11], $\pm 45^\circ$ tension [6], V-notch shear [7], end notch flexure (no official standard provided), and double cantilever beam [9] tests. In the second phase, the experimental results corresponding to the blind prediction cases were released for the $[0,45,90,-45]_{2S}$, $[60,0,-60]_{3S}$, and $[30,60,90,-60,-30]_{2S}$ layups with open hole and unnotched configurations under static tension and compression loading. The layup and geometry of each of these experiments are provided in Table 3.1. All tests were performed using an MTS testing machine in displacement controlled loading. X-ray radiography and computed tomography (CT) imaging were employed to generate images of internal damage within the laminates using zinc-oxide dye penetrant.

3.1.2 Modeling Details

One of the primary ground rules in the DTDP program was that a single consistent modeling approach be used for all prediction cases. This included the mesh generation method, application of boundary conditions, and selection of model parameters. Details of the microscale ROM and the macroscale mesh generation strategy employed in the DTDP predictions are included herein.

Panel Name	Layup	Test Type	ASTM Standard	No. plies	Width (mm)	Thick (mm)	Length (mm)	Hole Dia. (mm)
CC-1	0	tension	D3039	8	12.7	1.0	250.0	-
CC-2	90	tension	D3039	16	25.4	2.0	250.0	-
CC-3	0	comp.	D3410	16	12.7	2.0	140.0	-
CC-4	90	comp.	D3410	24	25.4	3.0	140.0	-
CC-5	[0, 90]4S	v-notch	D7078	16	56	2.0	76.0	-
CC-6	90	3 pt-bend	D790	16	12.7	2.0	110.0	-
CC-12	0	DCB	D5528	24	25.4	3.0	250.0	-
CC-16	0	ENF	Draft	24	25.4	3.0	250.0	-
CC-17	[+45, -45]4S	tension	D3518	16	25.4	2.0	250.0	-
CC-19	$[0,45,90,-45]_{2S}$	tension	D3039	16	25.4	2.0	250.0	-
CC-20	$[30,60,90,-60,-30]_{2S}$	tension	D3039	20	25.4	2.5	250.0	-
CC-21	$[60,0,-60]_{3S}$	tension	D3039	18	25.4	2.3	250.0	-
CC-22	$[0,45,90,-45]_{2S}$	tension	D3039	16	38.1	2.0	250.0	6.35
CC-23	$[30,60,90,-60,-30]_{2S}$	tension	D3039	20	38.1	2.5	250.0	6.35
CC-24	$[60,0,-60]_{3S}$	tension	D3039	18	38.1	2.3	250.0	6.35
CC-25	$[0,45,90,-45]_{2S}$	comp.	D3410	16	25.4	2.0	140.0	-
CC-26	$[30,60,90,-60,-30]_{2S}$	comp.	D3410	20	25.4	2.5	140.0	-
CC-27	$[60,0,-60]_{3S}$	comp.	D3410	18	25.4	2.3	140.0	-
CC-51	$[60,0,-60]_{3S}$	comp.	D3410	18	38.1	2.3	250.0	6.35
CC-52	$[0,45,90,-45]_{2S}$	comp.	D3410	16	38.1	2.0	250.0	6.35
CC-53	$[30,60,90,-60,-30]_{2S}$	comp.	D3410	20	38.1	2.5	250.0	6.35

Table 3.1: Test Matrix for the Static Prediction Phases of the DTDP Program.

3.1.2.1 Reduced Order Model of the Representative Volume Element

The RVE of the microstructure for the IM7/977-3 composite is idealized as a square-packed unit cell with a fiber volume fraction of 65% as identified from acid digestion testing of the composite material. The partitioning of the RVE for the EHM model is illustrated in Figure 3.1. Part 1 is comprised of the entire domain of the fiber and parts 2-4 partition the matrix. Fiber failure is interpreted from damage accumulation in part 1. Parts 2 and 3, used to describe the matrix material, account for the presence of the disparate failure mechanisms of transverse matrix cracking and delamination, respectively. Part 4, which also describes the matrix, exhibits damage under both the transverse matrix and delamination failure modes. The coefficient tensors, influence functions, localization operators, and polarization tensors, which define the EHM model, are computed as a

preprocessing step before progressive damage analysis. For this microstructure, the use of EHM reduces the model complexity from a finite element model comprised of 416 nodes and 1206 tetrahedral elements to a system with 24 degrees of freedom. The internal state variables required to be stored to represent the damage evolution is also reduced from 1206 in the direct microstructure model to 4 variables in the EHM model.

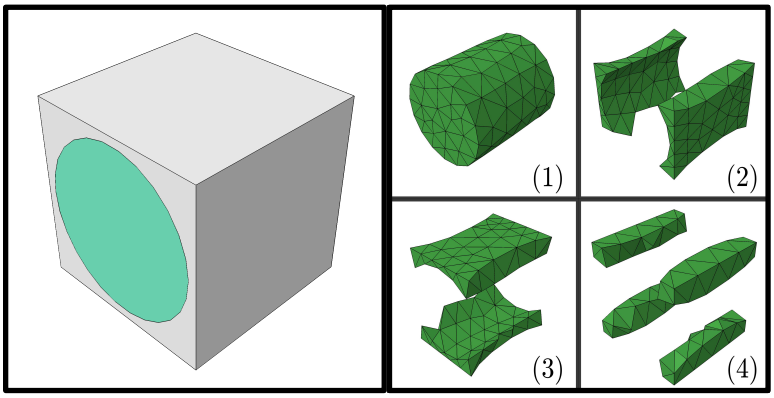

Figure 3.1: Partitioning of the Unidirectionally Reinforced Composite Unit Cell.

Over the course of the DTDP program, a modeling methodology to directly account for the discrepancy between longitudinal stiffness of 0° unidirectional tape under tensile and compressive loading was devised. Since the coefficient tensors associated with the EHM model are functions of the moduli of the fiber and matrix, modeling anisotropy requires building a separate model for tensile and compressive cases. The approach is therefore called the dual-ROM approach. The two models vary only in the longitudinal modulus of the transversely isotropic fiber, which is taken to be different for tension and compression, E^f_{3T} and E^f_{3C}, respectively. The value of E^f_{3C} was calibrated based on experimental data from the 0° compression tests and the value is included in Table 3.3. During the analysis of a laminated specimen, some fibers may be subjected to compressive stresses even when the specimen is under overall tensile loading. It is therefore appropriate to consider the compressive ROM in specimen subdomains where the fiber is subjected to compression and the tensile ROM elsewhere. In the current approach, the appropriate model is selected on the fly in the multiscale analysis based on the current state of strain in the fiber direction associated with each quadrature point. Using this approach, a consistent set of parameters is used for the

prediction of specimens in global tension and compression. The use of the dual-ROM and directly accounting for the discrepancy between longitudinal tension and compression moduli resulted in a significant improvement in accuracy in the prediction of lamina and laminate level composite stiffnesses across all of the experimental specimens.

3.1.2.2 Details of the Macroscale Model Discretization

A number of laminated composite specimens are considered in the investigations described herein including $[0,45,90,-45]_{2S}$, $[30,60,90,-60,-30]_{2S}$, and $[60,0,-60]_{3S}$ layups in open hole and unnotched configurations. A consistent mesh generation approach is implemented for the construction of the finite element meshes for each laminate to reduce the effects of mesh size sensitivity and alignment bias. The finite element meshes of the numerical specimens consisted of elements with a nominal edge length of $h = 1$mm in the in-plane directions and one element per ply in the thickness direction (0.125mm). Numerical specimens were constructed according to the geometry of the gage section in the experiment setups. For symmetric layups, only half of the plies were modeled, taking advantage of the layup symmetry. The mesh in each layup was generated to be in alignment with the fiber longitudinal axis in each ply, as shown in Fig. 3.2. Since each ply is meshed individually, the nodal positions on the surface of each ply within a stack does not necessarily align. In order to ensure load transfer, the plies were connected using surface tie constraints.

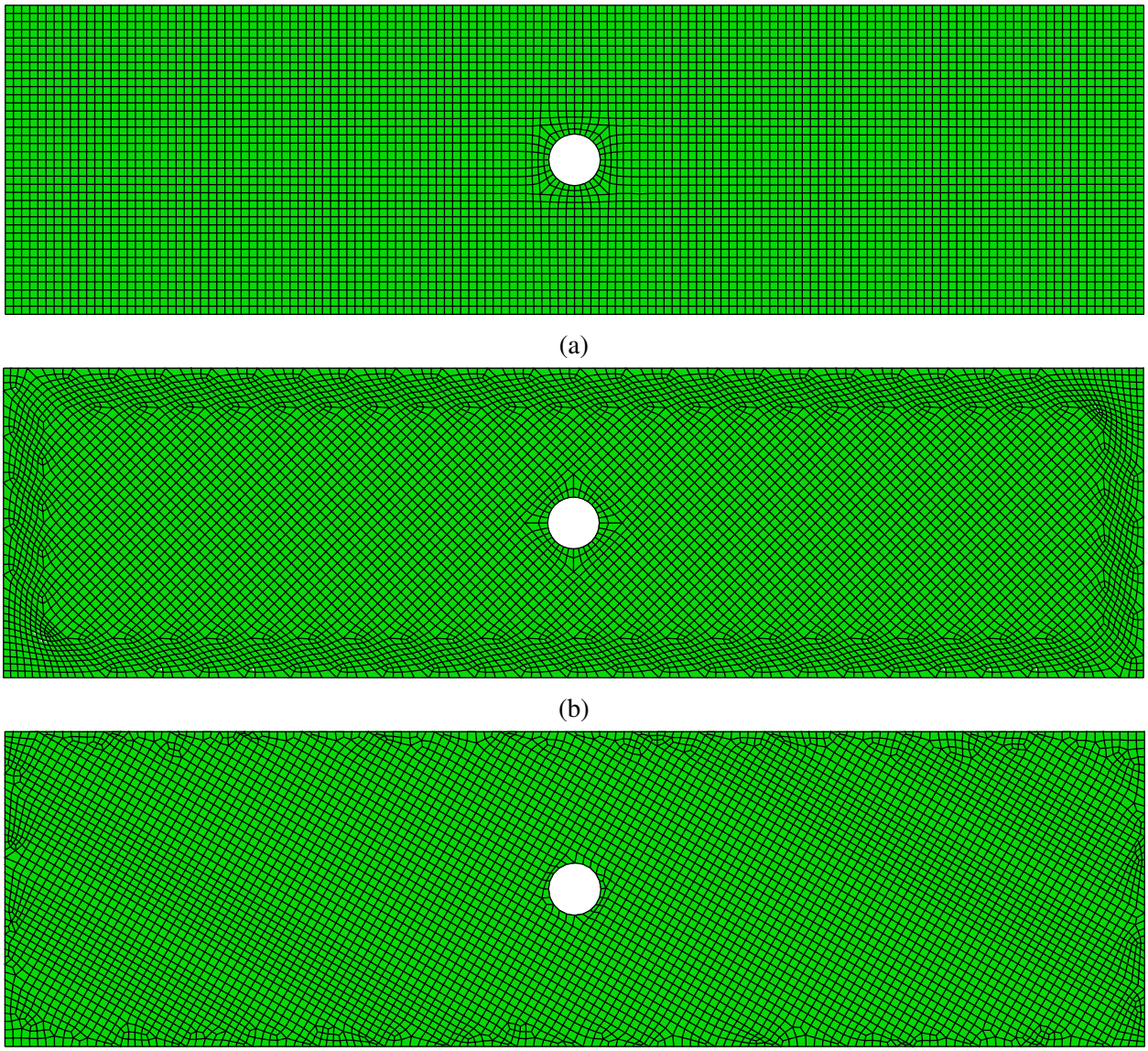

(a)

(b)

(c)

Figure 3.2: Aligned Mesh for (a) $0^\circ/90^\circ$ Plies, (b) $\pm 45^\circ$ Plies, and (c) $\pm 30^\circ/60^\circ$ Plies Used to Construct the Open-Hole Specimen Configurations.

3.1.2.3 Macroscale Mesh Density Study

The failure strength of materials predicted from CDM based approaches exhibits sensitivity to the size of the elements used in the finite element mesh in that larger elements tend to correlate with larger predicted ultimate strengths. A mesh sensitivity study was performed for the [0,45,90,-45]$_{2S}$ quasi-isotropic layup with an open-hole configuration subjected to compression loading. The behavior of this layup is consistent with results seen from the other specimens, as well. For comparison with the baseline mesh of $h = 1$mm, a coarser and finer mesh were investigated with edge lengths of 1.5mm and 0.5mm, respectively. A clear trend of a small decrease in the overall strength with decreasing element size was observed in the simulations. The predicted ultimate strength was 344 MPa for the coarse mesh, 335 MPa for the baseline, and 328 MPa for the fine mesh; a difference of 2-3% from the baseline result. This effect is the result of well-known damage localization. Damage contours provided in Figure 3.3 for 90% of the static ultimate strength demonstrate the damage localization effect where the width of the damage region in the loading direction (vertical on the page) is larger for the coarser mesh and smaller for the fine mesh. In these figures the reduced width of the damage band in the direction of the applied load can be seen, but the overall damage pattern remains similar for all meshes.

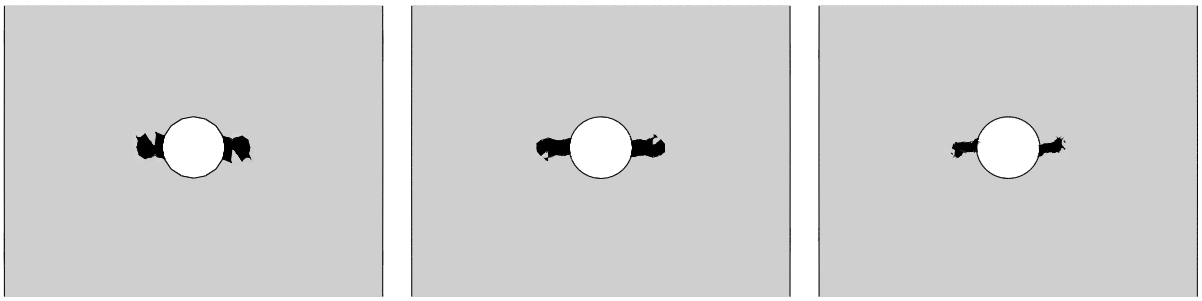

(a) Coarse (b) Baseline (c) Fine

Figure 3.3: Comparison of Transverse Matrix Damage Contours for 90% Ultimate Stress in [0,45,90,-45]$_{2S}$ Open-Hole Compression Simulations for the Mesh Sensitivity Study.

3.1.2.4 Macroscale Mesh Alignment Study

The failure behavior of composite material models also exhibits significant mesh alignment dependency [92]. To investigate the effect of mesh alignment dependency with the EHM models, four demonstration finite element meshes were considered. In all four models, a single lamina of unidirectional IM7/977-3 composite subject to uniaxial tension along the fiber orientation was modeled using EHM. The lamina are shown with the fiber oriented with the page vertical. The first pair of models considers the case of a lamina with a center crack perpendicular to the fiber orientation. In the second pair, the center crack is replaced with an open hole with diameter equal to one-sixth the overall width, as in the open hole tests performed experimentally. Both pairs contain one model with a structured mesh, i.e. mesh edges are aligned along the fiber direction, and one unstructured mesh. Using symmetry, only one quarter of each example was modeled.

Fig. 3.4 and Fig. 3.5 show the evolution of transverse matrix damage in the cracked lamina with respect to the applied strain. The boundary conditions on the undamaged lamina for both models are shown in 3.4(a) and 3.5(a). In both the structured mesh and unstructured mesh, matrix damage propagates in a thin band parallel to the fiber orientation. This band is narrower and longer in the structured mesh 3.4(b) than in the unstructured mesh 3.5(b). Physically, this corresponds to a phenomenon referred to as "fiber splitting," where the two adjacent fiber regions are split by the presence of a transverse matrix crack, which occurs at the crack tip and extends parallel in the fiber direction and perpendicular to the crack orientation. This is in contrast with the crack propagation behavior of an isotropic material, where the crack tip would tend to grow in the direction of the crack orientation. The crack does not grow along its orientation in this case because the stronger fibers bridge the crack front and restrain its growth in that direction.

At 0.75% applied strain, the damage band continues to propagate vertically in the structured mesh, Fig. 3.4(c), but begins to widen in the unstructured mesh, Fig. 3.5(c). The stress concentration at the crack tip is negated with the structured mesh as the right half of the specimen effectively does not see the crack. In the unstructured mesh, the random element distribution causes stress concentrations and artificial damage propagation paths into the right side of the structure. The

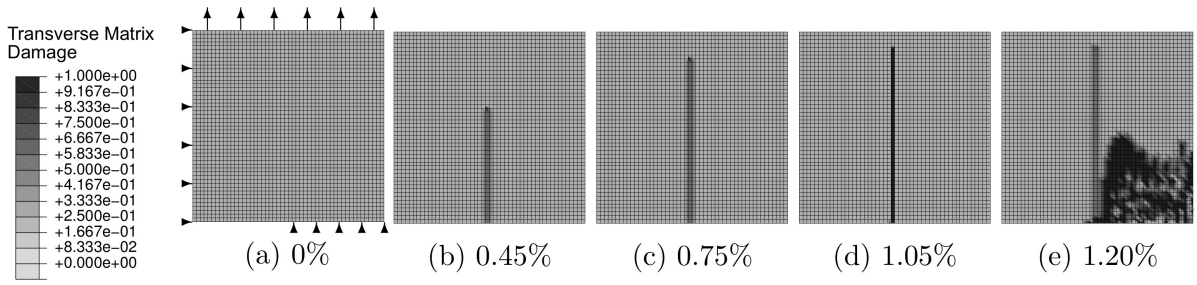

Figure 3.4: Damage Evolution in Structured Mesh of an IM7/977-3 Lamina with Center Crack vs. Applied Strain of (a) 0% to (e) 1.20%.

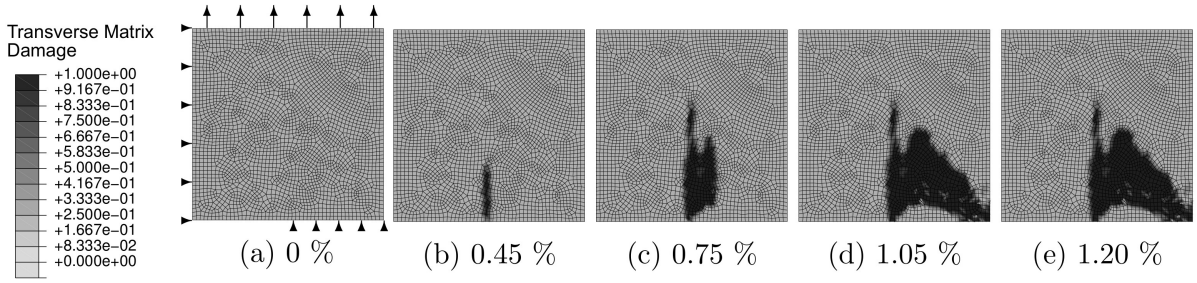

Figure 3.5: Damage Evolution in Unstructured Mesh of an IM7/977-3 Lamina with Center Crack vs. Applied Strain of (a) 0% to (e) 1.20%.

spread of damage perpendicular to the fiber direction seen in Fig. 3.5(c) leads to full damage and specimen failure in Fig. 3.5(d) at an applied strain of 1.05%. In contrast, the structured mesh still exhibits the thin damage damage at an applied strain of 1.05% (Fig. 3.4(d)) and does not exhibit failure until an applied strain of 1.20% (Fig. 3.4(e)). The stress vs. strain curves in Fig. 3.6 tell the same story, showing that the structured mesh fails at a level nearly two times the strength of the unstructured mesh. In the next example, the mesh alignment effect is also demonstrated to be present in unidirectional lamina with an open hole, similar to the quasi-isotropic open hole experiments. Due to rounded geometry of the hole, the structured mesh is not able to be achieved over the entire width of the specimen, but begins just to the right of the hole. The transverse matrix damage evolution as a function of applied strain is shown for the structured mesh in Fig. 3.7 and the unstructured mesh in Fig. 3.8. In Fig. 3.7(b-c) and Fig. 3.8(b-c), up to an applied strain of 0.60%, the damage pattern looks similar for the structured and unstructured meshes. At a strain of 0.75% however, the

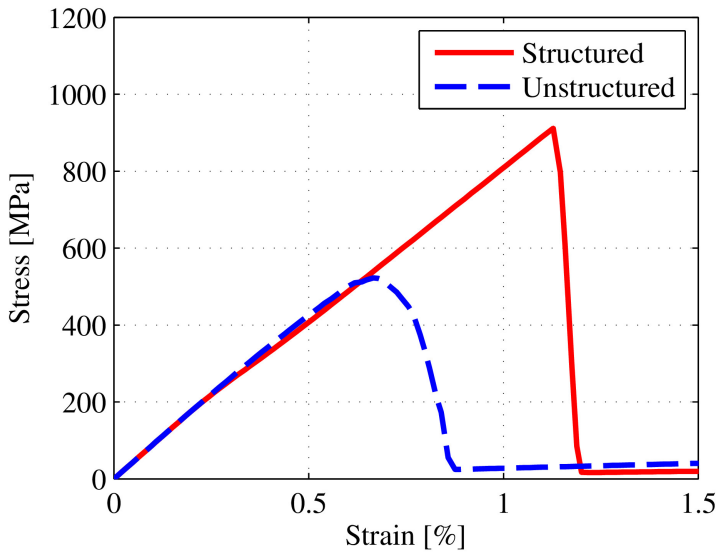

Figure 3.6: Stress vs. Strain Curves for Structured and Unstructured Meshes of IM7/977-3 Lamina with Center Crack.

difference between the two becomes apparent. The unstructured mesh shows damage propagating perpendicular to the fiber direction, Fig. 3.8(d), while the damage in the structured mesh continues to propagate along the fiber direction, Fig. 3.7(d). Damage does not propagate significantly perpendicular to the fiber direction until a strain of 0.90%, Fig. 3.7(e). Comparing the stress at failure from the structured and unstructured meshes in Fig. 3.9, the failure strength of the structured mesh is about 25% greater than the unstructured mesh. It is apparent from this study that a structured mesh, aligned with the fibers in the lamina, needs to be used in simulating the anisotropic behavior of fiber reinforced materials, in order to correctly capture the physically observed fiber splitting phenomena and associated effect on failure strength.

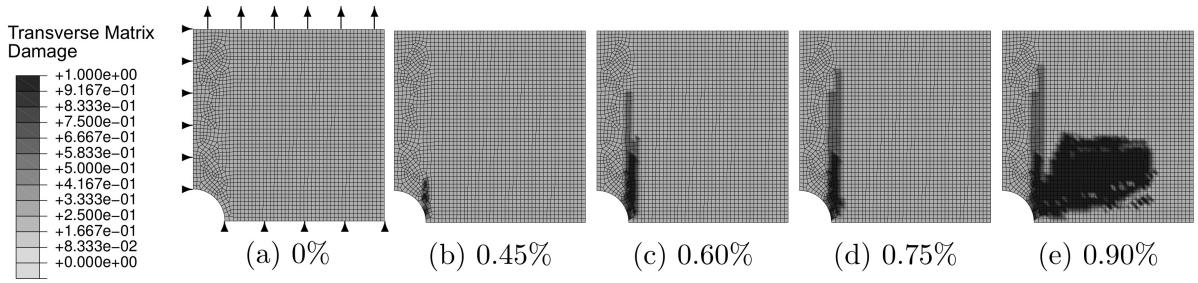

Figure 3.7: Damage Evolution in Structured Mesh of an IM7/977-3 Lamina with Open Hole vs. Applied Strain of (a) 0% to (e) 0.90%.

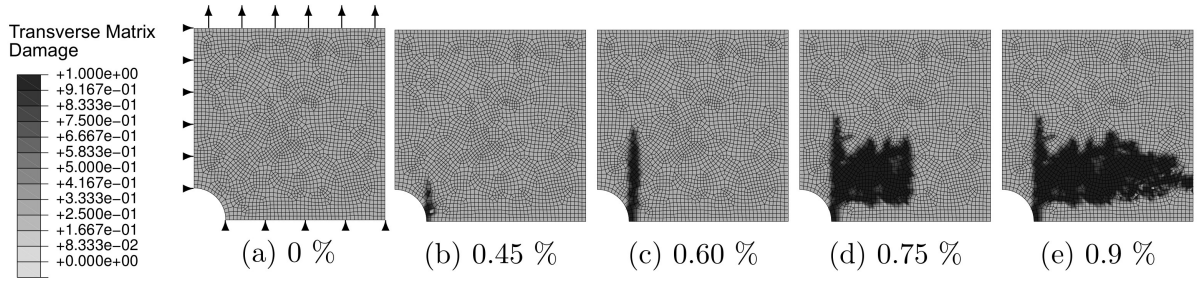

Figure 3.8: Damage Evolution in Unstructured Mesh of an IM7/977-3 Lamina with Open Hole vs. Applied Strain of (a) 0% to (e) 0.90%.

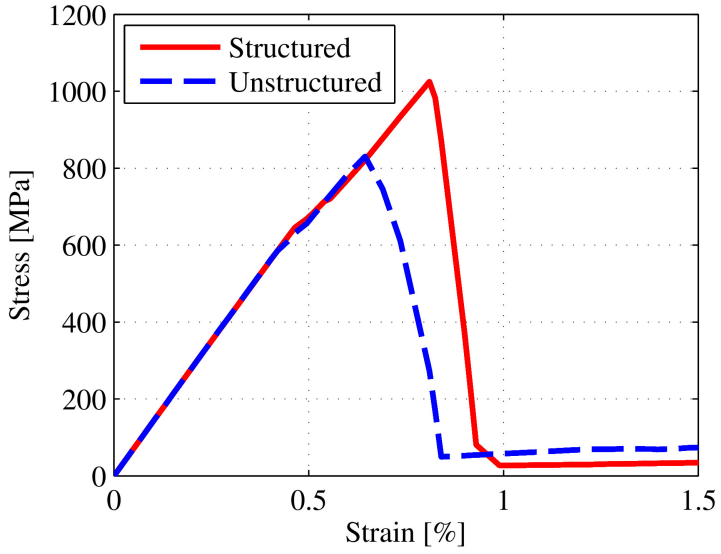

Figure 3.9: Stress vs. Strain Curves for Structured and Unstructured Meshes of IM7/977-3 Lamina with Open Hole.

3.1.3 Calibration

Because of the multiscale characteristics of the EHM approach, the associated model parameters are described at the scale of the composite constituents. In contrast, the calibration experiments are provided at the lamina or laminate levels. Calibration of the elastic and damage evolution parameters was therefore performed using a numerical optimization procedure, where the discrete L_2 norm of the differences between the effective composite properties observed in the experiments and those predicted by numerical simulations is minimized. Among the calibration experiments, six types of experiments were used to calibrate the material parameters: 0° tension, 0° compression, 90° three point bending, 90° compression, $\pm 45^\circ$ tension, and V-notch shear tests. The effective composite properties defined by these tests are summarized in Table 3.2.

Table 3.2: Comparison of Effective Composite Properties from Experiments and Blind/Recalibrated Static Simulations.

Parameter	Description	Experiment Average	Simulated Value	Calibration Experiment
E_{1t} (GPa)	Long. tension modulus	164.3	163.9	0° tension
E_{1c} (GPa)	*Long. compression modulus*	*137.4*	*137.4*	0° *compression*
E_2 (GPa)	Transverse modulus	8.85	8.85	90° three point bending
G_{13} (GPa)	Shear modulus	4.94	4.94	$\pm 45^\circ$ tension
ν_{12}	Long. Poisson's ratio	0.3197	0.321	0° tension
ν_{21}	Transverse Poisson's ratio	0.0175	0.0173	0° tension
X_T (MPa)	Long. tension Strength	2905	2905	0° tension
X_C (MPa)	Long. compression Strength	1274/*1680*	1274/*1680*	90° compression/*Literature*
Y_T (MPa)	Trans. tension Strength	130.0	130.0	90° three point bending
Y_C (MPa)	Trans. compression Strength	247.6	247.7	90° compression

The EHM model implemented in this study includes seven parameters to fully describe the elastic moduli tensor of the transversely isotropic fiber (i.e., E_1^f, E_3^f, G_{13}^f, ν_{12}^f, and ν_{31}^f) and the isotropic matrix (i.e., E^m and ν^m) where the 3-direction is along the direction of the fiber length, E indicates the Young's modulus, G the shear modulus, and ν the Poisson's ratio. The elastic properties of the fiber and matrix were calibrated to match the mean experimental values reported by the AFRL from the elastic portions of the 0°, $\pm 45^\circ$, and 90° three point bend tests. The calibrated constituent parameters are reported in Table 3.3. The experimental data indicates that the lamina

level stiffness of the 0° unidirectionally reinforced specimens was 16.4% lower under compression compared to tension. While the tension-compression anisotropy may be addressed by considering a separate compressive and tensile moduli for the fiber (denoted as E_{3C} and E_{3T}, respectively), as discussed in Section 3.1.2.1, all DTDP program participants agreed to proceed without accounting for this anisotropy in the blind prediction phase. In the initial calibration and blind prediction stage, a single longitudinal fiber modulus consistent with the tension tests was chosen. This assumption was revisited in the recalibration of the model as described in Section 3.1.5.

Table 3.3: Calibrated Material Properties for DTDP Static Predictions.

Property	Experiment	Blind Prediction	Recalibration
Elastic Parameters			
$E_1^{(f)}$ [GPa]	0° Tens.	12.45	12.45
$E_{3T}^{(f)}$ [GPa]	0° Tens.	257.4	257.4
$E_{3C}^{(f)}$ [GPa]	0° Comp.	257.4	215.5
$G_{13}^{(f)}$ [GPa]	$\pm 45^\circ$ Tens.	146.0	146.0
$\nu_{12}^{(f)}$	0° Tens.	0.291	0.291
$\nu_{31}^{(f)}$	0° Tens.	0.206	0.206
$E^{(m)}$ [GPa]	90° Tens.	3.70	3.70
$\nu^{(m)}$	90° Tens.	0.37	0.37
Damage Evolution Parameters			
$a^{(f)}$	0° Tens.	0.04921	0.050562
$b^{(f)}$	0° Tens.	274	274
$c^{(f)}$	0° Comp.	2.3514	1.4481
$\upsilon_0^{(f)}$	0° Tens.	1367	1367
$a^{(m)}$	90° 3PB	0.001582	0.001592
$b_n^{(m)}$	90° 3PB	15	15
$b_s^{(m)}$	$\pm 45^\circ$ Tens.	-3.2	-3.2
$c^{(m)}$	90° Comp.	0.567	0.535
$\upsilon_0^{(m)}$	90° 3PB	636.2	636.2

The accumulation of damage within the fiber was characterized by four model parameters ($a^{(f)}$, $b^{(f)}$, $c^{(f)}$, and $\upsilon_0^{(f)}$), whereas five parameters ($a^{(m)}$, $b_n^{(m)}$, $b_s^{(m)}$, $c^{(m)}$, and $\upsilon_0^{(m)}$) were employed to characterize the matrix damage evolution. Table 3.3 summarizes the calibrated damage evolution parameters. The experimental data used to calibrate each parameter are also indicated in Table 3.3.

Fiber strength and damage evolution (characterized by $a^{(f)}$, $b^{(f)}$, and $\upsilon_0^{(f)}$) primarily control failure in the 0° tension specimens. The fiber compression anisotropy parameter, $c^{(f)}$, governs failure in the 0° compression specimens. The failure of the 90° three point bend tests is predominantly affected by $a^{(m)}$, $b_n^{(m)}$, and $\upsilon_0^{(m)}$ and similarly the failure in the 90° compression specimens is governed by the matrix compression anisotropy parameter, $c^{(m)}$. The ductility of the $\pm 45^\circ$ tension specimens is dictated by the $b_s^{(m)}$ parameter.

Figures 3.10 and 3.11 show the comparison of the stress-strain response observed experimentally and computed using the calibrated EHM model. Figure 3.10 characterizes the unidirectional normal behavior, which is quite brittle. The fiber compression anisotropy parameter, $c^{(f)}$, was calibrated to match the experimental mean of 1274 MPa as reported from the experiments performed at the AFRL (Figure 3.10(b)). This value was revised in the recalibration phase to reflect higher reported values for this property in literature sources in agreement with all program participants. Figure 3.11 shows the $\pm 45^\circ$ and V-notch shear behavior which demonstrate significant ductility. For shear cases, the matching is performed up to 10% and 5% strain for the $\pm 45^\circ$ tension and V-notch shear cases, respectively, since the experimental data is reliable only up to these strain magnitudes due to strain gage failure [6, 7]. The agreement between the experiments and simulations is excellent. Table 3.2 shows the comparison between the specimen level strength and stiffness properties from experiments and numerical simulations, which also demonstrate the accuracy of the calibration.

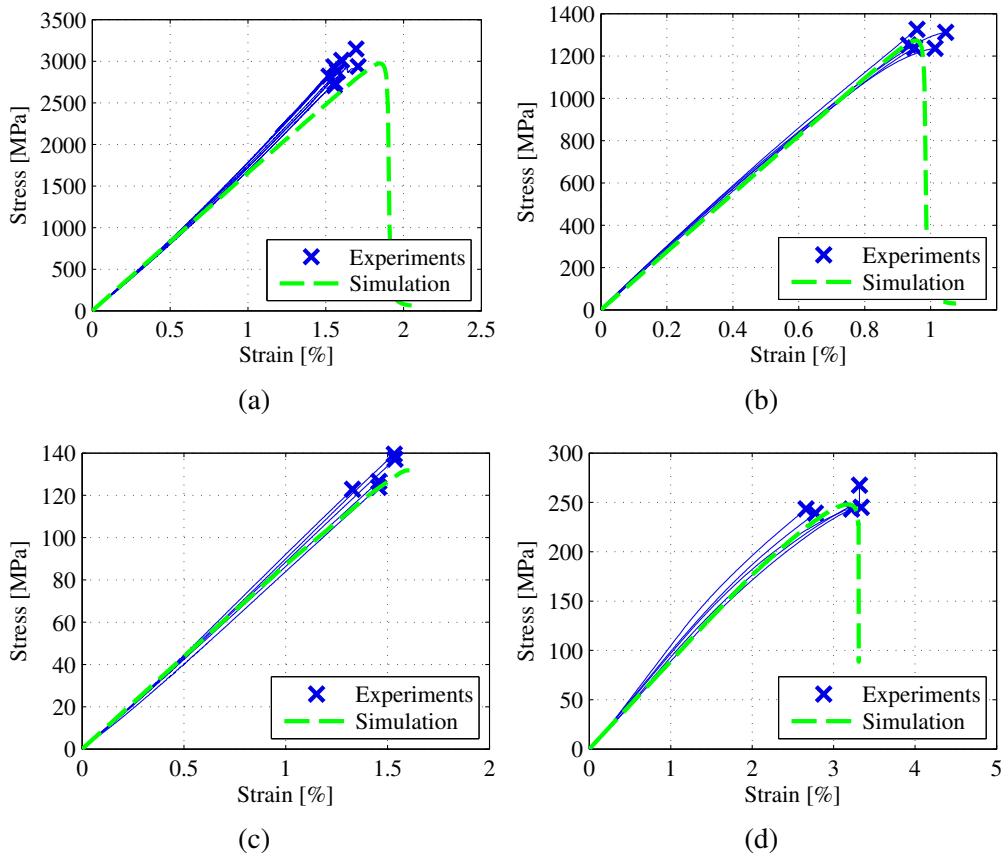

Figure 3.10: Composite Normal Stress-Strain Response from (a) 0° Tension, (b) 0° Compression, (c) 90° Three Point Bending, and (d) 90° Compression.

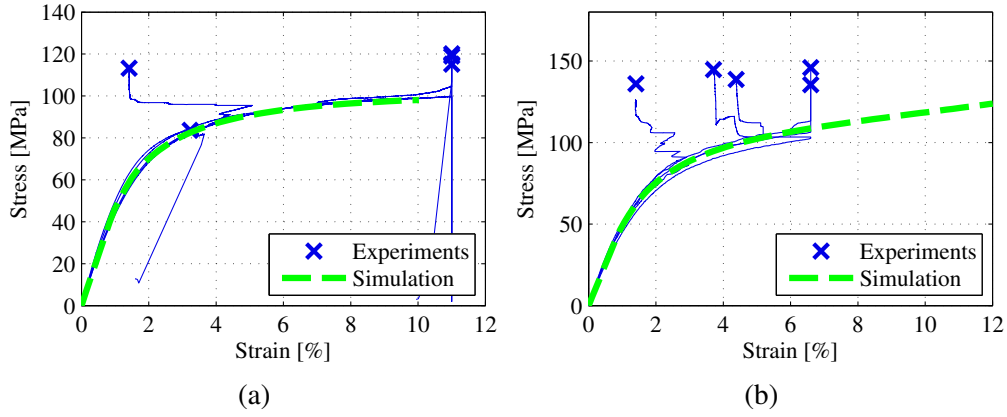

Figure 3.11: Composite Shear Stress-Strain Response from (a) $\pm 45^\circ$ Tension and (b) V-notch Shear.

3.1.4 Blind Prediction

The calibrated EHM model was exercised to predict damage accumulation, stress-strain response, and failure strengths of the $[0,45,90,-45]_{2S}$, $[30,60,90,-60,-30]_{2S}$, and $[60,0,-60]_{3S}$ specimens with open-hole and unnotched configurations under tension and compression. After calibrating the EHM model, the blind prediction phase included constructing the macroscale specimen geometry and discretization for each layup and executing the specimen analysis to obtain the quantities of interest mentioned above. The models used in the blind predictions consisted of 36,000-48,000 tri-linear hexahedral elements with full Gauss quadrature (i.e., eight integration points). Only half of the plies in each laminate were modeled, utilizing the symmetry of the layups. In each case, loading was idealized by applying a pinned boundary condition (i.e. displacement in the specimen longitudinal direction set to zero) at one end of the specimen and applying a monotonically increasing displacement along the longitudinal direction of the opposite end until failure. Strain was computed using a "virtual extensometer" mimicking the extensometer employed in the experiments for the open-hole specimens or the strain gauges in the unnotched specimens. Two nodes in the mesh of the exterior ply in each numerical specimen were identified corresponding to the extensometer ends in the experiments. The simulated strain is reported as the change in the distance between those two nodes divided by the initial separation distance. Stress was computed from the numerical specimens as the sum of the reaction forces at the pinned end of the specimen divided by gross cross-sectional area of the specimen modeled.

3.1.5 Recalibration

Upon submission of the blind prediction results to the AFRL, the experimental data for the twelve experiments were received for recalibration of the EHM model. The purpose of the recalibration was to reevaluate the assumptions made in the blind prediction phase, make corrections to the model or parameters as necessary, and revise the modeling approach accordingly. The manner in which the initially provided experiments were used to calibrate the multiscale model was

assessed and ways in which the model could be improved to better utilize the information from the new experimental datasets were identified. Two changes were made to the multiscale model in the recalibration phase in this regard. (1) The tension/compression stiffness anisotropy of the 0° composite tape under longitudinal loading was directly accounted for in the EHM model, and (2) the effective longitudinal compressive strength of the composite was increased in agreement with all of the program participants. In order to remain consistent across all prediction cases, any change in the model or parameters were applied to the entire suite of blind prediction simulations.

The initial calibration experiments demonstrated a marked discrepancy between the effective longitudinal modulus of the 0° unidirectional tape under tension and compression loading. In the recalibration phase, the dual-ROM approach described in Section 3.1.2.1 was implemented. Using this approach, a consistent set of parameters was used for each of the twelve specimens. An additional recalibration step was implemented to address a perceived experimental issue in the 0° compression experiment observed and agreed upon by the team of researchers participating in this study. The 0° compression specimens exhibited a significantly lower failure stress compared to data available in the literature for identical or very similar material systems. The team decided to consider the effective longitudinal compression strength to be 1680 MPa compared to the experimentally observed value of 1274 MPa. The recalibrated material parameters are shown in Table 3.3 and the resulting effective composite properties are included in Table 3.2. The increased longitudinal compression strength improved the overall prediction accuracy, particularly in the compression experiments. A detailed discussion of the results from the blind prediction and recalibration phases is included below.

3.1.6 Results and Discussion

Overall, the EHM model in the blind prediction phase of the program yielded an average error of 13.1% for ultimate strength predictions and 13.6% for predictions of elastic stiffness. The average error was reduced after recalibration to 8.7% for ultimate strength and 4.4% for elastic stiffness predictions. Summaries of the predicted strength and stiffness values from the blind

prediction and recalibration phases are provided in Tables 3.4 and 3.5. Table 3.4 includes two sets of results from the recalibration phase. The first column corresponds to the case where only the compression stiffness discrepancy was corrected without a change in the compression strength of the 0° undirectional specimens. The second column reflects the effects of both compression stiffness and strength corrections. Accounting for the tension/compression anisotropy in stiffness alone accounted for a 2.7% improvement in the recalibrated prediction of strength and a 9.2% improvement in the prediction of stiffness. The increased compression strength accounted for an additional 1.7% improvement in the prediction of ultimate strength. All improvements reported above are the average of all twelve cases.

Table 3.4: Summary of Predicted Ultimate Strength for DTDP Static Simulations.

		Ultimate strength over gross cross section [MPa]						
					Recalibration			
Layup	Case	Exp.	Blind Prediction		$X_c = 1274$MPa		$X_c = 1680$MPa	
$[0,45,90,-45]_{2S}$	UNT	866	807	-6.9%	896	+3.5%	911	+5.2%
$[30,60,90,-60,-30]_{2S}$	UNT	473	582	+23.0%	492	+4.0%	522	+10.3%
$[60,0,-60]_{3S}$	UNT	1005	802	-20.2%	1012	+0.7%	1014	+0.9%
$[0,45,90,-45]_{2S}$	OHT	554	529	-4.5%	542	-2.2%	558	+0.7%
$[30,60,90,-60,-30]_{2S}$	OHT	409	423	+3.5%	453	+10.8%	449	+9.8%
$[60,0,-60]_{3S}$	OHT	543	498	-8.2%	487	-10.3%	502	-7.6%
$[0,45,90,-45]_{2S}$	UNC	605	451	-25.5%	474	-21.7%	605	0.0%
$[30,60,90,-60,-30]_{2S}$	UNC	392	368	-6.1%	349	-11.0%	425	+8.4%
$[60,0,-60]_{3S}$	UNC	765	437	-42.9%	469	-38.7%	602	-21.4%
$[0,45,90,-45]_{2S}$	OHC	341	335	-1.8%	326	-4.4%	393	+15.2%
$[30,60,90,-60,-30]_{2S}$	OHC	295	299	+1.4%	296	+0.3%	360	+22.0%
$[60,0,-60]_{3S}$	OHC	358	311	-13.1%	297	-17.2%	368	+2.8%
		Avg. abs. error		13.1%		10.4%		8.7%

3.1.6.1 $[0,45,90,-45]_{2S}$ Layup

The average prediction error for the quasi-isotropic $[0,45,90,-45]_{2S}$ layup across all configurations was 9.6% and 13.3% for strength and stiffness, respectively, in the blind predictions. This improved to 5.3% and 4.3%, respectively, after recalibration. The stress-strain curves for the $[0,45,90,-45]_{2S}$ open hole and unnotched tension tests are shown in Figure 3.12. This figure, and

Table 3.5: Summary of Predicted Stiffness for DTDP Static Simulations.

		Stiffness [GPa]				
Layup	Case	Experiment	Blind Prediction		Recalibration	
$[0,45,90,-45]_{2S}$	UNT	60.5	61.52	+1.7%	60.41	-0.1%
$[30,60,90,-60,-30]_{2S}$	UNT	38.0	40.59	+6.8%	39.84	+4.8%
$[60,0,-60]_{3S}$	UNT	59.5	62.13	+4.4%	61.68	+3.7%
$[0,45,90,-45]_{2S}$	OHT	48.3	51.72	+7.1%	50.84	+5.3%
$[30,60,90,-60,-30]_{2S}$	OHT	32.4	35.40	+9.3%	34.57	+6.7%
$[60,0,-60]_{3S}$	OHT	48.8	51.88	+6.3%	50.84	+4.2%
$[0,45,90,-45]_{2S}$	UNC	48.0	61.52	+28.2%	52.80	+10.0%
$[30,60,90,-60,-30]_{2S}$	UNC	33.5	40.59	+21.2%	34.41	+2.7%
$[60,0,-60]_{3S}$	UNC	48.9	62.13	+27.0%	52.36	+7.1%
$[0,45,90,-45]_{2S}$	OHC	44.5	51.72	+16.2%	45.22	+1.6%
$[30,60,90,-60,-30]_{2S}$	OHC	30.1	35.40	+17.6%	31.76	+5.5%
$[60,0,-60]_{3S}$	OHC	44.4	51.88	+16.8%	44.77	+0.8%
		Avg. abs. error		13.6%		4.4%

the similar subsequent figures for stress and strain, includes the experimental average stress-strain curve to failure, the 90% and 95% confidence bounds on ultimate failure strength as provided by the program coordinators, and the simulated stress-strain curves for the blind prediction, the recalibrated model with $X_c = 1274$ MPa (Recal. A), and the recalibrated model with $X_c = 1680$ MPa (Recal. B). In both blind prediction and recalibration cases for the $[0,45,90,-45]_{2S}$ layups in tension, the EHM model is in very good agreement with the experimentally observed results. In the unnotched tension case (Figure 3.12a), the blind prediction under-predicted the ultimate strength of the specimen, while the recalibrated model slightly over-predicted the ultimate strength. In both cases, the prediction error was within 7%. For the open-hole specimen (Figure 3.12b), the blind and recalibrated predictions were within 5% error of the experimental value for ultimate strength. The correction made on the longitudinal compression modulus during the recalibration has a significant impact on the laminate stiffness and strength predictions under tension. This is due to the complex stress states present in the material constituents and points to advantages of using the present multiscale approach where the local stress states are available through localization operations (i.e., $\bar{\boldsymbol{\sigma}} \rightarrow \boldsymbol{\sigma}^{(i)}$). The open-hole simulations demonstrated higher ductility near ultimate

strength as compared to the experiments. In continuum damage approaches such as employed herein, damage in a quadrature point represents a loss of stiffness over the entire element. Because this loss of stiffness is not localized to a discrete crack, the width of the region experiencing the stiffness loss is larger than in the physical specimen, which accounts for the artificially higher degree of ductility witnessed in the simulations as compared to the experiments.

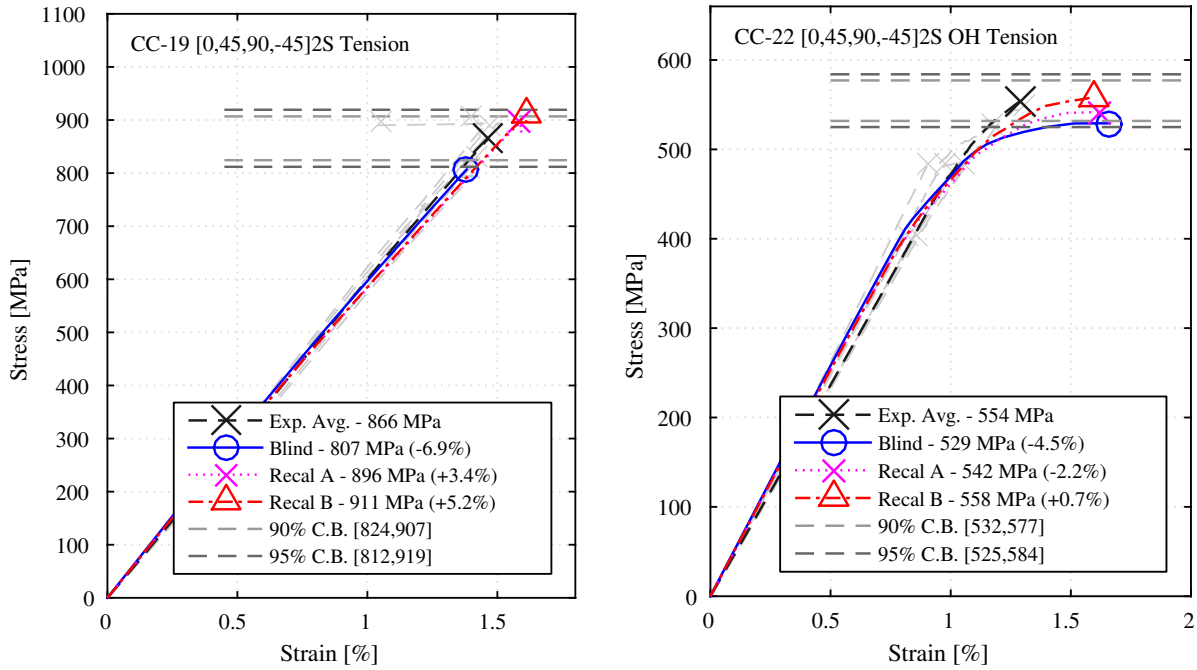

Figure 3.12: $[0,45,90,-45]_{2S}$ (a) Unnotched and (b) Open-Hole Tension Experiments and Blind/Recalibrated Stress vs. Strain Curves.

In the compression cases for the $[0,45,90,-45]_{2S}$ layup, the effect of the recalibration is pronounced. In Figure 3.13a, the prediction of stiffness is significantly improved through the use of the dual-ROM and directly accounting for the disparity between the longitudinal compression and tension moduli. In the blind predictions, the stiffness of the unnotched compression test had 28.2% error. After recalibration, this error in the stiffness was reduced to 10.0%. In the open hole specimens (Figure 3.13b), the error in the stiffness was reduced from 16.2% to 1.6%. The effect of using the higher value for longitudinal compression strength (Recal. B) is observed in both the unnotched and open hole compression cases. In the unnotched compression case, using

$X_c = 1680$MPa reduced the error in the prediction from over 20% to an error of less than 1% compared to the experiments. In the open hole compression case however, the strength prediction error increased from 1.8% to 15.1%. In both compression cases, using the higher value of lamina compression strength increased the ultimate strength of the laminate, as expected. The increased error in the open hole compression case is a result of using the consistent model through all twelve prediction cases, which in this case did not improve the prediction result. The additional nonlinearity near ultimate failure is also observed in the open hole compression tests.

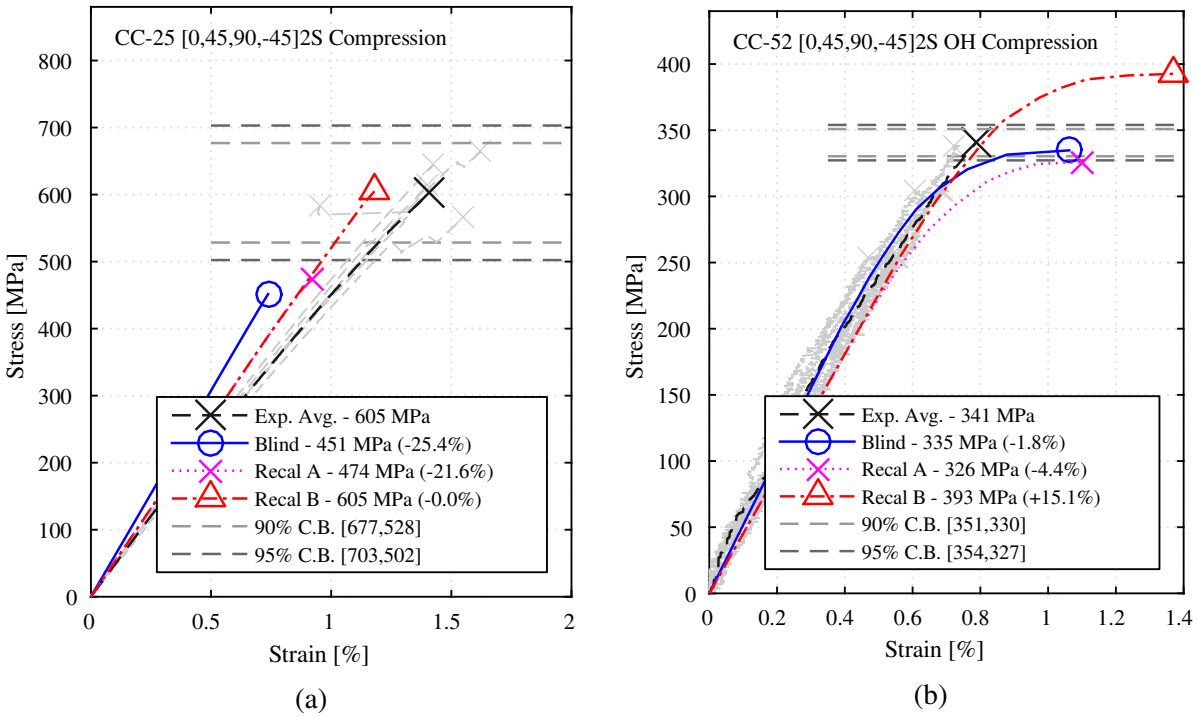

Figure 3.13: $[0,45,90,-45]_{2S}$ (a) Unnotched and (b) Open-Hole Compression Experiments and Blind/Recalibrated Stress vs. Strain Curves.

Damage contour plots from the recalibrated multiscale analysis (Recal. B) are compared to the experimental X-ray CT images at 90% of the static ultimate strength of the $[0,45,90,-45]_{2S}$ open hole tension experiment in Figure 3.14. The predicted damage patterns did not change significantly from the blind predictions to the recalibrated simulations, thus for brevity only the recalibrated results are shown. Due to the partitioning of the ROM, it is possible to directly interpret separate failure modes in the composite from the presence of damage in the different ROM parts as shown in

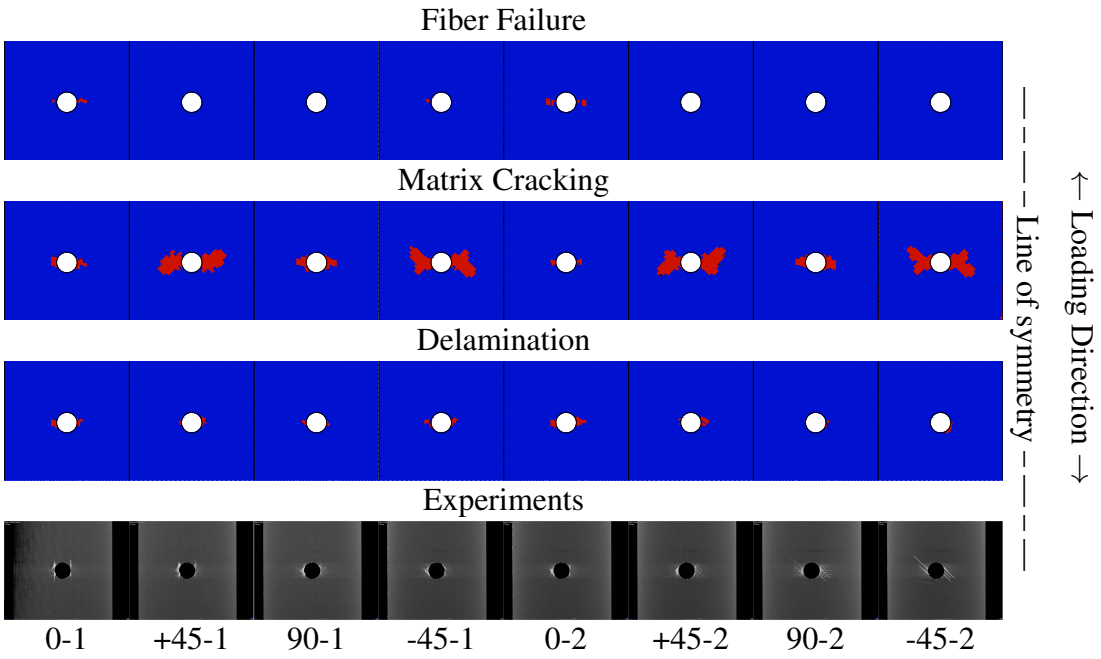

Figure 3.14: Static Damage Contours for $[0,45,90,-45]_{2S}$ Layup at 90% Ultimate Strength.

Figure 3.1. Fiber failure at a quadrature point corresponds to damage in part 1 of the ROM reaching unity. The matrix cracking and delamination are similarly interpreted from damage values in parts 2 and 3, respectively. When the corresponding damage values reach unity in an element, the entire element is highlighted as shown in Figure 3.14. Damage in the $[0,45,90,-45]_{2S}$ open hole layup under tension is dominated by transverse matrix cracking around the hole, primarily in the 90° and $\pm 45^\circ$ plies. The damage initiates near the hole and extends outward in the direction of fibers in each of the 90° and $\pm 45^\circ$ plies. In the $\pm 45^\circ$ plies, some additional damage accumulation propagating transverse to the fiber direction is predicted. A small amount of matrix damage around the hole in the 0° plies is also observed, indicating the presence of fiber splitting. This matrix damage behavior is consistent between the simulated damage contours and the CT images. The small amount of fiber failure at the hole in the 0° plies predicted in the simulations does not appear in the CT images. The simulation also predicts a small amount of delamination around the hole, predominantly near the 0° plies. The presence of such delaminations can be seen in the CT images as well.

3.1.6.2 [30,60,90,-60,-30]$_{2S}$ Layup

The [30,60,90,-60,-30]$_{2S}$ layup is a "soft" layup that contains no 0° plies. The strength of this layup is therefore markedly lower than the other two layups. The average error in this layup increased from 8.5% to 12.7% in terms of ultimate strength predictions after full recalibration using the increased longitudinal compression strength (Recal. B). Using the original longitudinal compression strength value of 1274 MPa and only accounting for the tension/compression anisotropy of the effective longitudinal elastic stiffness (i.e., Recal. A), the average error in laminated strength was reduced to 6.5%. The recalibration improved the average error in the prediction of the laminate stiffness for the [30,60,90,-60,-30]$_{2S}$ layups from 13.7% in the blind predictions to 4.9%. The impact of the longitudinal compression strength and elastic modulus on this soft layup is significant, given that the layup contains no 0° plies. The ultimate strength was over-predicted in blind prediction and after recalibration in both the open hole and unnotched tension tests of the [30,60,90,-60,-30]$_{2S}$ layup, as shown in Figure 3.15. The reduced effective longitudinal compression modulus value in recalibration reduced the ultimate strength prediction for the unnotched specimen (Figure 3.15a) and increased the ultimate strength prediction in the open hole specimen (Figure 3.15b). In both cases, the prediction error after recalibration was approximately 10%.

In the [30,60,90,-60,-30]$_{2S}$ compression tests shown in Figure 3.16, the accuracy of the predicted stiffness was significantly improved after recalibration from errors of 21.2% and 17.6% for the unnotched and open hole compression tests, respectively, to 2.7% and 5.5%, respectively, after recalibration (Recal. B). The increased longitudinal compression strength after recalibration resulted in a slightly larger prediction error in the [30,60,90,-60,-30]$_{2S}$ layups under compression loading.

Figure 3.17 displays the damage contour comparison between the recalibrated simulation and the experiments at 90% of the ultimate static strength of the specimen. Similar to the [0,45,90,-45]$_{2S}$ layup, the dominant failure mode is transverse matrix cracking. In the $\pm 60^\circ$ plies, the matrix is completely failed in the load ligament regions. There is also significant matrix damage in the $\pm 30^\circ$ and 90° plies both originating at the open hole and at the edges of the specimen. Minor

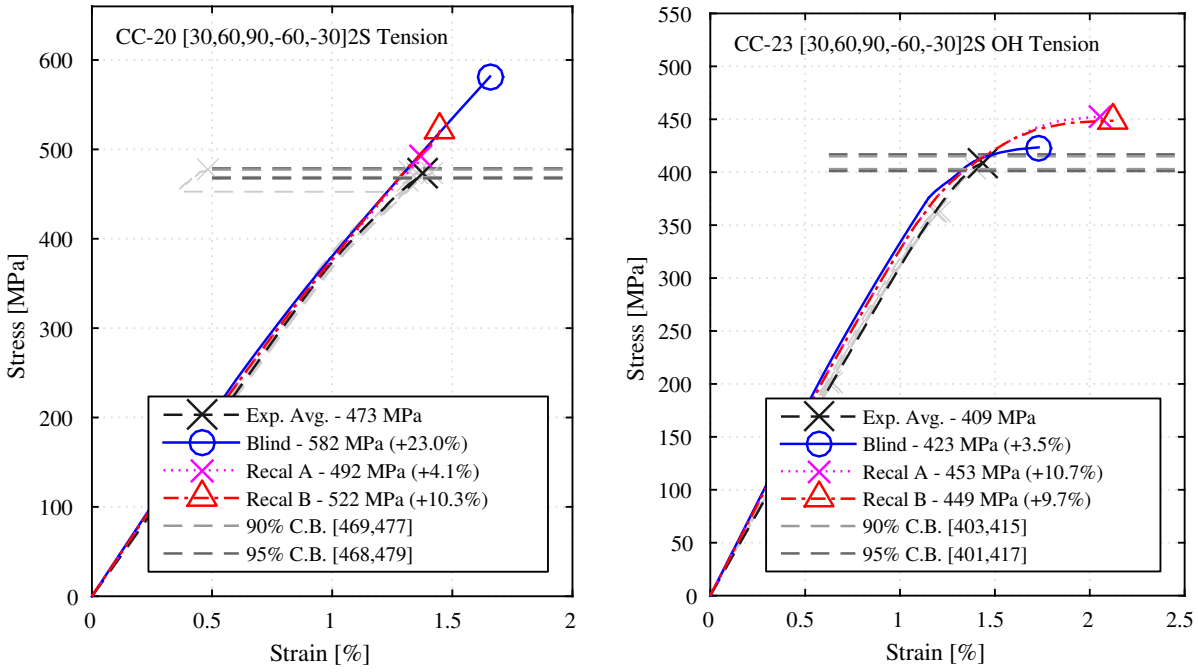

(a) (b)

Figure 3.15: $[30,60,90,-60,-30]_{2S}$ (a) Unnotched and (b) Open-Hole Tension Experiments and Blind/Recalibrated Stress vs. Strain Curves.

delamination regions are predicted around the hole in each ply as well.

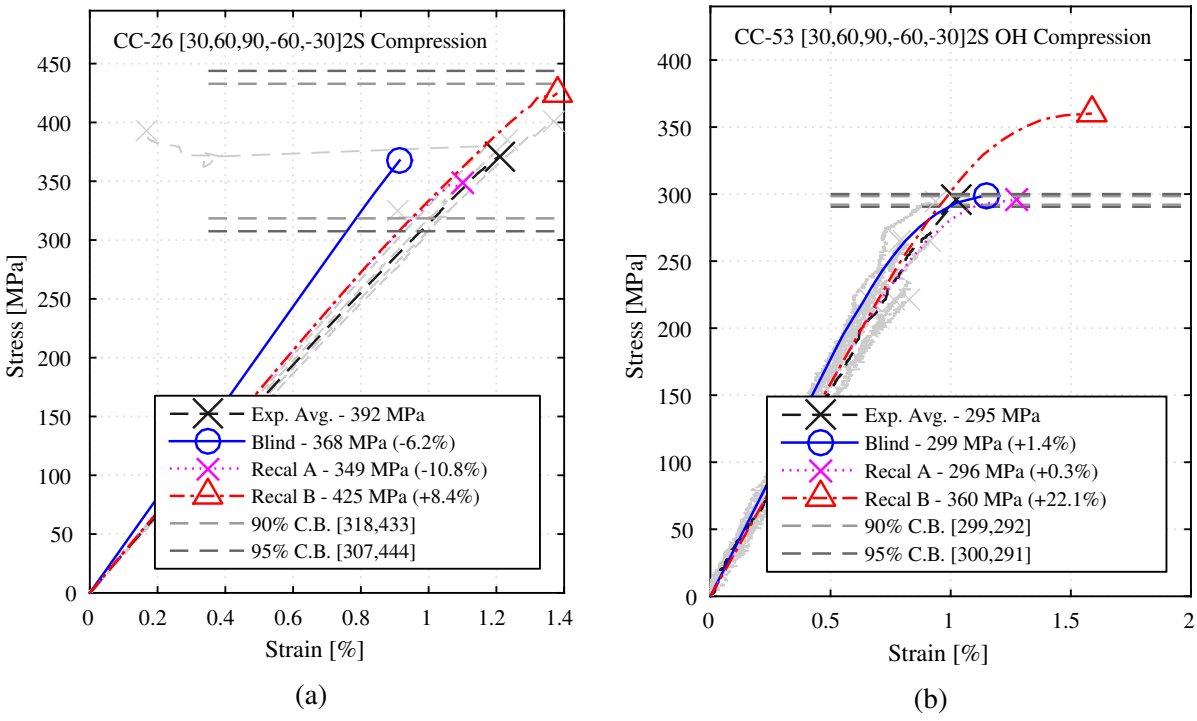

Figure 3.16: $[30,60,90,-60,-30]_{2S}$ (a) Unnotched and (b) Open-Hole Compression Experiments and Blind/Recalibrated Stress vs. Strain Curves.

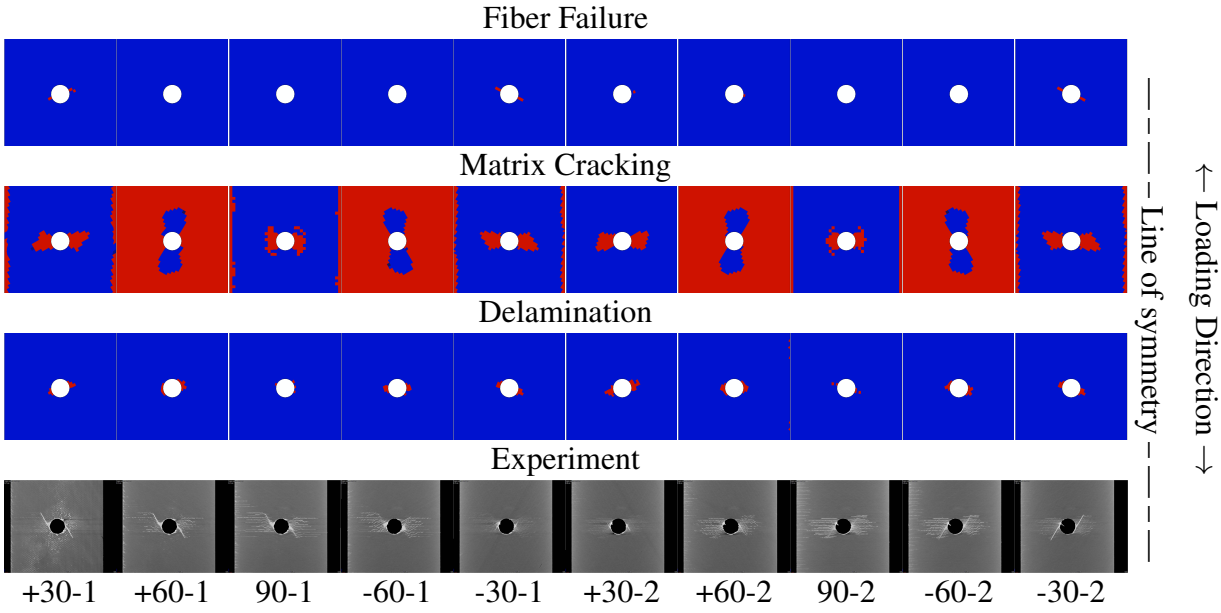

Figure 3.17: Static Damage Contours for $[30,60,90,-60,-30]_{2S}$ Layup at 90% Ultimate Strength.

3.1.6.3 [60,0,-60]$_{3S}$ Layup

Figure 3.18 shows the tensile loading results for the [60,0,-60]$_{3S}$ specimen with the unnotched and open-hole configurations. The recalibration of the model to account for the tension/compression anisotropy of the longitudinal compression stiffness (Recal. A) resulted in an improvement from 20.2% error in the blind prediction to less than 1% error after recalibration for the unnotched configuration. For the unnotched case, correcting for the longitudinal compression strength of the 0° lamina had only a minor impact on the predicted ultimate strength. In the [60,0,-60]$_{3S}$ open hole tension specimen, recalibration of the model did not significantly improve the prediction result. In all cases for the open hole tension specimen, the prediction error was between 7.6% and 10.3% (see Figure 3.18b).

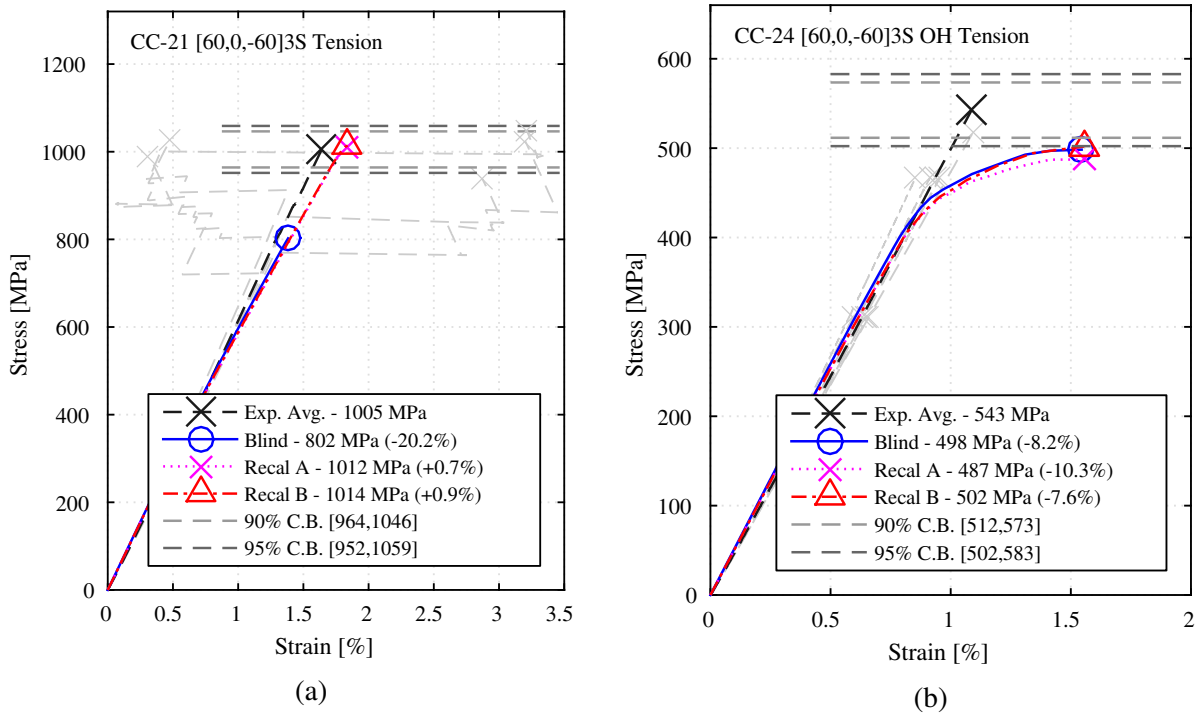

Figure 3.18: [60,0,-60]$_{3S}$ (a) Unnotched and (b) Open-Hole Tension Experiments and Blind/Recalibrated Stress vs. Strain Curves.

The ultimate strength of the [60,0,-60]$_{3S}$ unnotched compression test was under-predicted by a large margin in both blind prediction and recalibration, as displayed in Figure 3.19a. The blind prediction had 42.9% error and after recalibration the error improved to 21.3%. This case repre-

sented the largest prediction error for all twelve specimens. The prediction of the $[60,0,-60]_{3S}$ open hole compression strength in Figure 3.19b was significantly improved in recalibration from 13.1% in blind prediction to 2.8% after recalibration.

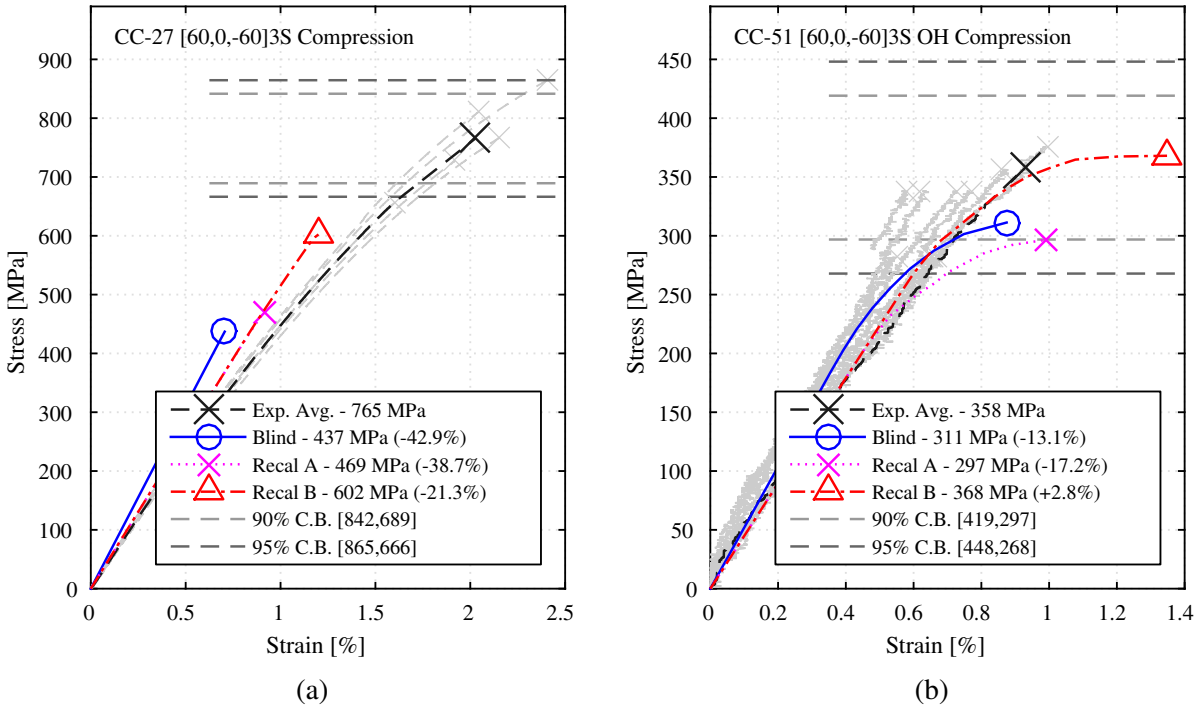

Figure 3.19: $[60,0,-60]_{3S}$ (a) Unnotched and (b) Open-Hole Compression Experiments and Blind/Recalibrated Stress vs. Strain Curves.

The damage contour plots for the $[60,0,-60]_{3S}$ specimen with the open hole in tension at 90% of the ultimate static strength are displayed in Figure 3.20 for both the recalibrated prediction and the experiments. In the simulation of damage evolution, the accumulation of transverse matrix damage is significantly over-predicted in the $\pm 60^{\circ}$ plies as compared with the experiments. The higher degree of ductility observed in the prediction of stress-strain curves are consistent with and caused by this over-predicted damage extent in the simulations. Matrix cracks are observed in the CT images, but at a lesser degree than in the prediction. The simulation does predict the accumulation of transverse matrix cracks in the 0° plies adjacent to the hole, accompanied by small regions of delamination. This is consistent with the vertical fiber splitting cracks observed in the CT images adjacent to the open hole in the 0° plies. The simulation also predicts the initiation of fiber failure in the 0° plies near the open hole at the 90% ultimate strength load.

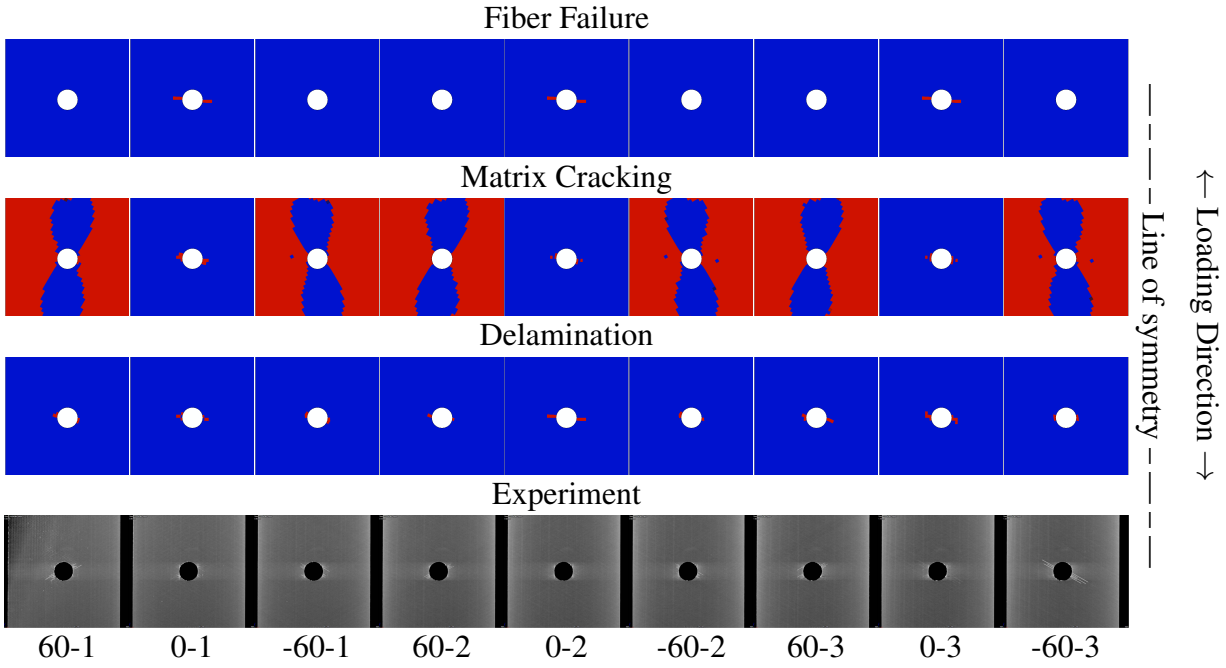

Figure 3.20: Static Damage Contours for [60,0,-60]$_{3S}$ Layup at 90% Ultimate Strength.

3.2 Damage Tolerance Design Principles Program - Fatigue Predictions

The fatigue prediction portion of the DTDP program took place directly following the completion of the static recalibration phase. The calibrated EHM model for fatigue predictions was characterized by the material parameters identified in the recalibration of the static prediction model and the cycle-sensitivity parameters calibrated from a suite of fatigue-life experiments provided by the AFRL. In the third phase of the DTDP program, blind predictions of laminated composite fatigue stiffness-life curves, compressive and tensile residual strength after fatigue, and accumulated damage contour plots after fatigue were predicted using the calibrated EHM model for the three composite layups ([0,45,90,-45]$_{2S}$, [30,60,90,-60,-30]$_{2S}$, and [60,0,-60]$_{3S}$) with open hole configurations. The fourth phase of the program consisted of the recalibration of the EHM model following the distribution of the experimental results for the blind prediction cases. This work is expected to be published in a forthcoming special issue of the Journal of Composite Materials [19].

3.2.1 Experiments

Similar to the static prediction portion, in the fatigue prediction phases, two sets of experimental data were released separately to the program participants. The first set of experiments was delivered at the start of the blind prediction phase in order to calibrate the cyclic damage evolution behavior of the model. This data set included 0° and 90° tension-tension, 90° three point bending, $\pm 45^\circ$ tension-tension, and end notch flexure fatigue experiments. In each case, the stiffness vs. cycles curves for a range of applied stress amplitudes were provided. In the fatigue recalibration phase, the results of the $[0,45,90,-45]_{2S}$, $[30,60,90,-60,-30]_{2S}$, and $[60,0,-60]_{3S}$ layups with open hole configuration under tension-tension fatigue were reported, in addition to the residual strength after fatigue in tension and compression and the X-ray CT images of damage progression for each of these layups. The applied stress amplitude for the $[0,45,90,-45]_{2S}$ layup was 50% of the mean static ultimate strength for the layup, for the $[60,0,-60]_{3S}$ layup was 80%, and for the $[30,60,90,-60,-30]_{2S}$ layup was 40%. Residual strength after fatigue was tested after 300K cycles for the $[0,45,90,-45]_{2S}$ layup and after 200K cycles for the $[30,60,90,-60,-30]_{2S}$ and $[60,0,-60]_{3S}$ layups. In each case for the calibration and prediction experiments, the fatigue load was applied at 10Hz with an R-ratio of 0.1. The geometry of each of these specimens was consistent with those delivered in the static phase (Table 3.1).

3.2.2 Calibration

Eight material parameters ($a^{(m)}$, $b_n^{(m)}$, $b_s^{(m)}$, $c^{(m)}$, $\upsilon_0^{(m)}$, $d_0^{(m)}$, $d_1^{(m)}$, and $d_2^{(m)}$) were used in the EHM model to calibrate the damage evolution properties of the matrix and seven properties ($a^{(f)}$, $b^{(f)}$, $c^{(f)}$, $\upsilon_0^{(f)}$, $d_0^{(f)}$, $d_1^{(f)}$, $d_2^{(f)}\}$ were used for the fiber. The values for these parameters are presented in Table 3.6. An additional column is included in the table showing the delamination part parameters which were included only in the recalibrated EHM model. The majority of the parameters were carried over from the recalibrated EHM model from the static prediction phases of the DTDP program. The only additional parameters calibrated in the blind prediction phase

were the factors controlling the cycle-sensitivity parameter from Equation 2.42.

Table 3.6: Calibrated Material Damage Evolution Properties for DTDP Fatigue Predictions.

Property	Fiber	Matrix	Delamination
a	0.050562	0.001592	0.018
b_n	274	15	304 .0
b_s	-	-3.2	9.45
c	1.4481	0.535	0.492
υ_0	1367	636.2	0
d_0	10.735	6.0	6.0
d_1	-2.068×10^{-3}	-3.0×10^{-3}	-6.0×10^{-3}
d_2	-1.04×10^{-10}	-2.62×10^{-10}	-2.62×10^{-10}

The applied stress vs. cycles to failure (S-N) curves for the 90° three point bending fatigue experiments were used to calibrate the matrix parameters, $d_0^{(m)}$, $d_1^{(m)}$, and $d_2^{(m)}$ and the S-N curves from the 0° tension-tension fatigue experiments were used to calibrate the fiber parameters: $d_0^{(f)}$, $d_1^{(f)}$, and $d_2^{(f)}$. In both cases the optimization was performed using the Nelder-Mead simplex method [67] minimizing the discrete L_2 norm of the differences between the experimental power law fit for cycles to failure and the simulated cycles to failure for a number of stress amplitudes along the S-N curve for the respective experiment. The resulting calibrated S-N curves are shown in Figure 3.21. The calibration method was able to generate a model which very closely matches the power law fit for the experiments.

3.2.3 Blind Prediction

The calibrated EHM model was exercised to predict the S-N curves, progressive damage accumulation contours, and residual strength after fatigue in tension and compression for the $[0,45,90,-45]_{2S}$, $[30,60,90,-60,-30]_{2S}$, and $[60,0,-60]_{3S}$ specimens with open-hole configurations under tension-tension fatigue. The macroscale specimen models used in the fatigue predictions were identical to the corresponding numerical specimens employed in the static phase. In the cyclic fatigue analysis, a pinned boundary was applied to one end of the specimen constraining displacement in the coupon longitudinal direction, and a monotonically increasing displacement

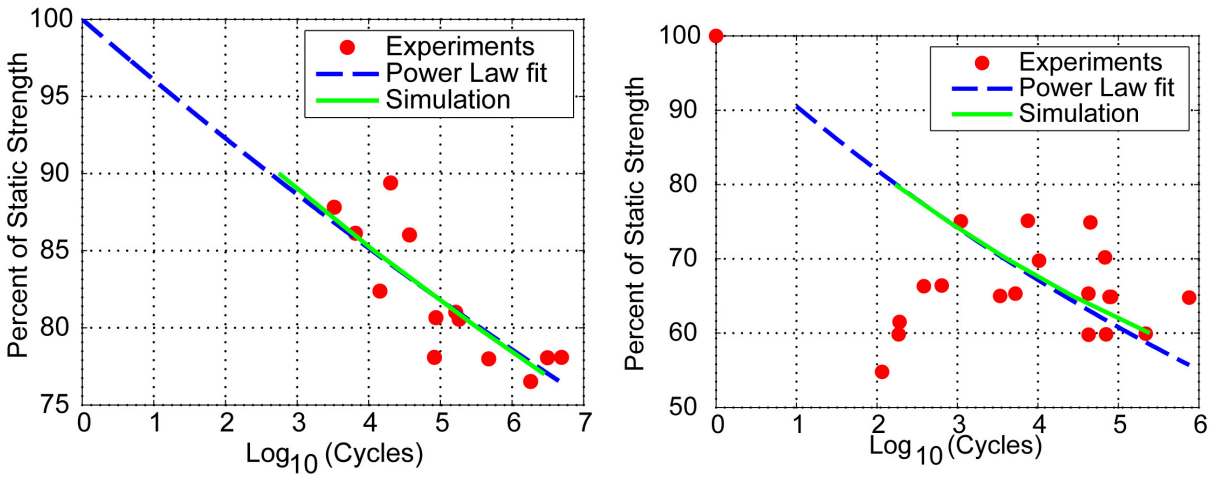

Figure 3.21: Fatigue Stress vs. Life for (a) 0° Tension-Tension Fatigue and (b) 90° Three Point Bending Fatigue.

was applied to the opposite end for the microchronological analysis of a single load cycle. In the macrochronological step, the displacement was held at the fixed point as the damage over the cycle-jump was gradually applied to the coupon, satisfying stress equilibrium through the application of damage. For the prediction of residual strength after fatigue, the internal damage state for the coupon after the appropriate number of loading cycles was stored, and a monotonically increasing displacement was applied to the pre-damaged specimen until failure. In the multitemporal analysis, the average damage over the entire macrostructure was limited to a value of $\Delta D_{max} = 0.01$ from Equation 2.35.

3.2.4 Recalibration

A clear deficiency in the model predictions for the [60,0,-60]$_{3S}$ specimen was observed from the blind predictions. The blind prediction of fatigue life for this specimen was 700 cycles, whereas the experimental specimens each ran out to 2M cycles. One hypothesis for this discrepancy was that the role of interlaminar shear and delamination was not accurately captured by the EHM blind prediction model. In order to recalibrate the model to capture the interlaminar shear behavior, the information from the end notch flexure static and fatigue experiments was utilized. These

experiments were provided in the calibration experiment data from the AFRL for the respective static and fatigue phases, but were not used in the static predictions or the fatigue blind prediction calibration. To better represent delamination effects in the EHM model, the constituent material parameters of part 3 in the ROM were adjusted to match the ENF static and fatigue experiments, as shown in Figure 3.22. These material parameters are reported in Table 3.6. Additionally, the 0° plies in the [60,0,-60]$_{3S}$ were modeled with 3 elements per ply thickness to better capture the macroscale localization of delamination effects. This resulted in a significant computational cost increase for this layup, but the resulting simulation performed much better than the blind prediction case.

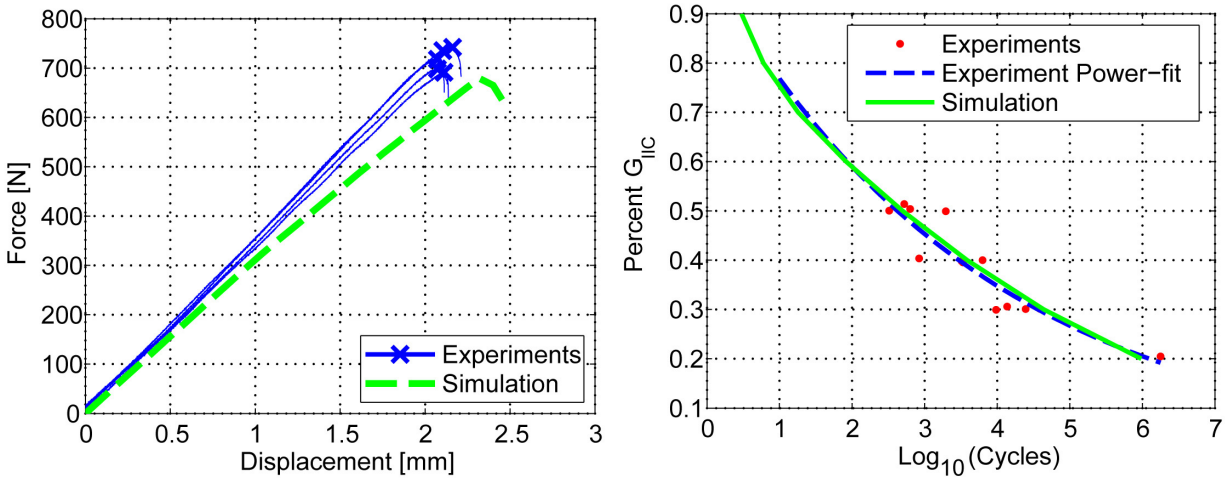

(a) (b)

Figure 3.22: Calibrated Model Comparisons with ENF tests for (a) Stress vs. Strain in Static Loading and (b) Critical Energy vs. Life in Fatigue.

3.2.5 Results and Discussion

The results from the fatigue prediction study are divided into three main areas of interest: stiffness vs. cycles, residual strength after fatigue in tension and compression, and progressive damage contour plots.

3.2.5.1 *Stiffness vs. Cycles under Fatigue*

Each of the three open hole layups were cycled under tension-tension fatigue with an R-ratio of 0.1 up to 2 million cycles or failure. The applied loading was 50% of the static ultimate strength for the $[0,45,90,-45]_{2S}$ layup, 40% for the $[30,60,90,-60,-30]_{2S}$ layup and, 80% for the $[60,0,-60]_{3S}$ layup. In both blind predictions and recalibration, the $[0,45,90,-45]_{2S}$ and $[30,60,90,-60,-30]_{2S}$ simulations matched reasonably well with the experiments. The prediction of the stiffness degradation curve as a function of number of load cycles for the $[0,45,90,-45]_{2S}$ layup compared with the individual experiments (Figure 3.23) shows that the simulation predicts the initial stiffness drop over the first few thousand cycles and the following stiffness plateau. The simulation does not predict failure in the specimen, which is observed to occur suddenly over a wide range of cycles-to-failure in the experiments. The simulated stiffness plateau and runout behavior of the $[30,60,90,-60,-30]_{2S}$ experiments and simulations are shown in Figure 3.24, and were found to be largely in good agreement with the experiments. The recalibration of the EHM model had only minor effects on the stiffness vs. cycles behavior for the $[0,45,90,-45]_{2S}$ and $[30,60,90,-60,-30]_{2S}$ specimens.

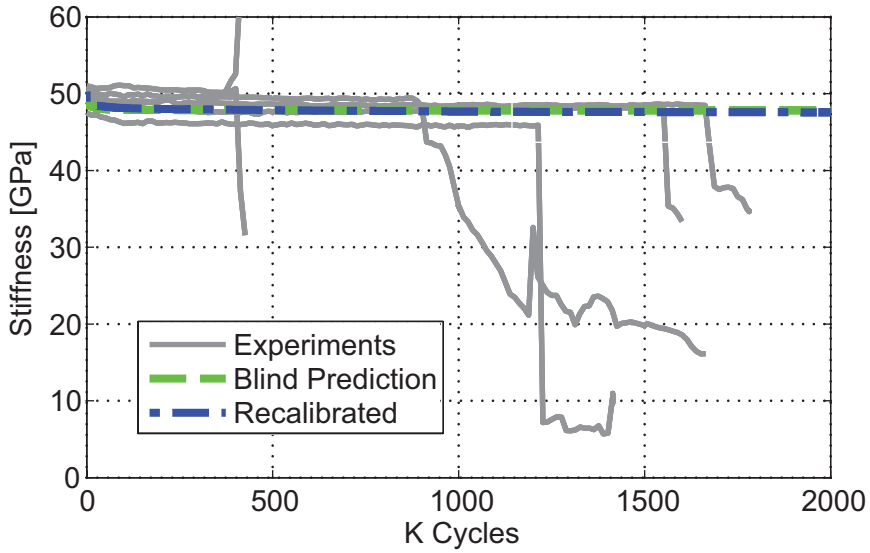

Figure 3.23: Stiffness vs. Cycles for $[0,45,90,-45]_{2S}$ Layup under Tension-Tension Fatigue.

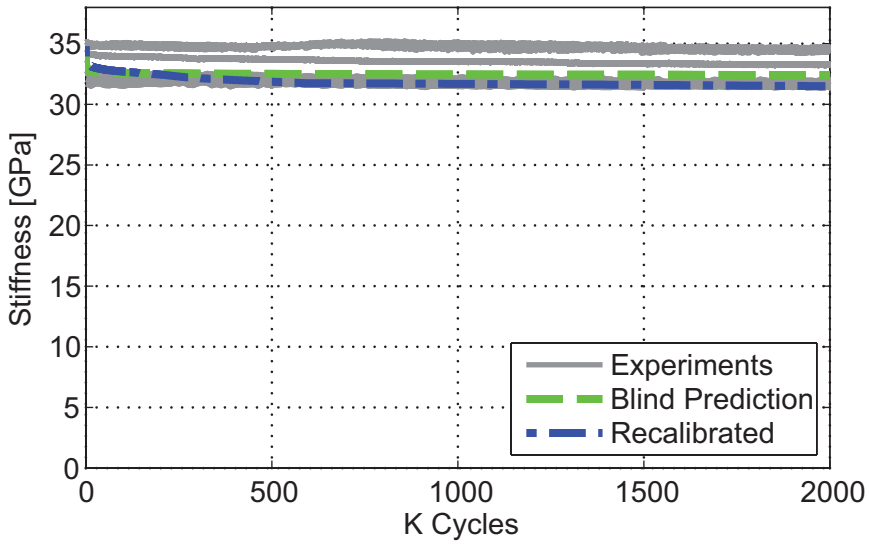

Figure 3.24: Stiffness vs. Cycles for [30,60,90,-60,-30]$_{2S}$ Layup under Tension-Tension Fatigue.

In blind predictions, the EHM prediction of the stiffness vs. cycles response of the [60,0,-60]$_{3S}$ specimen deviated from the observed behavior as shown in Figure 3.25. This layup contains the largest percentage of 0° plies and the applied load level of 80% is the greatest percentage of static ultimate strength over all three layups. In blind prediction, failure of the [60,0,-60]$_{3S}$ layup is predicted after 700 cycles, whereas in the experiments there is a pronounced stiffness drop but the specimens each continue to runout at 2 million cycles. In the fourth phase of the DTDP program, the EHM model was recalibrated to better handle interlaminar shear calibrated to the results of the ENF tests in static and fatigue loading. In the experiments, each replicate displayed a gradual stiffness degradation over time from an average stiffness of 51.2 GPa at the first cycle to 39.3 GPa after 2M cycles. This amounted to a 23% degradation of stiffness. In the recalibrated simulation, the stiffness dropped from an initial value of 51.2 GPa to 34.8 GPa over 100K cycles, where the stiffness remained at 34.8 GPa up to run out at 2M cycles. The pattern of damage accumulation leading to this behavior in the experiments and numerical specimens is described in Section 3.2.5.3 and the rationale behind the recalibration and the underlying phenomenological behavior is further explored in Section 3.3.

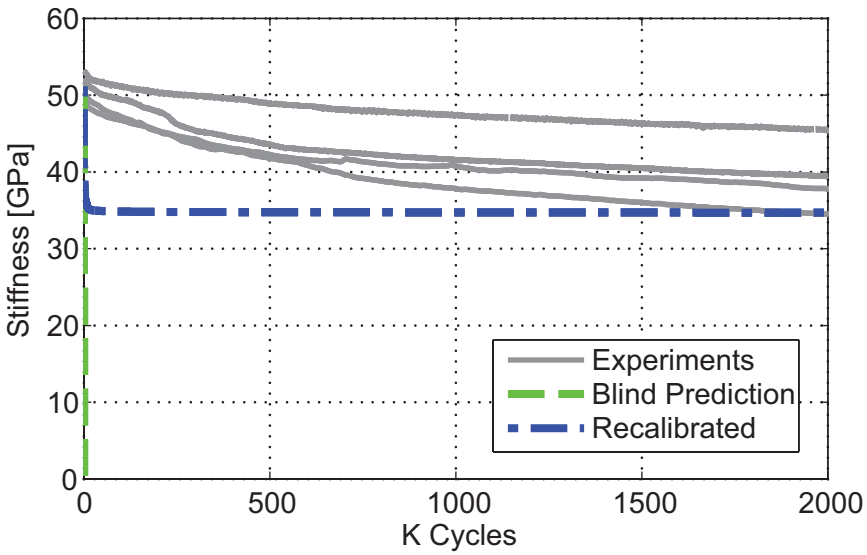

Figure 3.25: Stiffness vs. Cycles for $[60,0,-60]_{3S}$ Layup under Tension-Tension Fatigue.

3.2.5.2 Residual Strength after Fatigue

The residual strength in tension and compression after tension-tension fatigue was predicted after 300K cycles for the $[0,45,90,-45]_{2S}$ layup and after 200K cycles for the $[30,60,90,-60,-30]_{2S}$ and $[60,0,-60]_{3S}$ layups. In Figures 3.26 - 3.28, the stress vs. strain curves for the residual strength experiments are compared to the blind and recalibrated predictions. Additionally, the experimental mean and the predicted *static* strength from the static recalibration are shown for comparison.

The residual strength predictions for the $[0,45,90,-45]_{2S}$ layup are shown in Figure 3.26. The strength reduction after fatigue for the specimen in tension was 2.0%, comparing the static and residual experimental mean ultimate strength. In compression a 7.0% strength drop was observed. This behavior is well captured when comparing the simulated static strength and the simulated residual strength after fatigue. For tension there is a 2.1% drop in strength after fatigue in the simulations. For compression there is predicted drop of 6.7% strength. These values are in very good agreement with the experiments. In this layup, the nonlinearity in the curve due to high predicted damage extent in the residual strength prediction is still visible.

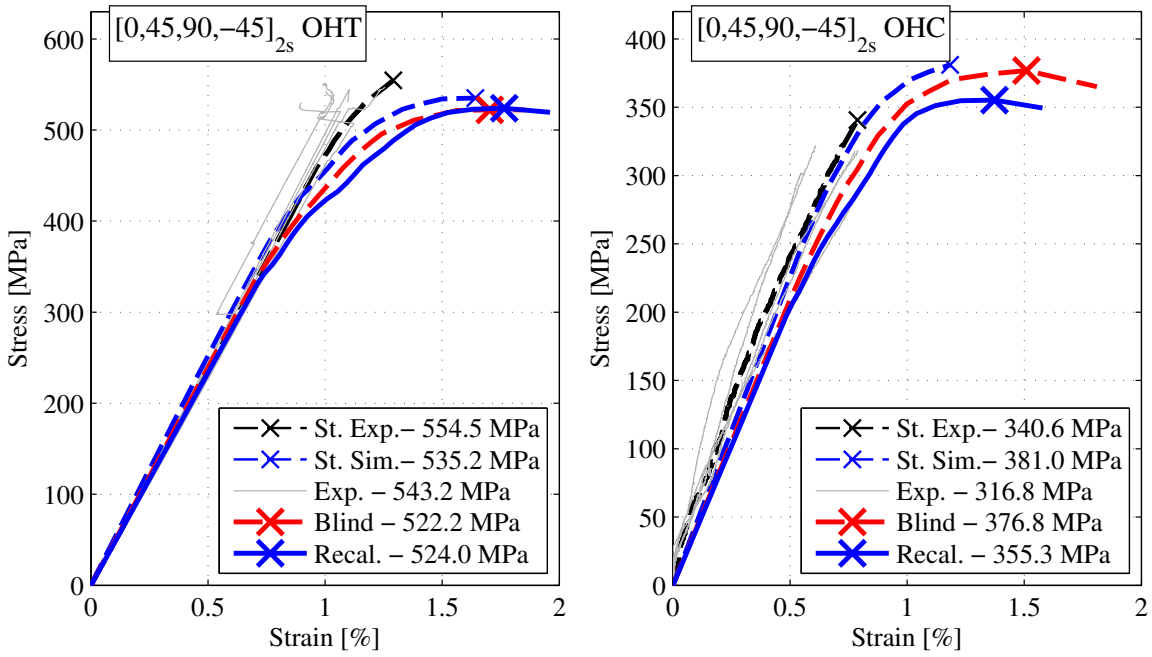

Figure 3.26: Residual Strength after 300K Cycles for [0,45,90,-45]$_{2S}$ Layup in (a) Tension and (b) Compression.

Figure 3.27 shows the residual strength predictions for the [30,60,90,-60,-30]$_{2S}$ layups in tension and compression. The recalibration step to account for interlaminar shear strength significantly increased the residual strength predictions for this layup in both tension and compression. In tension experiments, a slight 3.6% increase in residual strength over static ultimate strength was observed, whereas a 7.0% drop was observed in compression experiments. In both tension and compression, the recalibrated model predicts a drop of 11.7% and 12.6% for tension and compression residual strength, respectively. The increase in tension residual strength for the experiments is an interesting effect for this layup as there are no 0° plies. This increase may be within the experimental error range for this layup and may not be due to increase in strength induced by stress redistribution, as in the case of the [60,0,-60]$_{3S}$ layup. It is also possible that there are further phenomenological effects that have not been captured in the calibration process which account for this behavior. It is noted that no calibration data was available to characterize the behavior of $\pm 30^\circ$ or $\pm 60^\circ$ plies directly. Only data from 0° and 90° plies were provided to calibrate longitudinal and

transverse behavior and $\pm 45^\circ$ data to calibrate shear behavior. These tests might not be adequate to calibrate the mixed loading mode behavior in the 30° and 60° plies which will experience loading between the uniaxial and pure shear conditions provided for calibration.

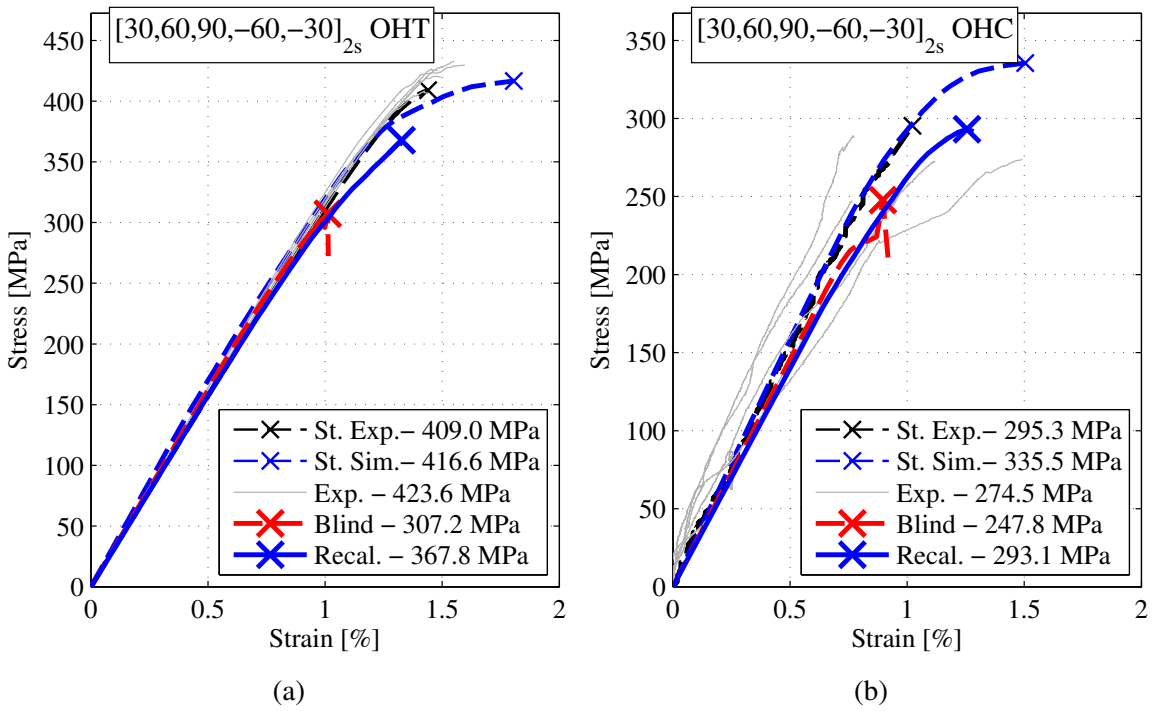

Figure 3.27: Residual Strength after 200K Cycles for [30,60,90,-60,-30]$_{2S}$ Layup in (a) Tension and (b) Compression.

No blind prediction of residual strength was made for the [60,0,-60]$_{3S}$ layup due to the early failure of the simulation under fatigue. However, the recalibrated model predictions of residual strength were in reasonable agreement with the experiments in Figure 3.28. There was a 24.4% *increase* in residual strength in tension after fatigue in the experiments. This is caused by the fiber splitting and stress shielding effects around the open hole (see Section 3.3). The recalibrated prediction model is able to capture the general trend of this behavior as well, predicting a strength increase of 14.6% in the residual strength after fatigue for tension. The effect of the rapid stiffness drop in the simulation of this layup from fatigue is shown in Figure 3.28(a), accounting for the stiffness discrepancy. In compression, the experiments show a 5.6% increase in strength after fatigue. This is not captured in the simulations, where a 2.8% drop in strength is predicted. In both

residual strength predictions of this layup, the artificial nonlinearity in the curve that was seen in the static results is not present.

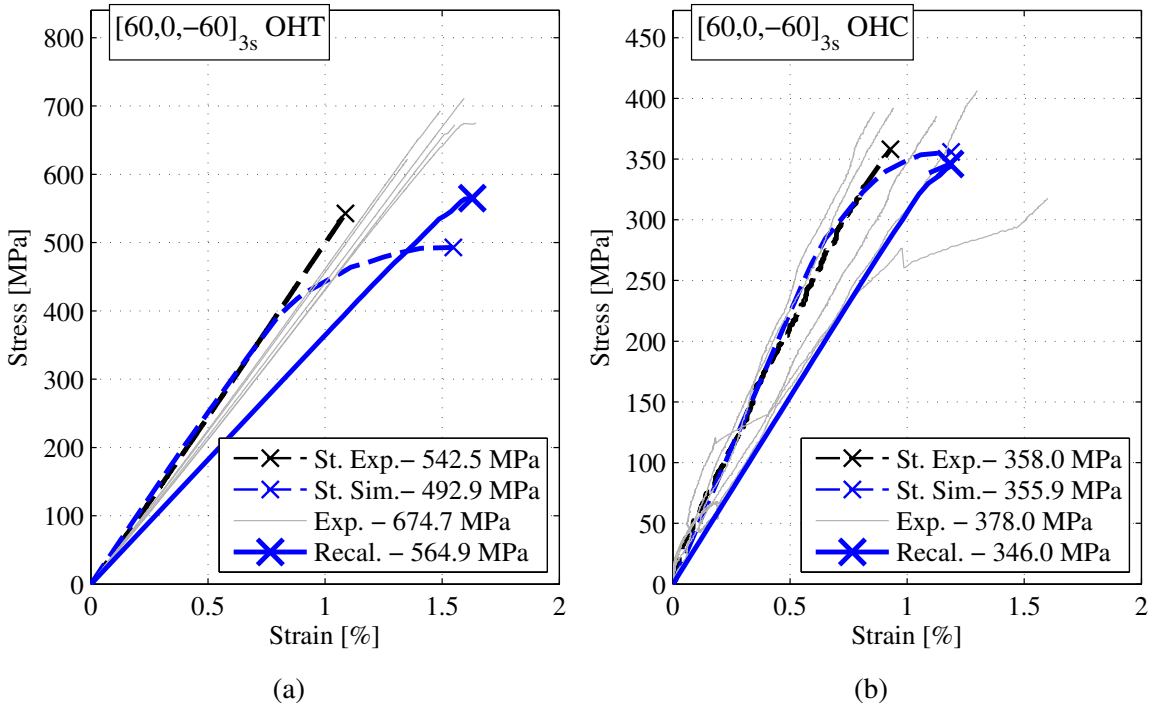

Figure 3.28: Residual Strength after 200K Cycles for [60,0,-60]$_{3S}$ Layup in (a) Tension and (b) Compression.

3.2.5.3 Damage Contour Plots from Fatigue Loading

Damage contour plots comparing the prediction of damage accumulation in the fatigue simulations and the X-ray CT images of experimental damage are included in this section. Figures 3.29-3.31 show the ply-by-ply damage accumulation corresponding to fiber failure, transverse matrix cracking, and delamination from the recalibrated fatigue simulation alongside the experimental CT images displaying damage in the experiments for the [0,45,90,-45]$_{2S}$ layup after 300K fatigue cycles. The damage pattern is consistent between the simulations and the experiments. In the 0° plies, the growth of a small region of fiber splitting due to transverse matrix damage is seen in both the experiments and predictions. The major damage mode of transverse matrix cracking in the fiber direction of the $\pm 45^\circ$ plies is captured in the simulations. The fatigue loading rapidly leads

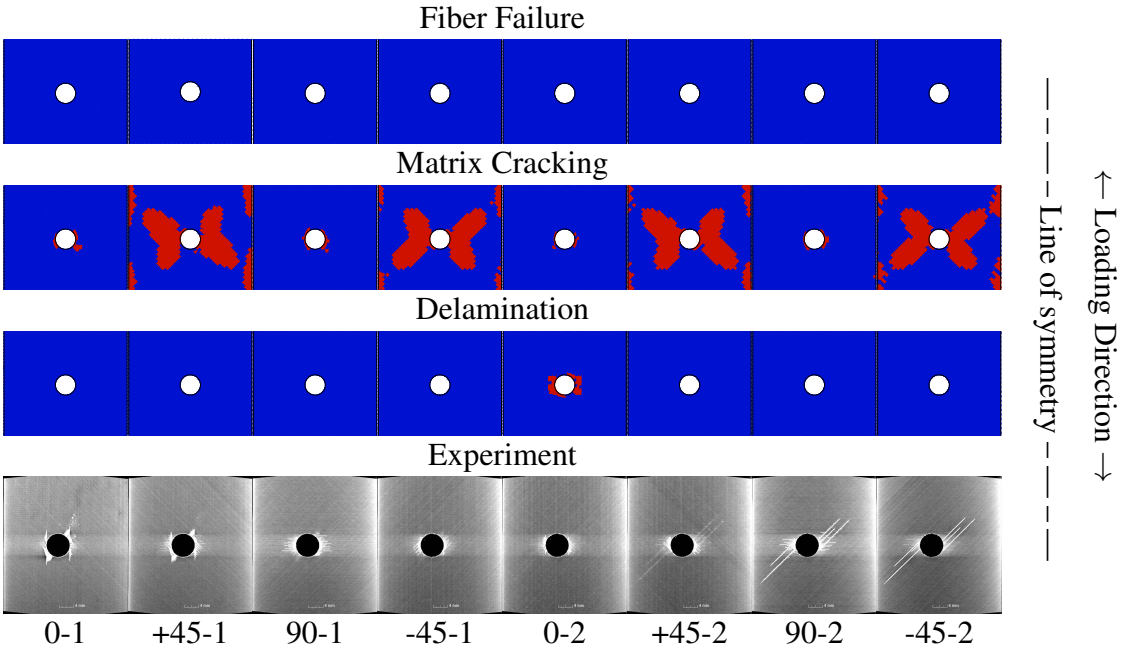

Figure 3.29: Fatigue Damage Contours for $[0,45,90,-45]_{2S}$ Layup after 100K Cycles.

to transverse matrix cracks over nearly the full width of the specimen in the $+45°$ and $-45°$ plies, with the cracks growing with additional cycles in both the simulations and the experiments. The presence of these matrix cracks is such a dominant effect that the cracks bleed through multiple plies. Matrix cracks are also present in the $90°$ plies near the hole, however the predicted matrix damage in the $90°$ plies was less than that observed in the experiments There is also evidence of delamination around the hole in the interior $0°$ ply which is predicted in the simulations, but the delamination regions near the fiber splitting is not observed in the simulations.

Damage accumulation in the $[30,60,90,-60,-30]_{2S}$ layup was predicted to occur predominantly in the $\pm 60°$ plies as seen in Figures 3.32-3.35. This is in good qualitative agreement with the experimental images, with the simulation predicting more damage than observed in the experiment. There is no fiber failure predicted in this layup. In the damage contours shown below, the general "X" pattern of damage in the $60°$ plies is predicted in the recalibrated simulations, but appears to be accumulating faster than the CT images show. The growth of damage at the hole near the stress concentration in the other plies developing around 150k cycles (Figure 3.34) is also visible

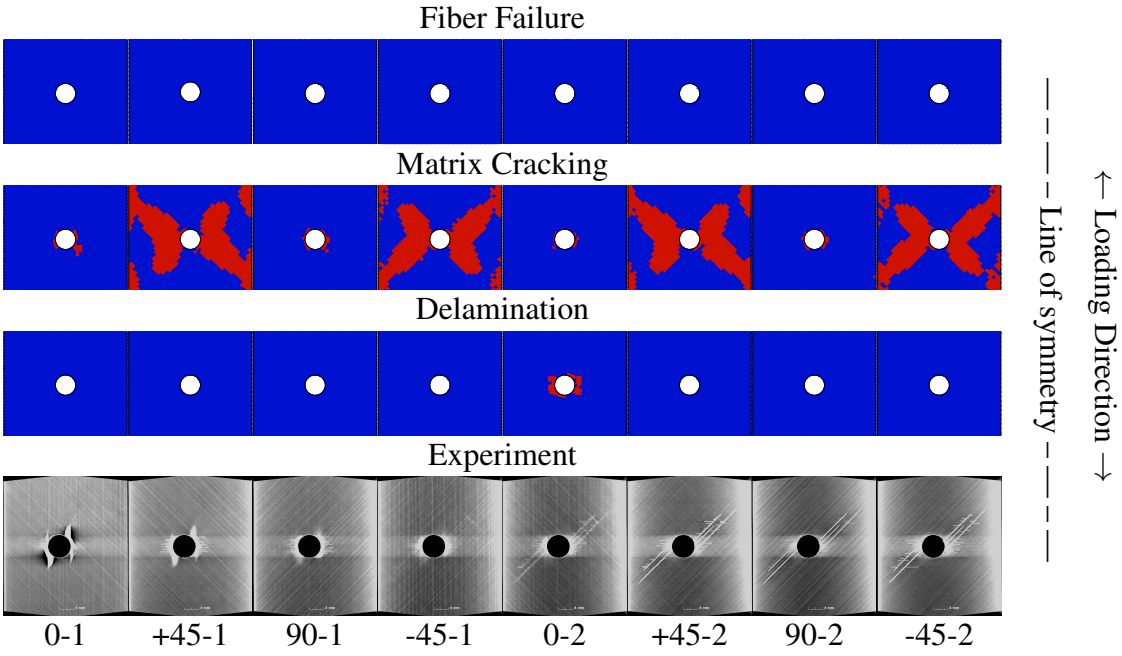

Figure 3.30: Fatigue Damage Contours for $[0,45,90,-45]_{2S}$ Layup after 200K Cycles.

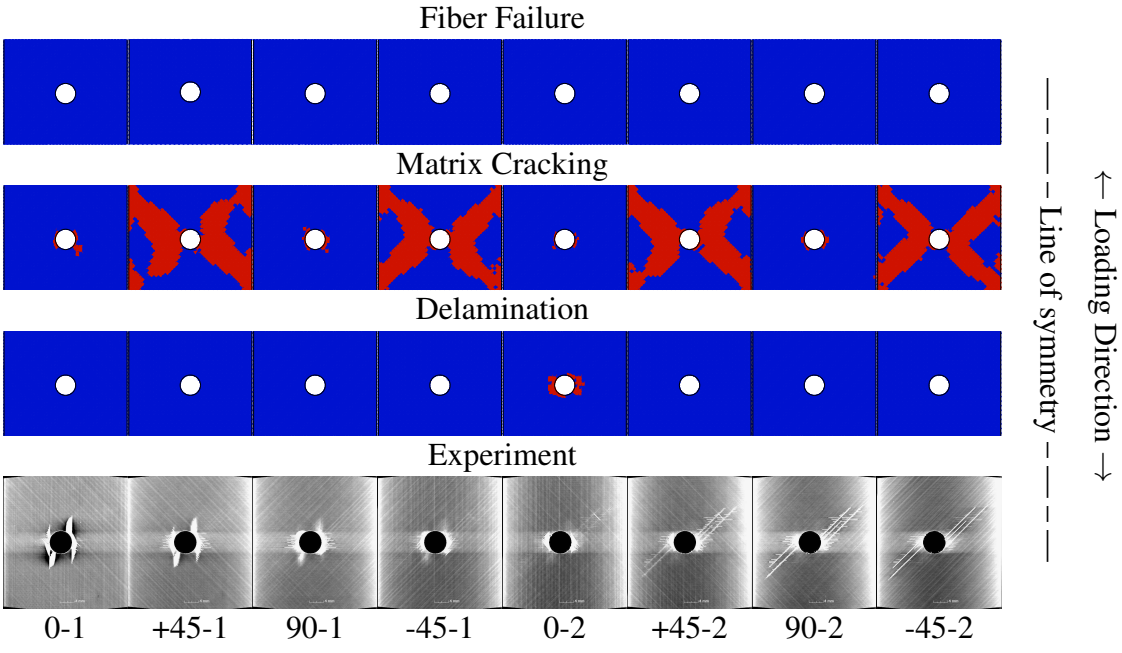

Figure 3.31: Fatigue Damage Contours for $[0,45,90,-45]_{2S}$ Layup after 300K Cycles.

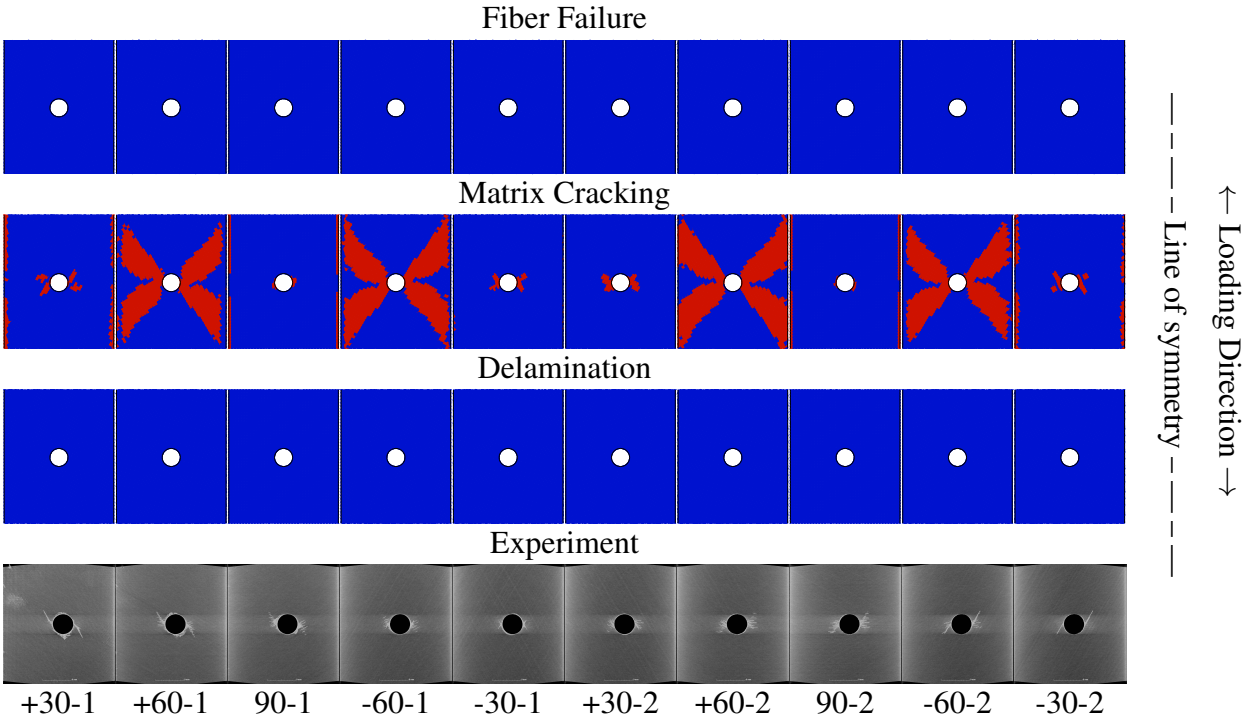

Figure 3.32: Fatigue Damage Contours for [30,60,90,-60,-30]$_{2S}$ Layup after 50K Cycles.

in the predicted damage contours. Delamination is not exhibited in the predicted contours, but delaminated regions are evident in the experimental images around the major cracks in the $\pm 30^{\circ}$ directions.

The recalibrated prediction of damage accumulation in the [60,0,-60]$_{3S}$ layup is in good qualitative agreement with the experiments in Figures 3.36-3.39, but progresses much more rapidly than in the experiments. The simulation displays much more significant delaminations than the CT images display, but the general pattern of the delamination in the 0° plies extending above and below the hole in the loading direction agrees well with the experiments. Additionally, the fiber splitting from transverse matrix damage on either side of the delamination region is well captured. The predominance of transverse matrix cracking is seen in the simulations and in the experiments with the large number of matrix cracks across the width of the specimen in the CT images of the $\pm 60^{\circ}$ plies, and the near complete predicted transverse matrix damage in the simulated $\pm 60^{\circ}$ plies. Fiber failure in the predictions is limited to the delaminating region, with no fiber failure propagat-

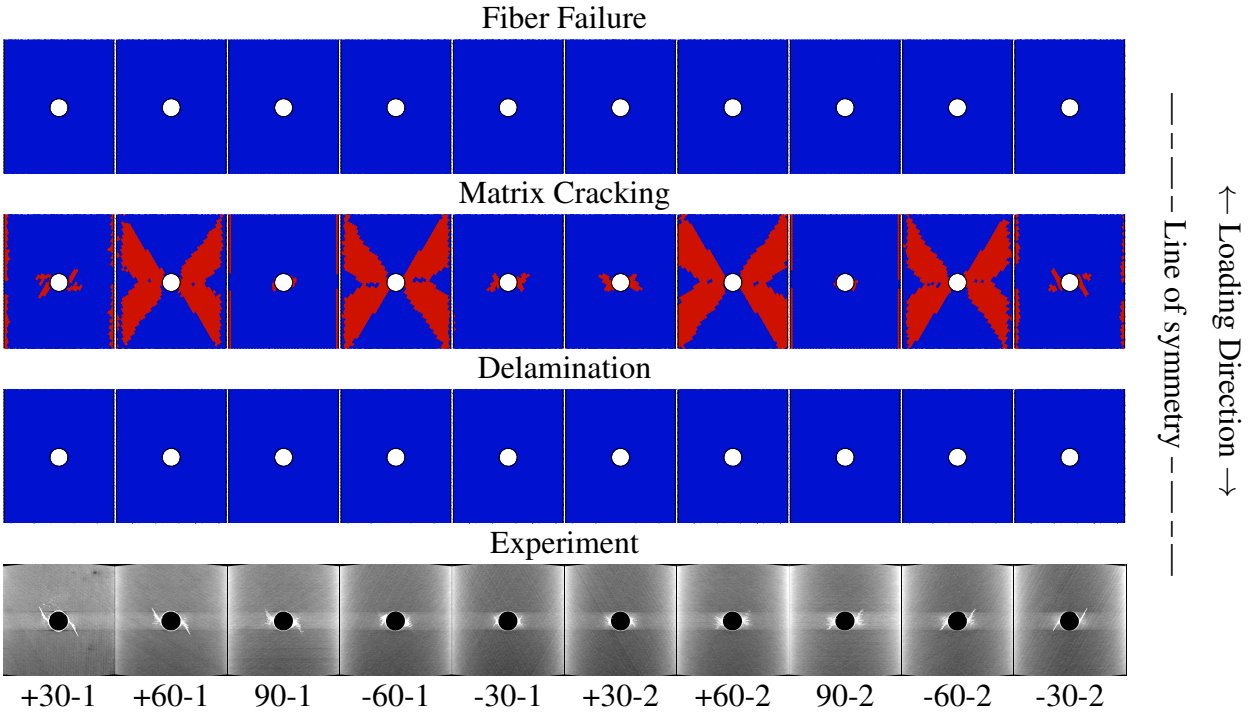

Figure 3.33: Fatigue Damage Contours for $[30,60,90,-60,-30]_{2S}$ Layup after 100K Cycles.

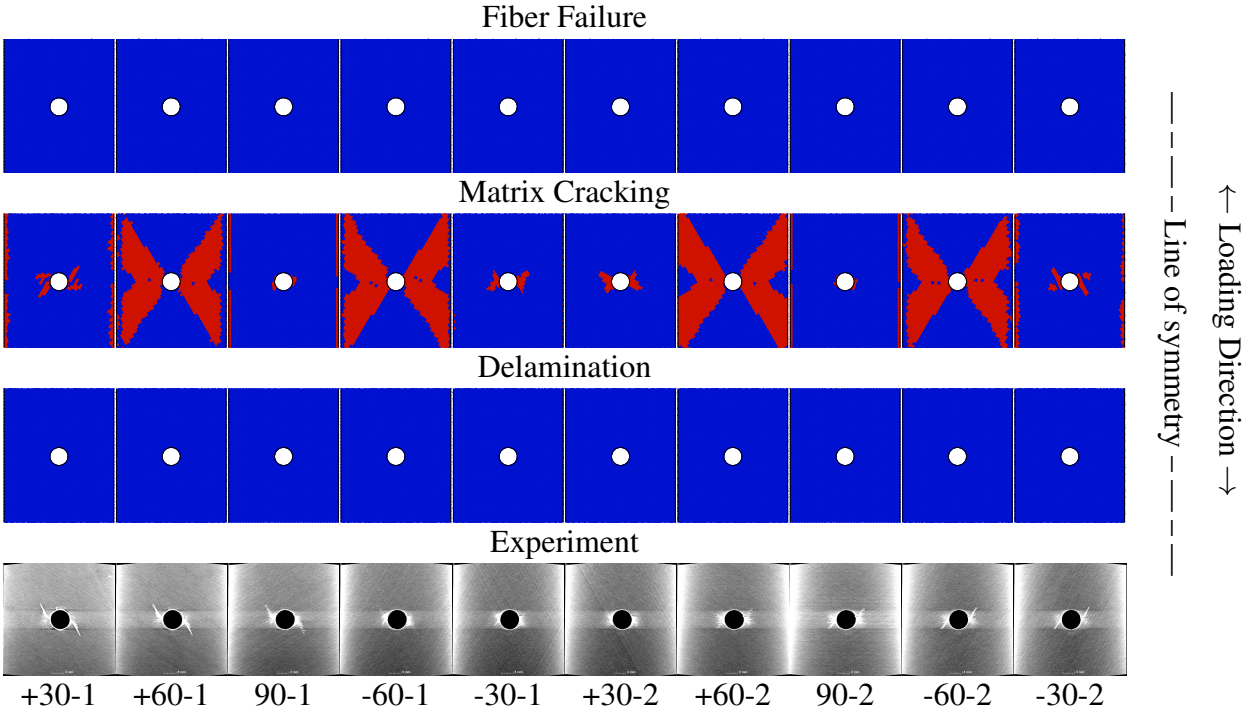

Figure 3.34: Fatigue Damage Contours for $[30,60,90,-60,-30]_{2S}$ Layup after 150K Cycles.

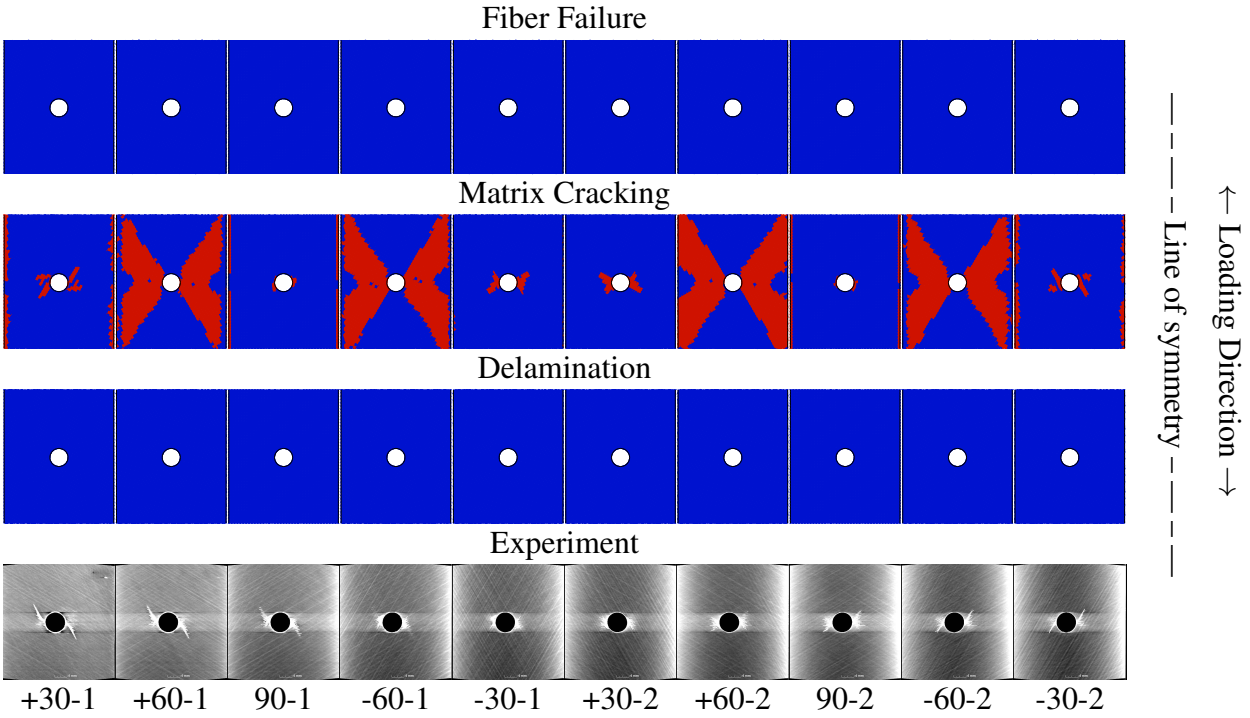

Figure 3.35: Fatigue Damage Contours for $[30,60,90,-60,-30]_{2S}$ Layup after 200K Cycles.

ing transverse to the loading direction away from the hole, as was the cause of early failure in the blind predictions. The premature prediction of such extensive damage is consistent with the rapid stiffness reduction observed in the stiffness vs. life curve of this specimen in Figure 3.25.

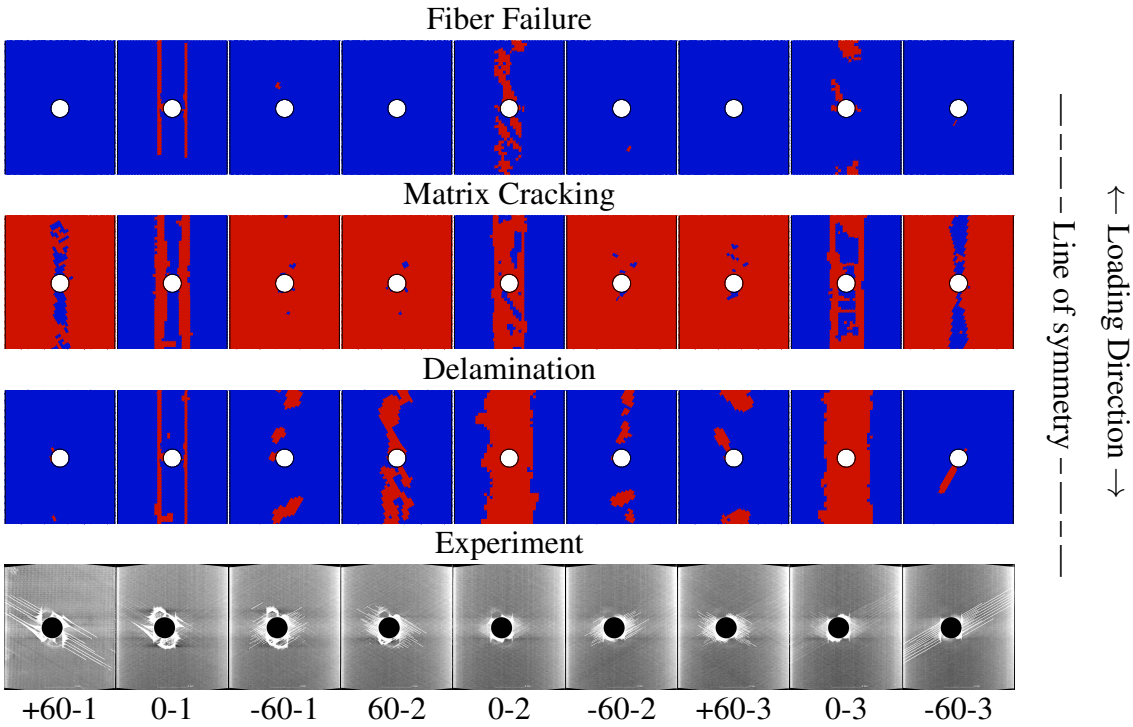

Figure 3.36: Fatigue Damage Contours for $[60,0,-60]_{3S}$ Layup after 50K Cycles.

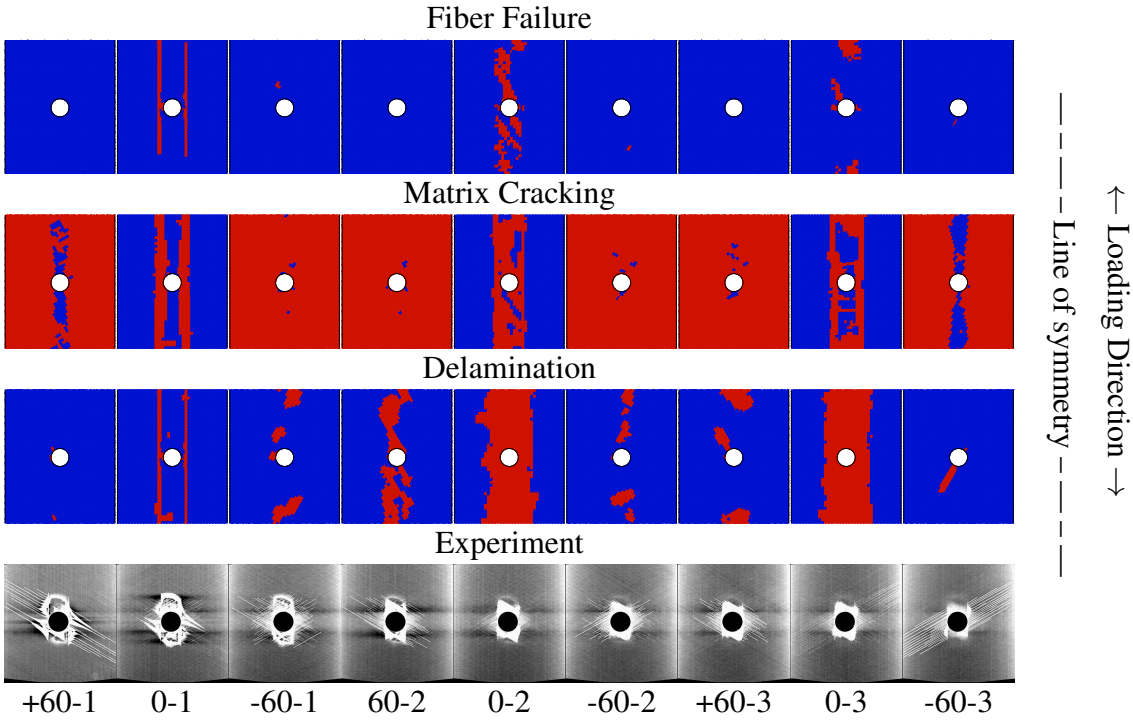

Figure 3.37: Fatigue Damage Contours for $[60,0,-60]_{3S}$ Layup after 100K Cycles.

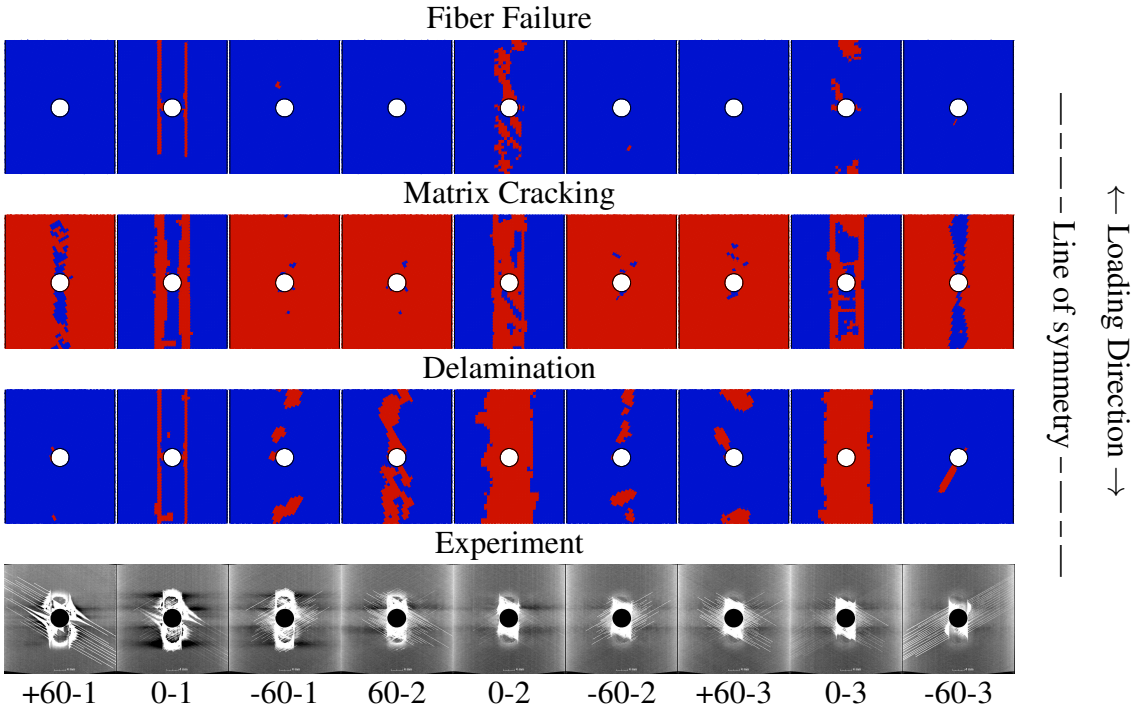

Figure 3.38: Fatigue Damage Contours for $[60,0,-60]_{3S}$ Layup after 150K Cycles.

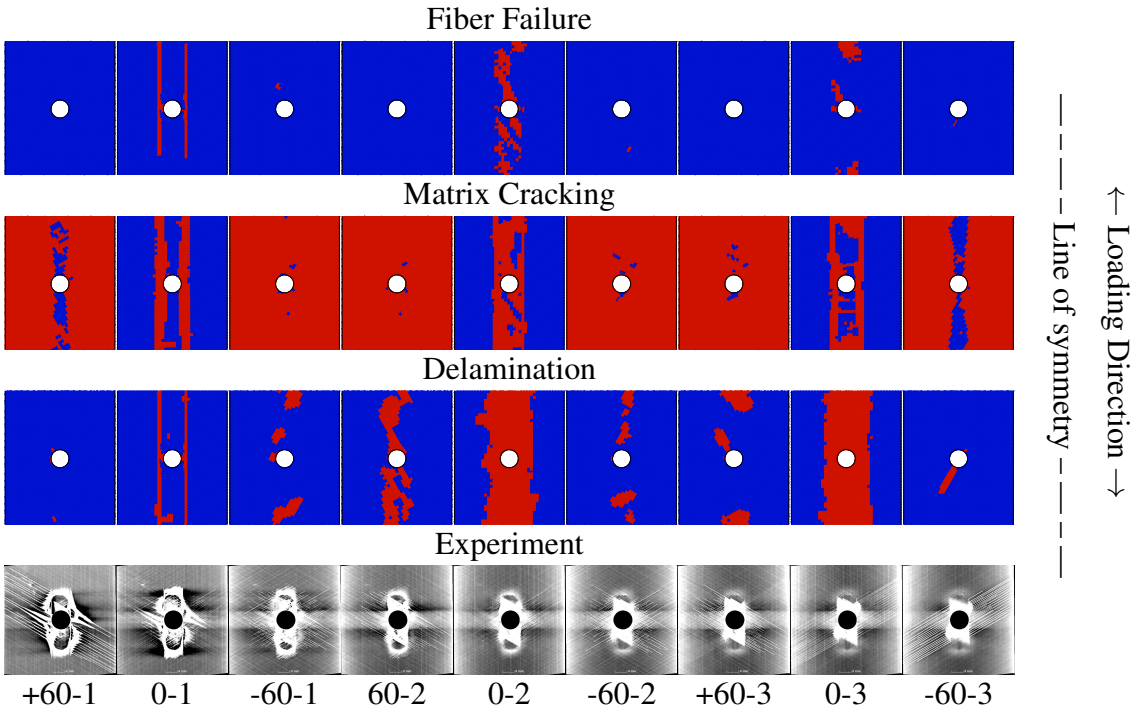

Figure 3.39: Fatigue Damage Contours for $[60,0,-60]_{3S}$ Layup after 200K Cycles.

3.3 Failure Mode Interaction

One lesson learned from the fatigue prediction phases of the DTDP program was the importance of the role of interaction between failure modes in the laminated composite, especially the roles of interlaminar shear strength and delamination development. In the $[60,0,-60]_{3S}$ layup, delamination played a significant role in the predicted behavior of the specimen, whereas the $[0,45,90,-45]_{2S}$ and $[30,60,90,-60,-30]_{2S}$ layups did not display the same sensitivity to delamination development. As more robust predictive models are developed, such as the EHM approach, increased scrutiny can be placed on the specific roles and interactions between inter- and intraply failure modes in the laminate, with high-fidelity simulations to support hypotheses on these effects. In Section 3.3.1, the progressive damage accumulation in $[60,0,-60]_{3S}$ quasi-isotropic laminates under fatigue loading is explored, particularly the formation of delaminations and fiber-splitting. Experimental results are compared with simulations to investigate interaction behavior between failure modes. Discussion of the implications from this investigation is provided in Section 3.3.2, where an explanation for the experimental behavior is proposed, supported by the experimental and simulated behavior.

3.3.1 Experimental-Computational Study Results

Figure 3.40 illustrates the state of damage within a $[60,0,-60]_{3S}$ specimen from the DTDP program through 200K loading cycles as observed using X-ray radiography. The images show damage at all plies through the thickness of the specimen, which is in contrast with the CT images which show a slice of damage through the specimen thickness. The initial state of the specimen is largely defect free with possibly very slight delamination around the hole (Figure 3.40a). The damage region above and below the hole progressively increases as a function of load cycles with snapshots shown for every 50K cycles. The rate of progressive damage accumulation appears to be very stable within this range of cycles. Figure 3.41 further supports the assertion that the nature of damage accumulation is progressive throughout stiffness reduction and acoustic emission hits as a

function of load cycles, shown up to 50K cycles. The damage growth as correlated to the reduction of the stiffness of the composite and the number of AE hits gradually increases with no indication of a change in the damage mode, which would otherwise register a discontinuity or abrupt rate change in the curves. It is noted that Figure 3.41 does not distinguish between propagation of different damage mechanisms that contribute to the property degradation.

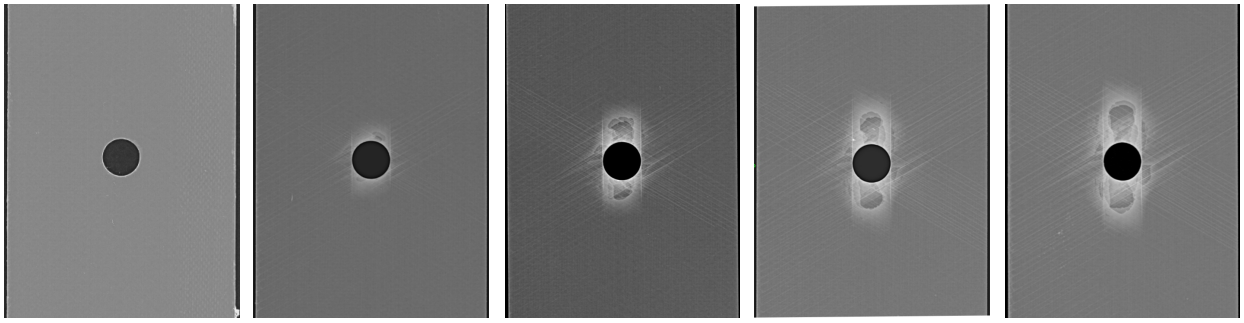

(a) (b) (c) (d) (e)

Figure 3.40: X-ray Radiography Images of the $[60,0,-60]_{3S}$ Specimen: (a) Initial State, After (b) 50K, (c) 100K, (d) 150K, and (e) 200K Cycles.

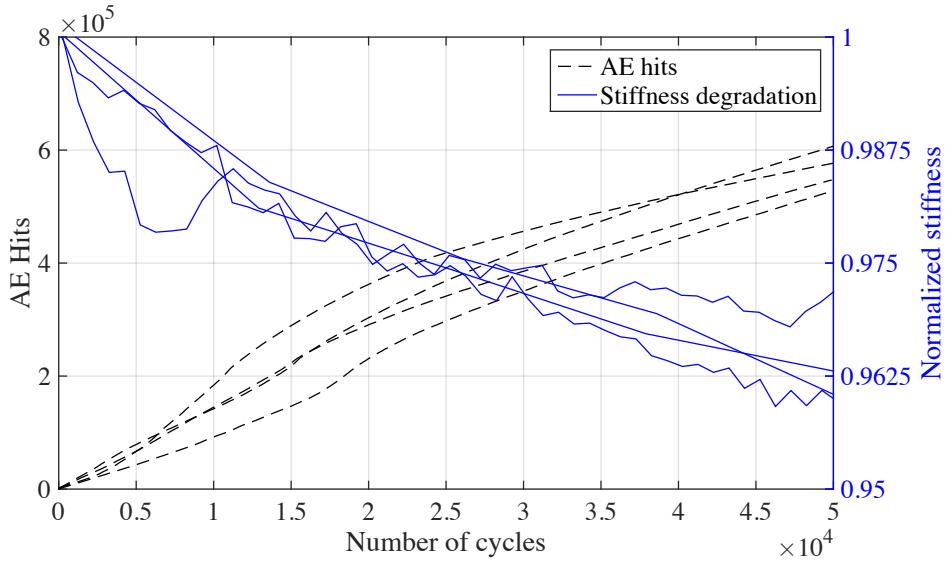

Figure 3.41: Acoustic Emission Hits and Stiffness Degradation as a Function of Load Cycles for Four Identical $[60,0,-60]_{3S}$ Specimens.

Figure 3.42 shows the damage modes within the $[60,0,-60]_{3S}$ specimen that grow under fatigue loading. The close-up image is obtained by 3-D X-ray CT, where the focus is on the 60-0 ply interface. While the CT imaging is able to isolate damage to a small depth through the thickness

of the laminate, damage in the plies behind the interface still bleeds over to the image to a small degree, which accounts for the -60° cracks also visible in the image. The figure clearly shows transverse matrix cracking in the ±60° plies and fiber splitting at the 0° plies. At the 60-0 interface, a large delamination zone exists at the top and bottom of the hole, delimited by the extent of fiber splitting. While the progressive damage accumulation continues throughout the loading history, none of the $[60,0,-60]_{3S}$ specimens failed within the two million cycle observation period, as seen in Figure 3.25.

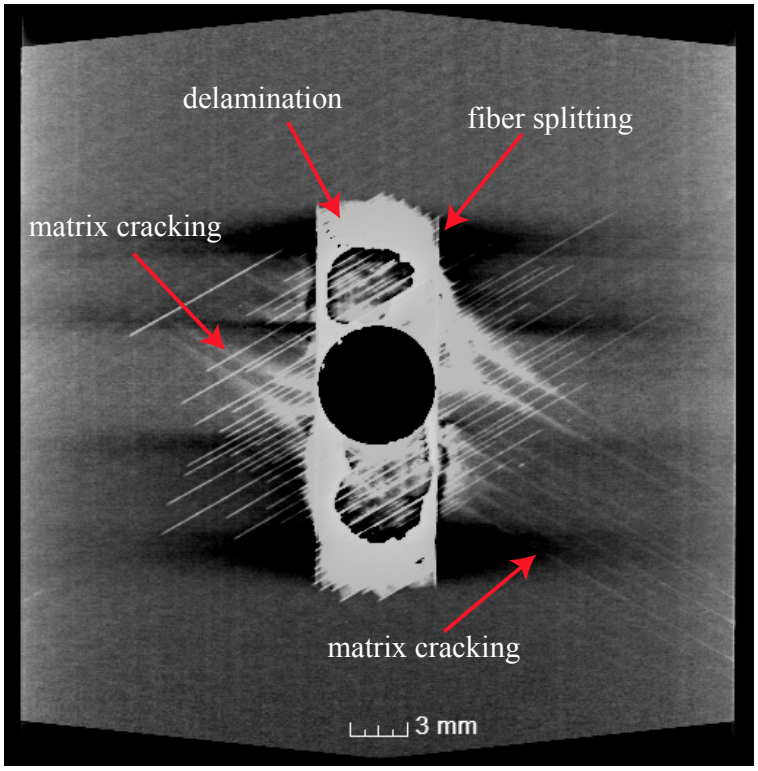

Figure 3.42: X-ray CT Image of the $[60,0,-60]_{3S}$ Specimen After 150K Cycles Illustrating the Damage Modes.

In order to understand the role of interacting sub-critical damage mechanisms on the failure behavior under fatigue loading, the numerical simulations from the blind prediction and recalibrated EHM models were further investigated. The blind prediction case corresponds to a model which includes fiber failure and matrix cracking as possible damage mechanisms whereas the possibility of delamination is deliberately excluded to understand its role on the failure response and overall fatigue life. In the recalibrated model, delamination was allowed to develop as calibrated to end

notch flexure experiments of the IM7/977-3 composite. Figure 3.43 illustrates the stiffness loss from the numerical simulation for the set of material parameters which do not lead to the development of significant delamination and the material parameters such that delamination is present. The same data is represented in both Figure 3.43(a) and (b); (b) is a zoomed in representation to better display the rapid stiffness loss in the simulation where delamination does not develop. In the absence of delamination, the stiffness of the composite specimen degrades very quickly, within approximately 700 cycles, causing failure of the specimen, in a failure mechanism seen in Figure 3.44a. The matrix cracking is accompanied by fracture of the fibers within the zero degree plies that initiate around the hole and propagate outward towards the specimen edges and ultimately cause the specimen failure. The experiments did not exhibit such a substantial fiber failure. Fiber splitting, which was prevalent in all experimental specimens did not form in the numerical simulations where delamination was not present. The damage contours for the simulation where delamination does progress (Figure 3.44b) show significant matrix cracking in the 60° plies, which is consistent with the experimental observation, notwithstanding the pace at which the cracking occurs. The discrepancy between the failure modes observed in the simulations where delamination is not present and the experiments points to the role of delamination in determining the failure characteristics of the composite subjected to fatigue loading.

In contrast to the simulation where the sub-critical damage mode of delamination is omitted, the model where delamination progresses around the hole along the loading direction does not predict a premature fatigue failure. At the early stage of loading, a significant amount of damage occurs, manifested by a drop in the stiffness of the specimen. The damage accumulation rate then reduces and the specimens run out beyond two millions cycles. The damage modes and the accumulation characteristics predicted by the model is similar to the experimental observations, as shown in Figure 3.44b. Fiber splitting and delamination growth are the two dominant damage mechanisms, whereas fiber fracture propagation is not observed. It is noted that the amplitude of loading applied is sufficient to lead to fiber fracture around the hole, even at the first loading cycle, due to the stress concentration from the open hole. Despite the early onset of fiber fracture, fiber fracture does not

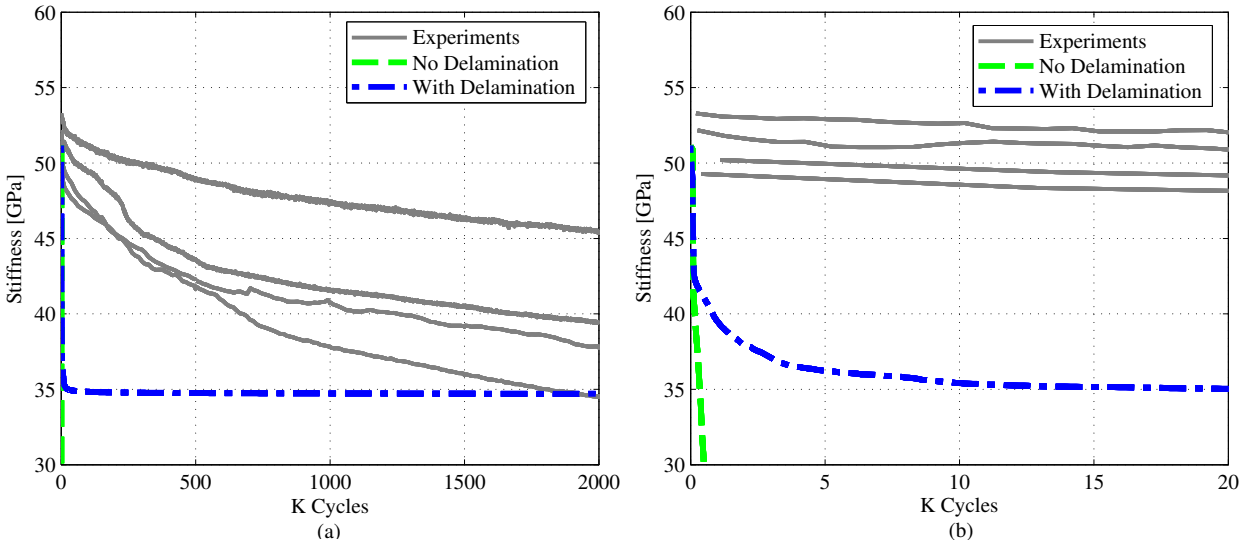

Figure 3.43: Stiffness Loss Curves for $[60,0,-60]_{3S}$ Tension-Tension Fatigue Shown (a) to Run-out, and (b) Blown-up to Display Behavior with No Delamination.

propagate transverse to the loading direction in the case where delamination is allowed to develop. The present damage modes and their propagation characteristics are accurately modeled when both dominant sub-critical modes are included in the model. The rate at which damage propagates with respect to loading is subject to further investigation.

3.3.2 Discussion of Failure Interactions

The combined experimental-computational investigation described above indicates a strong interactive effect of sub-critical damage mechanisms on the fatigue survivability of laminated composites under high amplitude fatigue loading. The investigation indicates that the following cascade of damage events controls the failure in the specimen as illustrated by Figure 3.45a: Under the applied cyclic loading, a shear dominated delamination occurs around the open hole which separates the 0° and 60° plies and permits the propagation of fiber splitting in the zero-degree plies. Fiber splits cause the relaxation of the stress concentration around the hole and redistribute the loading more evenly across the zero degree plies, reducing the stress on the fibers near the hole. The reduction of the stresses on the fibers arrest the propagation of the fiber fracture transverse to the loading

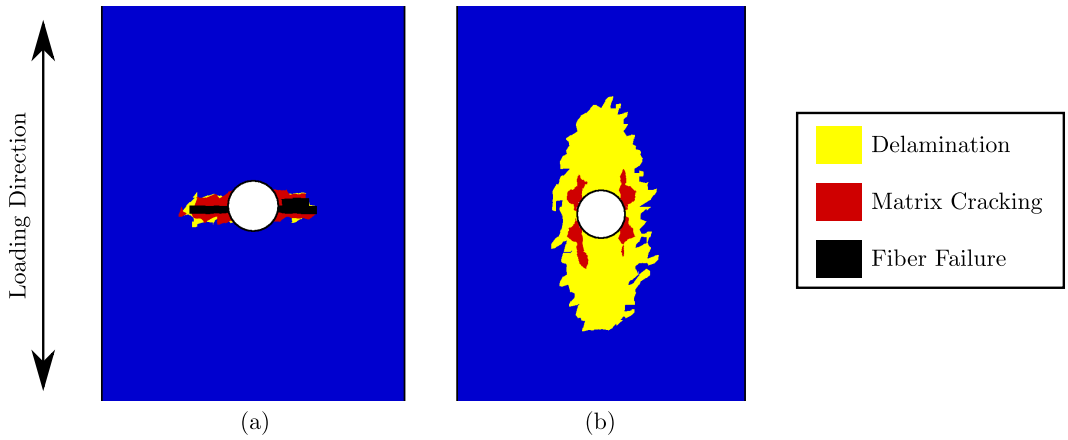

Figure 3.44: Intermediate Damage State for Internal 0° Ply of $[60,0,-60]_{3S}$ Simulation during Fatigue Loading from Simulations (a) Without Delamination and (b) With Delamination

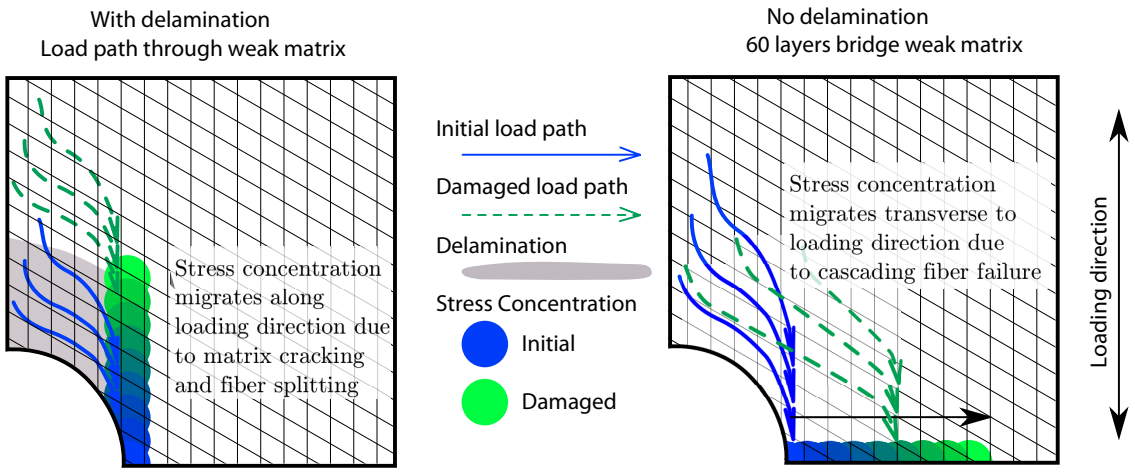

Figure 3.45: Schematic Illustration of the Interaction Between Damage Patterns (a) in the Presence of Delamination Mode; (b) in the Absence of Delamination Mode.

direction. In the absence of delamination, this phenomenon cannot occur. Shear stresses that cause fiber splitting are bridged by the neighboring off-axis plies around the hole and the matrix is left intact. Stress concentration is not relieved and the fiber fracture propagates as a crack through the specimen. This process is schematically illustrated in Figure 3.45b.

This phenomenon is not specific to the $[60,0,-60]_{3S}$ laminate. The growth of fiber splitting can also be seen to a much smaller degree in the $[0,45,90,-45]_{2S}$ laminate in Figure 3.31. Fiber splitting plays a much less significant role in this laminate, which is possibly due to the applied stress for the $[0,45,90,-45]_{2S}$ tension-tension fatigue experiment in this exercise being only 50% of the static

ultimate strength. It is clear that the interaction between delamination, fiber splitting, and fiber failure occurs in a different manner for different layup configurations and applied stress levels. Spearing et al. [95] also observed the phenomenon of fiber splitting induced relaxation mechanism in quasi-isotropic samples. In their case, the zero-degree surface plies quickly formed fiber splits under fatigue loading. When the zero degree plies are on the surface, the delamination mechanism is no longer needed as the plies are already kinematically unrestricted from splitting.

Further evidence of the stress relaxation effect was observed in the residual strength after fatigue of laminated composite specimens which were performed at the AFRL. Figure 3.46 shows the residual strength after fatigue of quasi-isotropic ($[+45,0,-45,90]_{2S}$) specimens as a function of the applied fatigue load amplitude. The residual strengths were measured after subjecting each cycle to 200K constant amplitude tension fatigue with an R-ratio of 0.1. For this layup, an increase in the strength from the virgin (i.e., not previously subjected to fatigue) strength is observed when the specimens are subjected to fatigue cycles. The corresponding damage profiles induced by prior fatigue loading is shown in Figure 3.47. This figure further demonstrates that the sub-critical damage mechanisms of delamination induced fiber splitting relieves the stress concentration and a consequent increase of residual strength. While this phenomenon has been previously observed, the connection of its occurrence to the interacting damage modes were not made.

The role of interacting damage mechanisms and their accumulation on the fatigue survivability of laminated composites is particularly important at high amplitude fatigue loading, where significant early fiber fracture is likely to occur. At lower amplitude loading, the fibers are able to carry the loads without the need to redistribute the load. The sub-critical damage mechanisms therefore may not have as large an impact on specimen survivability.

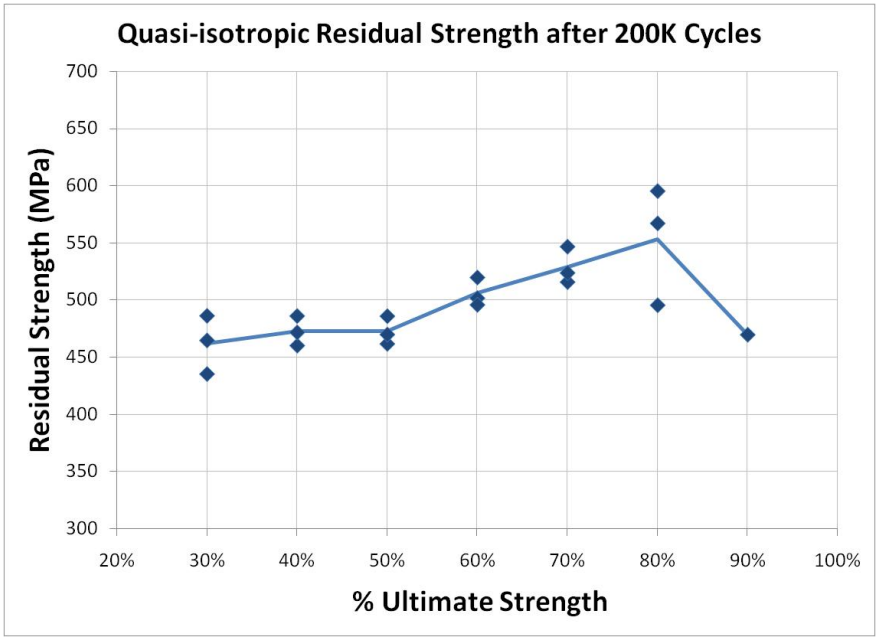

Figure 3.46: Residual Strength After 200K Fatigue Cycles of $[+45,0,-45,90]_{2S}$ Specimens as a Function of Fatigue Load Amplitude.

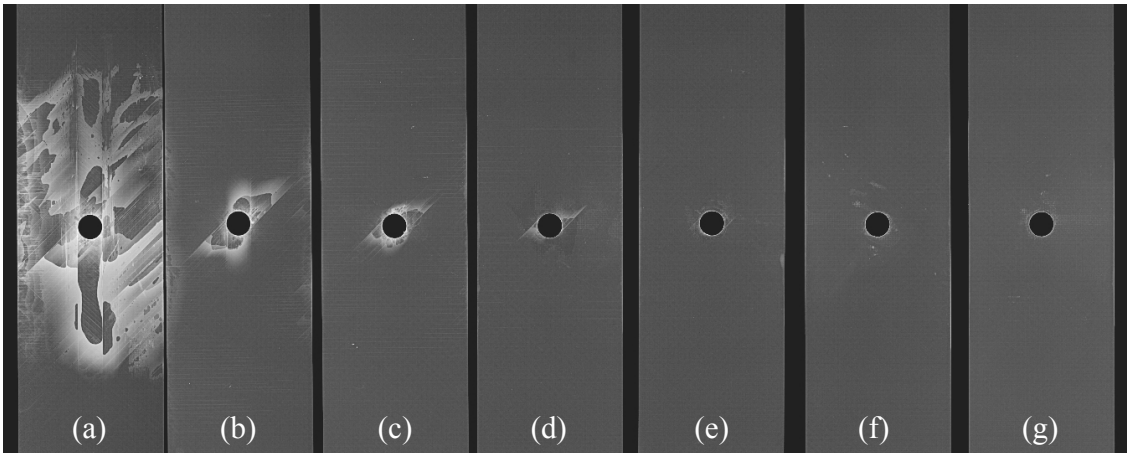

Figure 3.47: X-ray Images of the $[+45,0,-45,90]_{2S}$ Specimens Subjected to 200K cycles of Loading with Maximum Amplitude of (a) 90%; (b) 80%; (c) 70%; (d) 60%; (e) 50%; (f) 40%; and (a) 30% of Mean Static Ultimate Strength.

Chapter 4

COMPOSITE UNCERTAINTY AND VARIABILITY

Statistical variability in composite materials arises from a wide range of sources over the multiple scale of interest present in the material system. These sources of uncertainty, both epistemic and aleatory are addressed in Section 4.1. Because uncertainty is present at multiple disparate scales, the problem of quantifying uncertainty from each of these sources is a significant challenge. Furthermore, many times the sources of uncertainty cannot be directly measured, and the information that is available comes from larger scales of interest than scale of the quantities being considered. For instance, in the following investigations, the quantities of interest are the random underlying constituent material parameter distributions for the fiber and matrix which govern the microscale damage accumulation behavior, whereas calibration data is available from the composite lamina scale. In this work, a new probabilistic multiscale methodology is presented to link the material property variability at the scale of the microstructure to the laminate scale and predict the uncertainty associated with the composite strength. The proposed methodology relies on EHM to bridge the micro- and the macroscales. Bayesian statistical analysis forms the foundation of the uncertainty quantification framework for the calibration of random parameters which define the multiscale EHM model, as described in Section 4.2. Markov chain Monte Carlo (MCMC) sampling, found in Section 4.3, is utilized to perform the computation required to generate the random material distributions. Section 4.4 describes the Gaussian process (GP) modeling which is employed to approximate the failure response of the multiscale simulations in the rapid sampling MCMC process as a surrogate model for the EHM model. This work provides a new method to propagate uncertainty from the constituent materials of a heterogeneous composite to the macroscopic scale in the context of computational homogenization, employs the Bayesian statistical method to stochastic constituent parameter calibration in composites, and characterizes the influence of microscale parameter variability on the failure response of composite laminates. Numerical

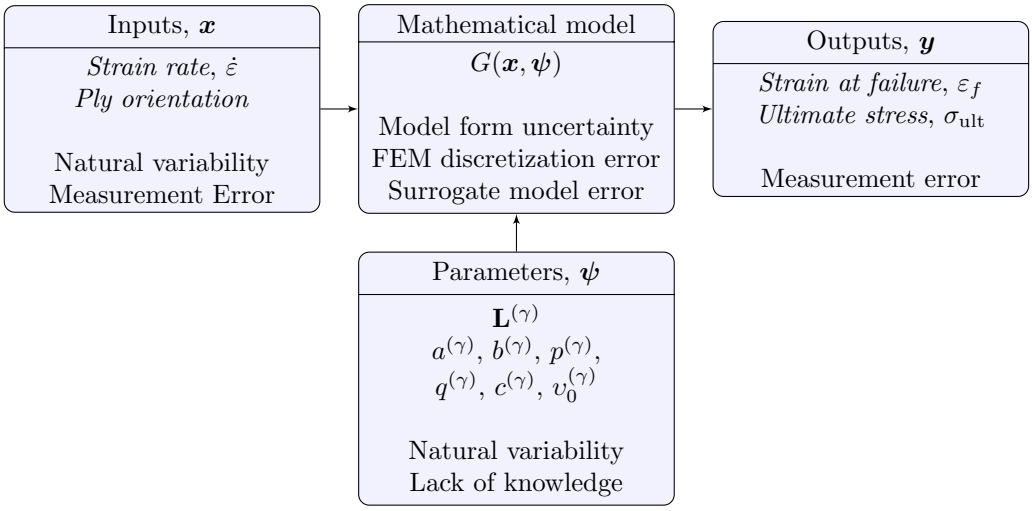

Figure 4.1: Sources of Uncertainty in Model Prediction.

investigations applying this approach are found in Chapter 5.

4.1 Sources of Uncertainty

Consider the case of a monotonically loaded composite specimen. A suite of experiments have been performed on this specimen and the intent is to create a mathematical representation of the physical system to predict the results of the experiments. This model is shown in Figure 4.1 including the inputs, outputs, mathematical model form, and model parameters, as well as the types of uncertainty characteristic of each component. The goal of this model is to predict the ultimate stress, σ_{ult}, and strain at failure, ε_f, for the composite material. These are the outputs, $\boldsymbol{y}$, of the model $G(\boldsymbol{x}, \boldsymbol{\psi})$, for the inputs, $\boldsymbol{x}$, subject to the model parameters, $\boldsymbol{\psi}$. Reported output values from experiments are subject to measurement error from the instruments used to collect this data and are also subject to error in the experimental setup, collectively considered to be measurement error. The inputs for both the underlying physical phenomenon and the prediction model, considering rate-dependent failure behavior, are the strain rate and orientation of the composite ply, as these values are directly controlled in the experiments. These inputs are also subject to natural variability, i.e., the applied strain rate fluctuates over time, and measurement error. The mathematical employed to represent the physical phenomenon of interest is subject to uncertainty in the

form of the model used and its underlying assumptions and numerical aspects, including in the case of the EHM model FEM discretization error, as well as error in the surrogate model when the GP model approximation is employed. The parameters for the mathematical model include the elastic properties, contained in the stiffness matrix, $\mathbf{L}^{(\gamma)}$, and the damage evolution parameters, $a^{(\gamma)}$, $b^{(\gamma)}$, $p^{(\gamma)}$, $q^{(\gamma)}$, $c^{(\gamma)}$, and $\upsilon_{0(\alpha)}$ for each phase, which are subject to natural variability and lack of knowledge, such as when sufficient data is not available to accurately define the parameters.

The underlying physical response of the composite material is subject to random natural variability. This is present in the variability of the elastic properties and the damage evolution parameters for the each phase of the composite. Epistemic uncertainty is, however, also present in these parameters from incomplete information on the distribution of the parameters. Of primary concern in this study are the parameters that govern the rate-dependency of the stress-strain response, ultimate strength and ductility modeled by the $a^{(\gamma)}$, $b^{(\gamma)}$, $p^{(\gamma)}$, and $q^{(\gamma)}$ parameters of the rate-dependent damage evolution law from Section 2.3.2. It is difficult to analytically arrive at the distributions of these parameters directly from experimental data because the observable response of the material is non-linearly related to these parameters. What is required is an indirect calibration approach to determine the range of possible combinations of material parameters. Further, multiple parameters need to be calibrated simultaneously, in order to capture the non-linear relationships between the parameters. This is accomplished through the use of a Bayesian calibration method, discussed below. Measurement error is present in the model inputs - strain rate and loading orientation - and outputs - macroscopic ultimate stress and strain at failure, due to imprecision in the techniques used to record these values. Slight perturbations in the experimental inputs cause the simulation model to vary from the natural behavior that is actually occurring, propagating error to the predicted outputs. Input measurement error is assumed to be small for the experiments considered in this study and is not explicitly modeled. The uncertainty from output measurement error is commonly represented as a Gaussian random variable with zero mean and known or estimated standard deviation.

Solution approximation error exists in the model from homogenization, finite element dis-

cretization, and surrogate modeling [59]. As an example of homogenization error, the composite fiber ratio is given as an average quantity for the entire composite. However, in some areas of the material, the local fiber ratio can vary significantly from the mean. In this analysis, the stresses and strains and the fiber ratio for the composite are assumed to be uniform at the structural scale, varying only at the RVE microscale (i.e. uniform macroscopic response). The uncertainty from these homogenization assumptions could be further quantified by using RVEs of various fiber ratios, constructing macroscopic models randomly composed of these RVEs, and analyzing the resulting macrostructures for the variability in the response. There is additional model uncertainty from discretization error in the finite element model, which can be reduced by refining the mesh in the RVE or the macroscale mesh. These additional finite element analyses represent significant computational expense and are not implemented in this investigation. Surrogate models that replace finite element models also contribute to approximation error. The uncertainty from the surrogate model approximation is available from the GP prediction variance and a cross-validation approach, as explained later.

A major source of epistemic uncertainty in the model comes from the model form itself. The true value of the quantity of interest, y_{true}, (e.g. σ_{ult} or ε_f) accounting for various sources of uncertainty is represented as:

$$y_{true} \quad = \quad \hat{y}(\boldsymbol{x}, \boldsymbol{\psi}) + \delta(\boldsymbol{x}) + \epsilon_m \tag{4.1}$$

where $\hat{y}(\boldsymbol{x}, \boldsymbol{\psi})$ is the predicted output from the model, ϵ_m the measurement error, and $\delta(\boldsymbol{x})$ is a model discrepancy term introduced by Kennedy and O'Hagan [51]. The $\delta(\boldsymbol{x})$ term is used to reflect the inherent discrepancy in the model prediction with respect to the experimental observations. This discrepancy includes the contributions from surrogate model error, model form uncertainty, homogenization error, and finite element discretization error. (Alternatively, one could also separately quantify the solution approximation errors and include them in Eq. 4.1, in order to quantify the model form error). Note that $\delta(\boldsymbol{x})$ depends on the input, $\boldsymbol{x}$, i.e., the model discrepancy varies depending on the rate of loading applied. This discrepancy terms accounts for

additional effects which are not explicitly incorporated in the mathematical model. In the context of the rate-dependent model, this could be the presence of inertial effects or higher-order viscous effects which are present only at the higher loading rates.

4.2 Bayesian Calibration

The Bayesian statistical approach is employed to calibrate the probabilistic distributions of the constituent failure parameters and quantify their uncertainty. A critical observation is that the calibration process itself is multiscale. Calibration data is often measured and meaningful at the laminate level, whereas the parameters to be calibrated are characterized at the scale of the RVE.

Consider an arbitrary quantity of interest, ϕ_{lam}, (e.g., ultimate stress) that is measurable at the scale of the laminate. For a given set of input conditions, $\boldsymbol{x}$, assume the macroscale quantity can be described as a function, G, of the microscale material parameters, $\boldsymbol{\psi}$:

$$\phi_{lam} = G(\boldsymbol{\psi}) \quad \boldsymbol{\psi} \in \mathbf{S} \subset \mathbb{R}^{n_p} \tag{4.2}$$

where n_p is the number of constituent parameters, and $\mathbf{S}$ the range of parameter values defined by physical constraints. In this work, $G(\boldsymbol{\psi})$ represents the response surface defined by the multiscale mechanical model. Under the deterministic approach, ϕ_{lam} is a scalar value and the goal of the calibration process is to find a single vector of constituent parameters which produce the desired output. This is analogous to solving the inverse problem, $\boldsymbol{\psi} = G^{-1}(\phi_{lam})$. For multiscale analyses with non-linear material models, however, G is not easily invertible, and requires a rigorous optimization strategy to identify $\boldsymbol{\psi}$.

In a probabilistic setting, the desire is not only to find the parameters resulting in a single value of ϕ_{lam}, but the distribution of parameters, $f_{\boldsymbol{\psi}}$, which lead to the desired random distribution in the quantity of interest, $f_{\phi_{lam}}$. The calibrated parameter distributions must not only reflect the range of values in $f_{\phi_{lam}}$, but also accurately model the stochastic characteristics of the $f_{\phi_{lam}}$. The probabilistic constituent material parameter calibration strategy employed herein is rooted in Bayes' Theorem, which is based on the principles of conditional probability. Consider two distinct

random events A and B. The probability of simultaneously observing A and B, denoted as $P(AB)$, is expressed using the conditional probabilities as:

$$P(AB) = P(A|B)P(B) = P(B|A)P(A) \tag{4.3}$$

where, $0 \leq P(A) \leq 1$ denotes the probability of observing event A, and $P(A|B)$ the conditional probability of observing A given that B has been observed. Rearranging the equality yields Bayes' Theorem:

$$P(A|B) = \frac{P(B|A)P(A)}{P(B)}; \quad P(B) > 0 \tag{4.4}$$

Considering the collectively exhaustive and mutually exclusive events A_i ($i \in \mathcal{I} := \{1, 2 \ldots, m\}$) where $\sum_i P(A_i) = 1$ and $P(A_j) \geq 0 \; \forall \; j \in \mathcal{I}$, and using the theorem of total probability, Bayes' Theorem is expressed in terms of discrete events as:

$$P(A_i|B) = \frac{P(B|A_i)P(A_i)}{\sum_j P(B|A_j)P(A_j)} \tag{4.5}$$

Equation 4.5 is interpreted as the probability update procedure. Let B be an event, such as an observation from an experiment, that has some dependence on A_i, such that $P(B|A_i)$ is well defined, then $P(A_i)$ and $P(A_i|B)$ are interpreted as the probability distributions of A_i prior to and posterior to the occurrence of event B, respectively. In the context of the material parameter updating, A_i are considered to be continuous rather than discrete events. Renaming the variables and considering continuous events, the parameter update function is expressed as:

$$f(\boldsymbol{\psi}|y_{obs}) = \frac{f(y_{obs}|\boldsymbol{\psi})f(\boldsymbol{\psi})}{\int_{\mathbf{S}} f(y_{obs}|\boldsymbol{\chi})f(\boldsymbol{\chi})d\boldsymbol{\chi}} \tag{4.6}$$

in which y_{obs} denotes observed experimental data, $f(\boldsymbol{\psi}|y_{obs})$ the posterior probability of the parameters $\boldsymbol{\psi}$ given the observed experimental data, $f(y_{obs}|\boldsymbol{\psi})$ the probability of observing y_{obs} given parameters $\boldsymbol{\psi}$, and $f(\boldsymbol{\psi})$ the prior probability of $\boldsymbol{\psi}$. The conditional probability, $f(y_{obs}|\boldsymbol{\psi})$, is the "likelihood" of parameters $\boldsymbol{\psi}$ producing y_{obs}, and is denoted as $\mathcal{L}(\boldsymbol{\psi})$. For simplicity, prior and posterior probabilities of $\boldsymbol{\psi}$ are denoted as $f'(\boldsymbol{\psi})$ and $f''(\boldsymbol{\psi})$, respectively. The denominator of the right hand side in Eq. (4.6) is a normalizing constant such that the area under the curve of $f''(\boldsymbol{\psi})$

is equal to 1. As will be seen below, the actual value of $f''(\boldsymbol{\psi})$ is not important in the Bayesian updating procedure, only the ratio between the probability of different parameter points, and therefore the expensive integration required to evaluate the denominator does not need to be performed. The parameter update is then expressed in the alternative form:

$$f''(\boldsymbol{\psi}) \propto \mathcal{L}(\boldsymbol{\psi}) f'(\boldsymbol{\psi}) = \bar{f}(\boldsymbol{\psi}) \tag{4.7}$$

where $\bar{f}(\boldsymbol{\psi})$ is the unnormalized kernel of the posterior probability distribution for $\boldsymbol{\psi}$, i.e. the area under the curve for $\bar{f}(\boldsymbol{\psi})$ over the set of all possible parameter values $\mathbf{S}$ is not normalized to unity, as with a typical probability density function.

When the observations come from a suite of similar or identical experiments, the observation, y_{obs}, is a distribution characterized by the probability density function, f_{obs}. The observation distribution can be expressed using either a parameterized distribution (i.e normal, log-normal, Weibull, etc.) or in a non-parametric form, such as the Kernel Spectral (KS) function [80, 75]. In the following investigations, a non-parametric probability density function is employed in reporting calibrated values and observation results. The Bayesian calibration methods employed herein are applicable to both parametric and non-parametric distributions. In this study, the desire was to consider the information from experiments with as little bias as possible. In using a parametric distribution, the distribution parameters are enforced on the statistics of the information, which does effect the results. On the other hand, the use of non-parametric distribution may introduce fluctuations and features in the predicted distributions which are artifacts of small data sets and model errors. Ultimately, non-parametric KS distributions were employed to further demonstrate the flexibility of the Bayesian calibration approach for a wide range of statistical distributions.

Consider a set of experimental observations, $\boldsymbol{y}_{obs} = \{y^1_{obs}, y^2_{obs}, \ldots, y^p_{obs}\}$, the probability density using the KS approximation is expressed as:

$$f_{obs}(y) \simeq \frac{1}{ph} \sum_{i=1}^{p} K\left(\frac{y - y^i_{obs}}{h}\right) \tag{4.8}$$

where p is the total number of observations, h the kernel bandwidth, and K the symmetric kernel.

In the form of the standard normal density function,

$$K(x) = \frac{1}{\sqrt{2\pi}} \exp\left(-\frac{1}{2}x^2\right). \tag{4.9}$$

From Reference [90], the optimal bandwidth for a standard normal kernel is estimated as:

$$h = \left(\frac{4\sigma_{obs}^5}{3p}\right)^{\frac{1}{5}} \tag{4.10}$$

where σ_{obs} is the standard deviation of the experimental observations.

When the experimental observation is a scalar (e.g., strength), using KS density estimation and recalling that the model prediction of the observed quantity, ϕ_{lam}, is expressed in terms of the constituent parameters as: $\phi_{lam} = G(\boldsymbol{\psi})$, the likelihood function is defined as:

$$\mathcal{L}(\boldsymbol{\psi}) = \frac{1}{ph}\frac{1}{\sqrt{2\pi}}\sum_{i=1}^{p} \exp\left(-\frac{1}{2}\left[\frac{G(\boldsymbol{\psi}) - y_{obs}^i}{h}\right]^2\right). \tag{4.11}$$

4.3 Markov Chain Monte Carlo Simulation

Equation 4.7 provides the mathematical form for computing the posterior probability of the model parameters for G, but direct computation of this value over the set of all possible material parameters $\mathbf{S}$, quickly becomes a computational burden, especially when multiple model parameters are present. An efficient sampling method is required to accurately and effectively evaluate $f''(\boldsymbol{\psi})$. MCMC sampling is used to produce a "chain," or set, of model parameter values from Monte Carlo simulation whose probability density estimates the posterior distribution of those parameters. In general, a Markov chain is a memoryless random process where a given state depends on the previous state only. In the context of parameter updating, the states in the Markov chain are the parameter values, and each new state is determined by comparing the likelihood estimate of the previous state and a trial state. The chain is started from set of parameter values, $\boldsymbol{\psi}_0$, whose likelihood is greater than 0. Given a parameter state in the chain, $\boldsymbol{\psi}_k$, a trial parameter state, $\boldsymbol{\psi}^*$, is sampled by taking a random walk from $\boldsymbol{\psi}_k$. Considering the prior probability times likelihood of

the two parameter sets:

$$\bar{f}(\boldsymbol{\psi}_k) = \mathcal{L}(\boldsymbol{\psi}_k) f'(\boldsymbol{\psi}_k) \qquad \text{and} \qquad \bar{f}(\boldsymbol{\psi}^*) = \mathcal{L}(\boldsymbol{\psi}^*) f'(\boldsymbol{\psi}^*). \tag{4.12}$$

The trial state, $\boldsymbol{\psi}^*$, is accepted with probability of

$$a = \min(1, \frac{\bar{f}(\boldsymbol{\psi}^*)}{\bar{f}(\boldsymbol{\psi}_k)}) \tag{4.13}$$

This implies that if the trial parameter state is more likely to yield the observed values than the current parameter state it is automatically accepted, and if the trial state is less likely, it will be accepted randomly with a probability diminishing with its comparative likelihood with the current state. As the acceptance criterion is based on the ratio of likelihoods, the constant denominator from Equation 4.6 is canceled out, and is not necessary to evaluate. If the trial state, $\boldsymbol{\psi}^*$ is rejected, the current state, $\boldsymbol{\psi}_k$, is repeated in the chain and a new $\boldsymbol{\psi}^*$ is sampled and tested.

The completion criteria for MCMC is the convergence of the chain. Chain convergence is achieved when additional samples do not affect the generated distributions. The posterior density distributions of each of the parameters can then be evaluated by fitting the chain to a parametric distribution, or employing KS density for a non-parametric PDF. Additionally, the covariance of the parameters in the chain is computed as:

$$\sigma_{cov}(\boldsymbol{\psi}^i, \boldsymbol{\psi}^j) = \frac{1}{N_{mcmc} - 1} \sum_{k=1}^{N_{mcmc}} (\boldsymbol{\psi}_k^i - \bar{\boldsymbol{\psi}}^i)(\boldsymbol{\psi}_k^j - \bar{\boldsymbol{\psi}}^j) \tag{4.14}$$

where N_{mcmc} is the number of MCMC steps and $\bar{\boldsymbol{\psi}}^i$ is the sample mean of $\boldsymbol{\psi}^i$, which is the chain of parameters generated for the i^{th} component of $\boldsymbol{\psi}$. The covariance is important in sampling correlated random parameters from the generated distributions.

4.4 Surrogate Models using Gaussian Processes

MCMC requires hundreds of thousands of samples evaluated in serial to generate converged parameter chains. The time required to perform this procedure using the nonlinear multiscale simulations is prohibitively large. To achieve computational efficiency, a surrogate model is trained

to approximate the response surface which is otherwise generated by full multiscale simulations. GP modeling is employed because of its ability to capture nonlinear surfaces and quantify the uncertainty in the approximation of the response surface [45, 77, 87].

The GP model is a variant of a radial basis function built on Gaussian kernels. The GP model is trained by a series of simulations performed using the multiscale model. Consider a set of n_t input training parameter sets, $\boldsymbol{\psi}_t = \{\boldsymbol{\psi}_{t_1}, \ldots, \boldsymbol{\psi}_{t_{nt}}\}$ such that $\boldsymbol{\psi}_{t_i} \in \mathbf{S}$. In this work, Latin hypercube sampling is employed to obtain parameter sets spread within $\mathbf{S}$. The multiscale model is exercised to compute the corresponding set of output values, $\boldsymbol{y}_t$, from parameters $\boldsymbol{\psi}_t$. For a given input prediction point, $\boldsymbol{\psi}_p$, the output of the GP, y_p, is computed as a Gaussian (Normal) distribution conditioned upon the prediction point, training points, training point outputs, and the hyperparameters of the GP, $\boldsymbol{\Psi}$:

$$p(y_p|\boldsymbol{\psi}_p, \boldsymbol{\psi}_t, \boldsymbol{y}_t; \boldsymbol{\Psi}) \sim N(m, S) \tag{4.15}$$

where m and S are the prediction mean and variance and N denotes a Gaussian distribution.

The covariance, k_{ij}, between two points, $\boldsymbol{\psi}_i$ and $\boldsymbol{\psi}_j$, in the input space is defined as

$$k_{ij} = k(\boldsymbol{\psi}_i, \boldsymbol{\psi}_j) = \theta_1 \exp\left\{ -\frac{1}{2} \sum_{d=1}^{n_p} \frac{(\psi_{i_d} - \psi_{j_d})^2}{\lambda_d^2} \right\} \tag{4.16}$$

in which θ_1 is a scaling factor and λ_d the length scale parameter in the d^{th} input dimension. θ_1 and λ_d comprise the hyperparameters of the GP model. When λ_d is small, variation in the output response is more sensitive to slight perturbations of the input. When λ_d is large, the output response is less sensitive to changes in the input. A covariance matrix is defined for any two sets of parameters, $\boldsymbol{\psi}_a = \{\boldsymbol{\psi}_{a_1}, \ldots, \boldsymbol{\psi}_{a_{na}}\}$ and $\boldsymbol{\psi}_b = \{\boldsymbol{\psi}_{b_1}, \ldots, \boldsymbol{\psi}_{b_{nb}}\}$ such that

$$\mathbf{K}_{AB_{ij}} = k(\boldsymbol{\psi}_{a_i}, \boldsymbol{\psi}_{b_i}). \tag{4.17}$$

The covariance matrices of interest in the GP model are those between the set of training input values, denoted by T and the set of prediction input values, denoted by P.

The optimal length scale parameters are inferred in the training of the GP model from the given

data by maximizing the log marginal likelihood [45, 77]:

$$\log P(\mathbf{y}_T \mid \mathbf{x}_T; \theta) = -\frac{1}{2}\mathbf{y}_T{}^{\mathsf{T}}(\mathbf{K}_{TT} + \sigma_n^2\mathbf{I})^{-1}\mathbf{y}_T - \frac{1}{2}\log \mid \mathbf{K}_{TT} + \sigma_n^2\mathbf{I} \mid + \frac{n_p}{2}\log(2\pi) \quad (4.18)$$

where σ_n^2 is the noise variance of the training points and I indicates the identity matrix whose size matches $\mathbf{K}_{TT}$.

The prediction mean, m, and variance, S, from the trained GP model are defined as:

$$m = \mathbf{K}_{PT}(\mathbf{K}_{TT} + \sigma_n^2 I)^{-1}\boldsymbol{y}_t \quad (4.19)$$

$$S = \mathbf{K}_{PP} - \mathbf{K}_{PT}(\mathbf{K}_{TT} + \sigma_n^2 I)^{-1}\mathbf{K}_{TP} \quad (4.20)$$

Where $\mathbf{K_{PP}}$, $\mathbf{K_{PT}}$, and $\mathbf{K_{TP}}$ are computed from the set of prediction inputs. For GP model predictions trained from computer models, σ_n^2 is taken as 0, as the computer prediction is taken to be a noiseless process (i.e. the computer output is taken to be always the same for the same input).

Surrogate model error is a function of the distance between the prediction point and the nearby training points. Model prediction error is taken to be lesser for predictions made closer to the values used to train the response surface of the GP model, while there are high errors associated with predicting outputs for inputs that are not near the training points. The surrogate model error can be estimated in the GP model using a jackknifing or "leave-one-out" cross-validation approach [45]. For each of the n_t training points, a GP model is constructed leaving out the n_t^{th} point. The prediction mean and variance at this point is then determined for each of the n_t points in this manner as a Gaussian $\sim N(m, S)$. Finally, the surrogate model prediction error, ϵ_{su}, can be estimated also as a Gaussian distribution with mean, μ_{su}, and variance, σ_{su}^2:

$$\mu_{su} = \sum_{i=1}^{n_t} m_i \quad (4.21)$$

$$\sigma_{su}^2 = \sum_{i=1}^{n_t} S_i \quad (4.22)$$

Chapter 5

MODEL PARAMETER CALIBRATION UNDER UNCERTAINTY INVESTIGATIONS

The Bayesian parameter calibration approach described in Chapter 4 was implemented in the calibration of constituent material parameters for two FRP composite material systems. In the first investigation, the proposed calibration method was implemented to identify the underlying material parameter distributions from experimental data acquired from off-axis loaded unidirectional S2-glass/epoxy composite specimens, and is presented in Section 5.1. The second investigation, included in Section 5.2, implements the Bayesian calibration scheme to calibrate underlying material parameter distributions from lamina-scale experiments of IM7/977-3 carbon FRP composites and also predicts the ultimate strength of laminated composite layups from the calibrated material distributions.

5.1 Uncertainty Quantification at the Lamina Scale

. The proposed model calibration and uncertainty quantification approach was employed to evaluate the response of unidirectional S2-glass/epoxy composite materials. In this study, the effective composite response of a unidirectional lamina was used to calibrate the underlying random constituent material parameters of the fiber and matrix which comprise the composite. The Bayesian calibration method was employed with MCMC sampling and GP surrogate modeling to quantify the distributions of the material parameters for the rate-dependent damage evolution model described in Section 2.3.2. The calibration was validated by comparing the simulation result of randomly sampled parameter sets from the calibrated distributions with the experimental results. It is noted that the EHM model is not exercised in this study, but rather this study presents a significant step in propagating randomness between the lamina or RVE scale and the constituent material scale. This work below was published in the International Journal for Multiscale Compu-

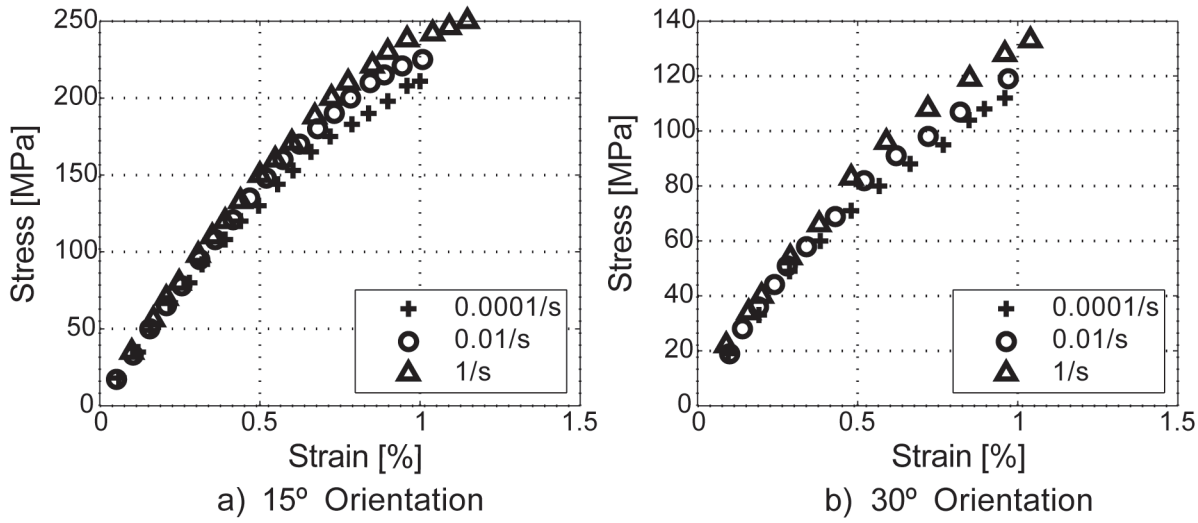

Figure 5.1: Uniaxial Tensile Stress Strain Curves for (a) 15° and (b) 30° Off-Axis Specimens [99]

tational Engineering [14].

Off-axis specimens loaded uniaxially to failure at angles of 15° and 30° to the fiber direction with strain rates of 0.0001/s, 0.01/s and 1/s, were considered in this study. The stress strain curves for these tests, as originally provided by Thiruppukuzhi and Sun [99], are shown in Figure 5.1. The ultimate strength and the strain to failure for each of the six tests were used in the calibration effort. This data set provides a fairly sparse amount of information for calibration. As such, only a subset of the model parameters available were calibrated, specifically $a^{(f)}$, $b^{(f)}$, $p^{(f)}$, and $q^{(f)}$ (f indicates the fiber phase and m the matrix).

An RVE with a fiber ratio of 65%, shown in Figure 5.2, with periodic boundaries, was created as a homogenization of the structural scale response for the unidirectional GFRP composite. Strain load was applied to the RVE by defining relative displacements between the periodic boundaries equivalent to the transformed strains from the off-axis loadings. The fiber and matrix phases were both meshed with tetrahedral elements, with 1806 total elements used to define the RVE.

The elastic parameters of the fiber and matrix were chosen assuming isotropic behavior at the microscale such that the elastic moduli of the overall composite material at 15° and 30° to the fiber longitudinal direction match the experimental data. The fiber was modeled with modulus of elasticity, $E_f = 60$ GPa, and Poisson ratio, $\nu_f = 0.30$; the matrix with $E_m = 4.775$ GPa and

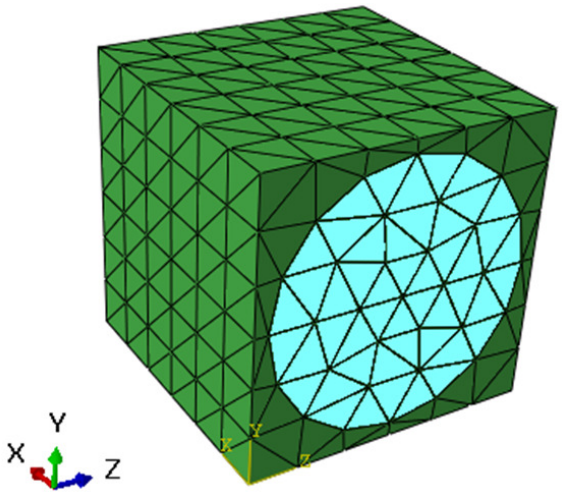

Figure 5.2: Representative Volume Element of the S2-glass GFRP Composite.

$\nu_m = 0.29$. Neglecting interface damage, 12 parameters remained ($a^{(\gamma)}$, $b^{(\gamma)}$, $p^{(\gamma)}$, $q^{(\gamma)}$, $c^{(\gamma)}$, and $\upsilon_{0^{(\gamma)}}$ for both the fiber and matrix from Equations 2.37, 2.45, 2.46, and 2.49) governing the material response of the RVE. $c^{(\gamma)}$ is used to account for the difference in damage behavior under tensile and compression loadings and was set to 0 for both phases since only tensile loading was considered. $\upsilon_{0^{(\gamma)}}$, the threshold value below which no damage occurs in the phase set to zero for both the fiber and matrix, as well, since only ultimate response was considered in this study. This left the eight damage evolution parameters, $a^{(m)}$, $b^{(m)}$, $p^{(m)}$, $q^{(m)}$, $a^{(f)}$, $b^{(f)}$, $p^{(f)}$, and $q^{(f)}$, unknown. In this investigation, the parameters governing the matrix response were set at deterministic values ($a^{(m)}$ = 2.0, $b^{(m)}$ =1.5, $p^{(m)}$ = 2.5, and $q^{(m)}$ = 0.001) and the damage parameters of the fiber were calibrated. The sensitivity of the damage model response to each of the four parameters, $a^{(f)}$, $b^{(f)}$, $p^{(f)}$, and $q^{(f)}$, was evaluated using a one-element model to set bounds on the prior distributions of each of these parameters in the calibration. Twelve sets of these model parameters were selected using Latin Hypercube sampling and were each used to simulate the six strain rate and strain orientation input conditions from the experimental data. GP models were trained for each experiment for ultimate stress, $\sigma^{(f)}$, and strain to failure, ε_f. The experimental data was then used to calibrate the parameters of the damage model and discrepancy function as well as the standard deviation of the measurement errors.

5.1.1 Parameter Sensitivity Study

The prior distributions for the four calibrated material parameters were obtained by evaluating the damage evolution in a one-element model for the effect that each parameter displayed on the stress-strain and strain-damage relationships. The distributions of the parameters $a^{(f)}$, $b^{(f)}$, $p^{(f)}$, and $q^{(f)}$ were selected, considering the nonlinear relationships in these variables, to keep the ultimate strength and strain to failure values within a reasonable range of the experimentally observed values when RVE failure occurs. The rate of damage growth in the constituent is primarily governed by $a^{(f)}$ and $b^{(f)}$. As $a^{(f)}$ increases, the strain to failure decreases and the ultimate stress attained decreases, seen in Figure 5.3. Figure 5.4 shows the effects of $b^{(f)}$ on stress, strain, and damage with damage accumulating faster for larger $b^{(f)}$ values, accompanied by lower stress values.

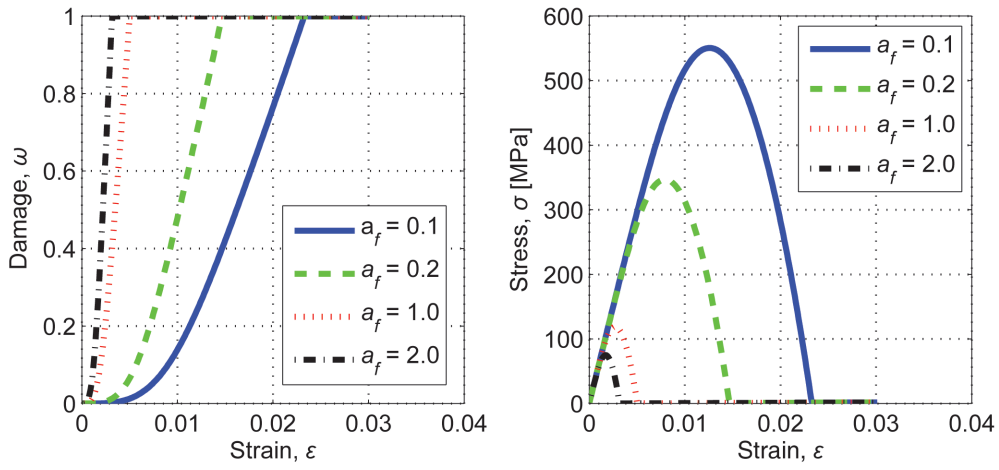

Figure 5.3: Effect of $a^{(f)}$ on Damage vs. Strain and Stress vs. Strain Behavior.

The parameters $p^{(f)}$ and $q^{(f)}$ govern the rate-dependency of the damage evolution. Figure 5.5 shows the effect of three different values of $p^{(f)}$ for each of the strain rates considered. As $p^{(f)}$ increases, the response becomes more rate-dependent. Figure 5.6 shows the effect of $q^{(f)}$ on the rate dependency of the damage accumulation model. For greater $q^{(f)}$ values, the difference between growth rates from different strain rates is more pronounced.

This analysis yielded prior uniform distributions for the parameters as $a^{(f)} = [0, 0.2]$, $b^{(f)} =$

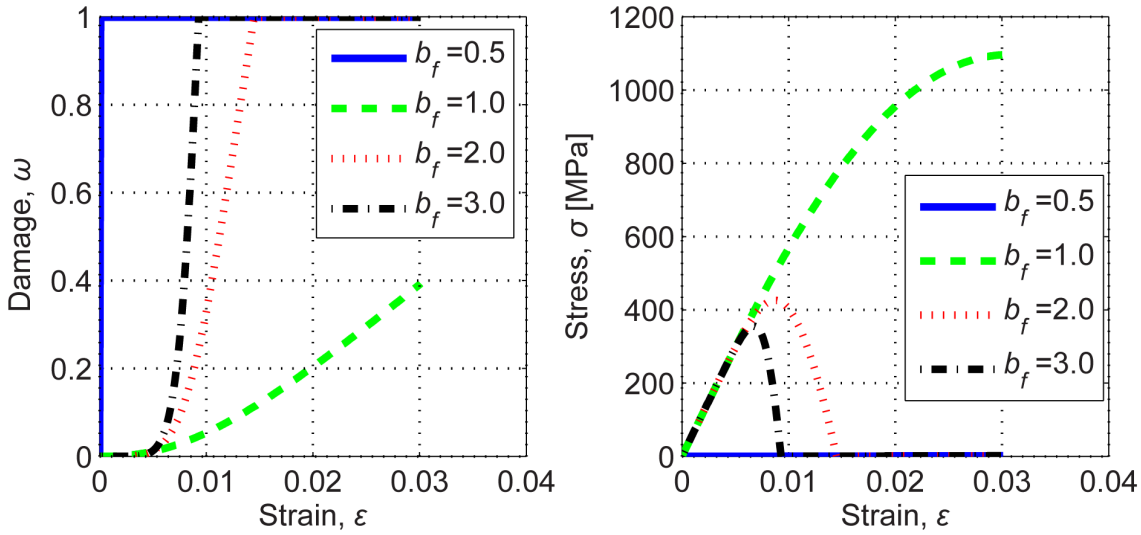

Figure 5.4: Effect of $b^{(f)}$ on Damage vs. Strain and Stress vs. Strain Behavior.

$[1, 2]$,$p^{(f)} = [1, 2]$, and $q^{(f)} = [0, 0.001]$.

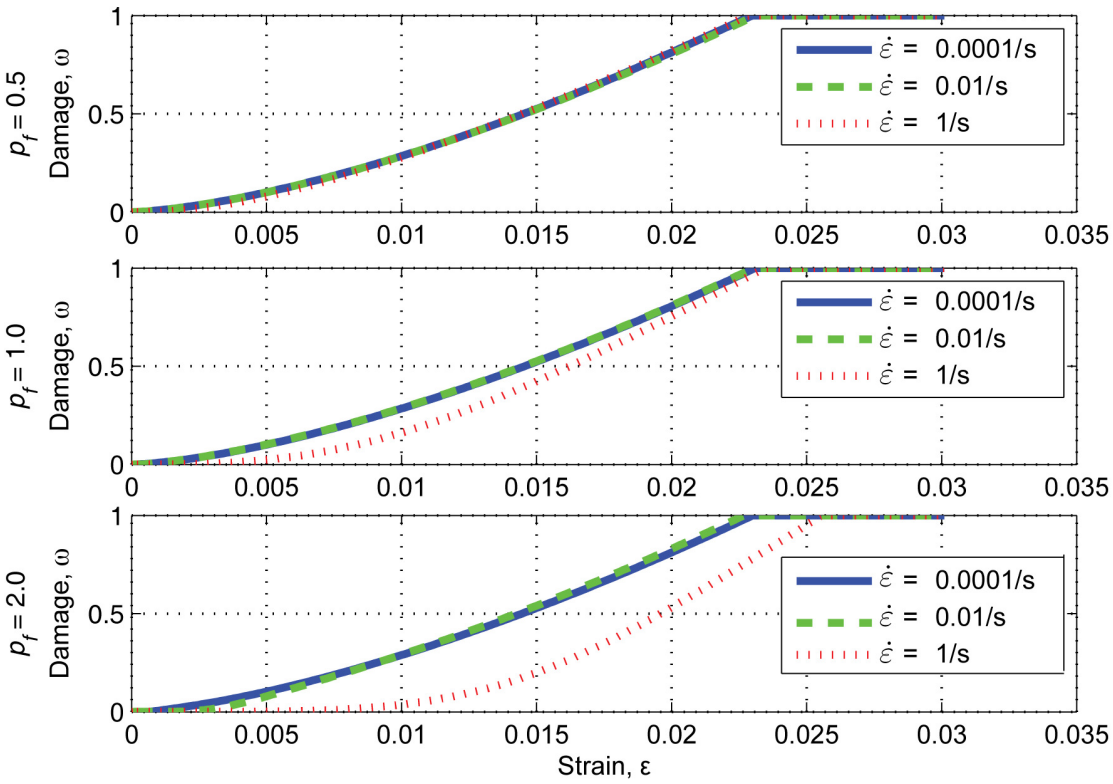

Figure 5.5: Effect of $p^{(f)}$ on Rate Dependence of Damage Accumulation.

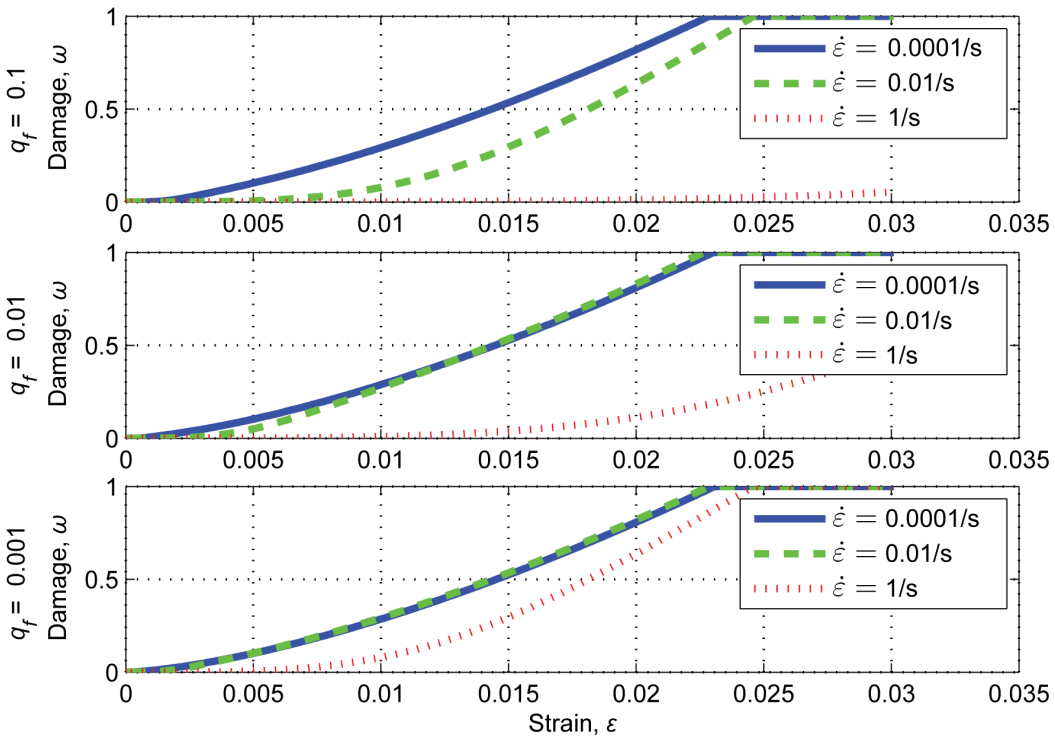

Figure 5.6: Effect of $q^{(f)}$ on Rate Dependence of Damage Accumulation.

5.1.2 Simulation and GP Model Training

Using Latin Hypercube sampling to draw twelve sets of model parameter values from the prior distributions above and the six experimental input conditions, 72 finite element simulations were performed. From these simulations, the stress at the macroscale of the composite was computed as the component of the homogenized stress acting in the direction of the strain loading. As the RVE was loaded with the strain oriented at an angle to the fiber direction, the face of the RVE transverse to the fiber direction accumulated damage at the fastest rate (see Figure 5.7). Structural failure occurred when the stress carrying capacity in this direction was lost. The resulting stress-strain curves from all 72 simulations are shown alongside the experimentally obtained curves in Figure 5.8.

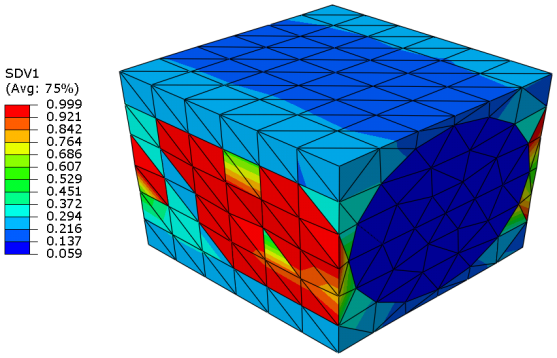

Figure 5.7: Matrix Damage Accumulation Transverse to the Fiber Direction.

The ultimate stress and the strain to failure from these simulations were used to train twelve GP models. A mean (trend) function was used in the training of the GP models as a first fit for the outputs to the model parameters. To account for the nonlinearity in the model, the form of the mean function was:

$$\hat{y}_{mean} = c_0 + c_1 a^{(f)} + c_2 b^{(f)} + c_3 {a^{(f)}}^2 + c_4 {b^{(f)}}^2 + c_5 {a^{(f)}}^3 + \frac{c_6}{a^{(f)} b^{(f)}} + c_7 p^{(f)} + c_8 \ln(q^{(f)}) \quad (5.1)$$

where $\hat{y}_{mean}$ is the mean function prediction and $c_{0...8}$ are the coefficients of the mean function. These coefficients were determined from least-squares regression for each of the twelve surrogate models. Using this form for the mean function yielded predictions with R-squared values from

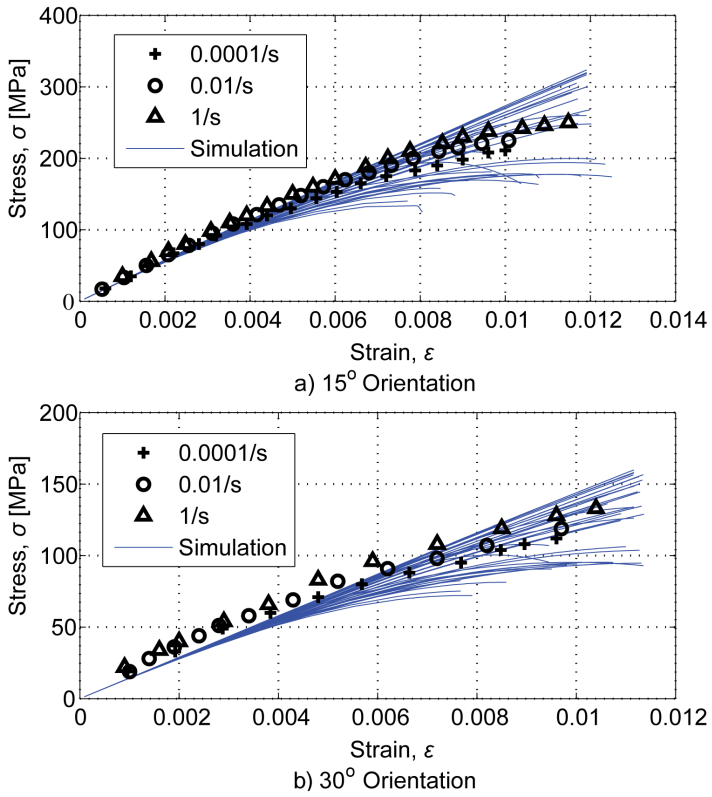

Figure 5.8: Simulated and Experimental Stress vs. Strain curves for (a) 15° and (b) 30° Load Application.

0.9 to 0.99 for each of the twelve data sets. The GP model, with a squared exponential covariance function, was then trained using the difference between the mean function prediction and the actual training value.

5.1.3 Model Discrepancy and Measurement Error

Recalling Equation 4.1, the trained GP model provides the surrogate for the FEM model prediction, $\hat{y}(\mathbf{x}, \theta)$, while the discrepancy, $\delta(\mathbf{x})$, and measurement error, $\varepsilon^{(m)}$, must still be addressed. In this study, it was assumed that the model discrepancy was only a function of the strain-rate, $\dot{\epsilon}$, and that the function was the same for both the 15° and 30° tests:

$$\delta(\mathbf{x}) = b_0 + b_1 \ln(\dot{\epsilon}) \tag{5.2}$$

where b_0 and b_1 are the coefficients of the discrepancy term to be calibrated (two for the stress discrepancy and two for the strain discrepancy). The prior distributions for these coefficients were taken as uniform: b_{0_σ} = [-10,10], b_{1_σ} = [-2,2], b_{0_ϵ} = [-1,1], b_{1_ϵ} = [-0.01,0.01].

Output measurement error was taken as a Gaussian random value with zero mean and standard deviation, $\sigma^{(m)}$. Since two types of outputs, ultimate stress and strain to failure were utilized in this calibration process, two separate values of measurement error standard deviation were calibrated, σ_{m_σ} and σ_{m_ϵ}, for the stress and strain respectively. It was assumed that the measurement error was independent of the load orientation angle strain rate. The prior density of the standard deviation, based on the Fisher information criterion [29] is given as:

$$f'(\sigma^{(m)}) \propto \frac{1}{\sigma^{(m)}} \tag{5.3}$$

The prior of the standard deviation was assumed to be uniform from 0.1 to 20 MPa for stress and 0.001% to 0.1% for strain.

5.1.4 Calibration Results

The distributions of ten variables were to be calibrated using MCMC sampling: $\theta = a^{(f)}$, $b^{(f)}$, $p^{(f)}$, $q^{(f)}$, b_{0_σ}, b_{1_σ}, b_{0_ϵ}, b_{1_ϵ}, σ_{m_σ}, σ_{m_ϵ}. For each loop in the MCMC sampling, a random value was sampled from each distribution. Assuming independence, the prior probability of this set was proportional to the product of the inverse of the standard deviations, as all the other values were sampled from uniform distributions. Using $a^{(f)}$, $b^{(f)}$, $p^{(f)}$, and $q^{(f)}$, the GP model predictions for the twelve outputs were calculated. The discrepancy values were calculated from b_{0_σ}, b_{1_σ}, b_{0_ϵ}, b_{1_ϵ}, using Equation 5.2, and added to the GP prediction. The measurement error standard deviations σ_{m_σ} and σ_{m_ϵ} were then used to compute the likelihood of observing the experimental outputs given those model parameters and discrepancy values. MCMC simulation was then carried out for five hundred thousand samples until the chain converged. The results for the calibrated distributions of the four model parameters are shown in Figure 5.9 through Figure 5.12. In each of the graphs, posterior distribution of the parameters can be seen to tighten and show preference to a narrower

band of values. Each of the graphs shows one major spike in the parameter values, with some minor spikes away from the large spike. This is partly attributed to the nonlinearity of the model and numerical artifacts from the MCMC method.

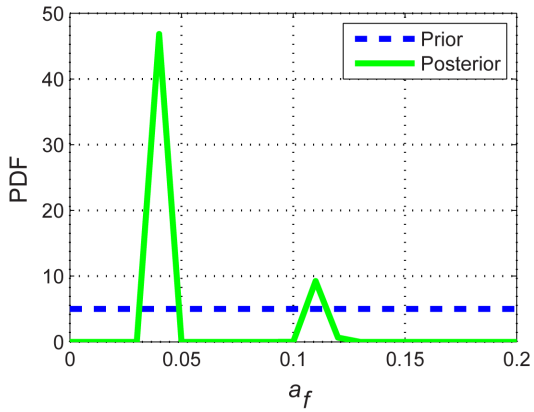

Figure 5.9: Calibrated Distribution of $a^{(f)}$.

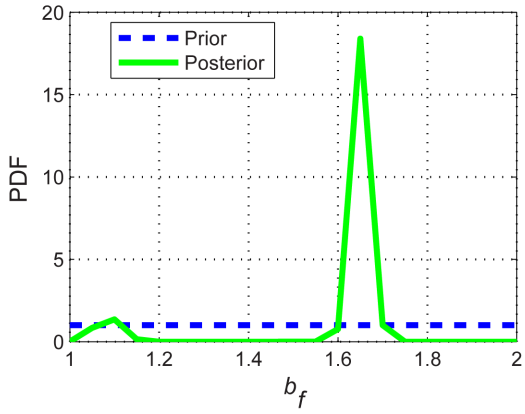

Figure 5.10: Calibrated Distribution of $b^{(f)}$.

Apart from the natural variability in the material parameters, two major sources of uncertainty exist in the model: model discrepancy and measurement error. Surrogate model error was estimated by using the "leave-one-out" approach. In the calibration procedure, this surrogate model error was included in the calibrated model discrepancy. Model discrepancy and measurement error were evaluated during the calibration process. The estimated error in the surrogate model is given in Table 5.1. The variance in the stress prediction error was high, indicating that additional training points are needed to reduce the epistemic uncertainty. With four parameter dimensions, twelve

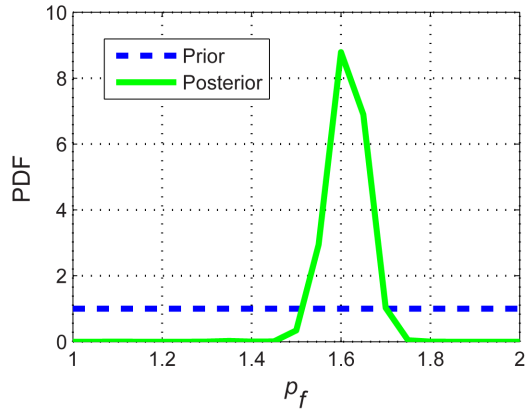

Figure 5.11: Calibrated Distribution of $p^{(f)}$.

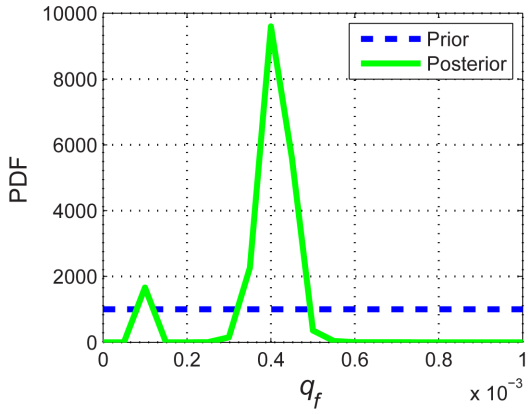

Figure 5.12: Calibrated Distribution of $q^{(f)}$.

training points can miss nonlinearities in the model response.

The parameters of the model discrepancy (including model form error and solution approximation error), calibrated simultaneously with the model parameters, are shown in Figure 5.13 for stress and Figure 5.14 for strain. If there were no discrepancies in the model, each of the coefficients would be equal to zero. As this is not the case, it is apparent that the damage model or surrogate model has a discrepancy in capturing all of the rate-dependent effects in the material response.

The final uncertainty measure that was calibrated is the standard deviation of the measurement error. The posterior distributions for stress and strain measurements are displayed in Figure 5.15. These graphs indicate that the standard deviation of the measurement error in the stress is around

Table 5.1: GP Surrogate Model Error.

Output	Strain Rate	Strain Orientation	Surrogate Model Error Mean	Surrogate Model Error Variance
Stress	0.0001/s	15°	0.0142	53.1
Stress	0.01/s	15°	-0.0050	37.5
Stress	1/s	15°	-0.5016	134.4
Stress	0.0001/s	30°	-0.0777	5.6
Stress	0.01/s	30°	-0.0616	1.4
Stress	1/s	30°	-0.2251	30.9
Strain	0.0001/s	15°	0.001172	0.000479
Strain	0.01/s	15°	0.000690	0.000186
Strain	1/s	15°	-0.000487	0.001545
Strain	0.0001/s	30°	-0.000197	0.000315
Strain	0.01/s	30°	0.000270	0.000487
Strain	1/s	30°	-0.000075	0.001293

2 MPa and for strain around 0.01%. Additional experimental observations are required to generate more accurate predictions of the measurement error.

The calibrated model parameters were used to draw samples of the predicted outputs using Equation 4.1. This prediction for the first experimental set-up with a strain rate of $0.0001/s$ and strain applied at a 15° angle to the fiber direction is shown in Figure 5.16. A significant amount of scatter remains around the observed value for the output, but the calibration shows reasonable performance in achieving results close to the observations. While the range of predicted strain to failure appears to be centered on the observed results, the range of predicted ultimate stress tends to be biased below the observed value. The calibration and prediction accuracy can be improved with further testing and a larger experimental data set. As such, there is not enough data to compare the statistics of the predicted outputs with the true material behavior. However, the variance in the model predictions is on the order of material behavior expected for composite materials.

5.2 Uncertainty Quantification at the Laminate Scale

To build upon the work of the previous section, the proposed probabilistic multiscale calibration approach was applied to investigate the rate-dependent response of IM7/977-3 carbon fiber

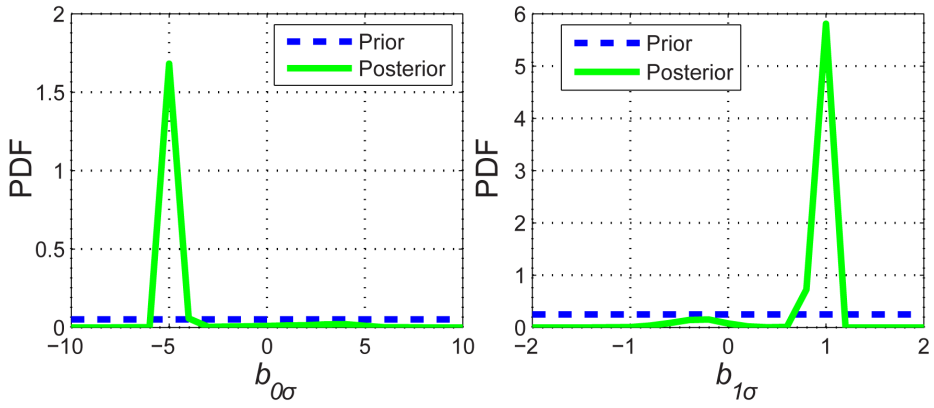

Figure 5.13: Model Discrepancy Parameters for Stress Prediction ($\delta(\mathbf{x}) = b_0 + b_1 \ln(\dot{\epsilon})$).

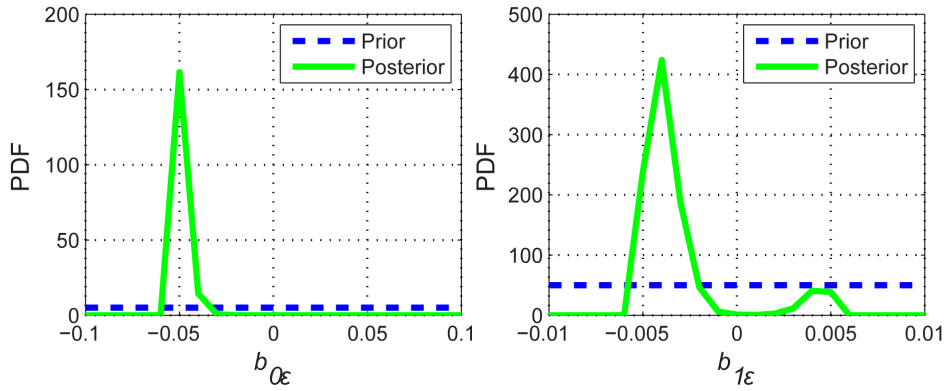

Figure 5.14: Model Discrepancy Parameters for Strain Prediction ($\delta(\mathbf{x}) = b_0 + b_1 \ln(\dot{\epsilon})$).

reinforced composite laminates. The random distribution of microscale failure properties was calibrated based on ply-level experimental data. The calibrated model predictions from EHM were validated against separate experimental measurements of the ultimate tensile strength of quasi-isotropic open-hole composite specimens at various loading rates. The effect of macroscopic spatial distribution of the constituent failure properties on the composite response was also investigated through a parametric analysis. This study was initially presented at the AIAA SciTech 2013 conference [15] and published in Computational Mechanics [17].

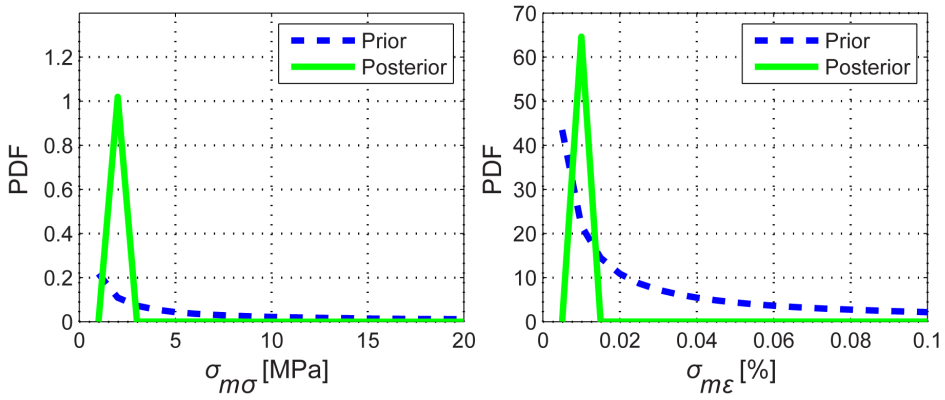

Figure 5.15: Measurement Error Standard Deviation for Stress and Strain.

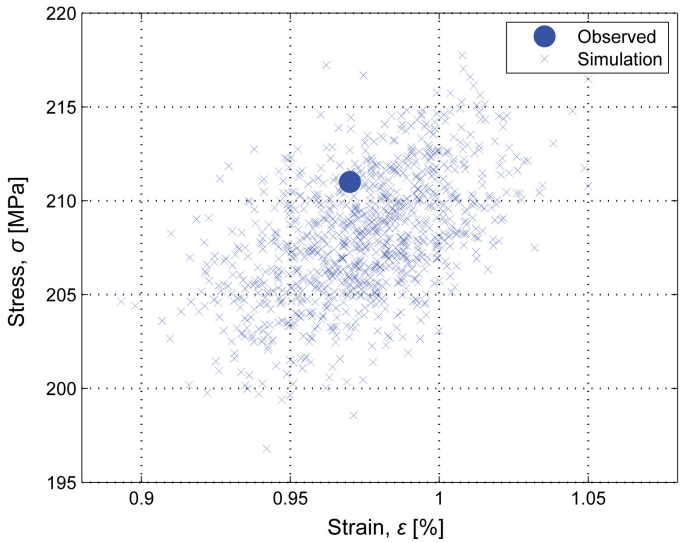

Figure 5.16: Sampled Failure Predictions for 0.0001/s Loading Rate at 15°.

5.2.1 Experimentation

A suite of experiments was conducted to calibrate the material parameters and validate the proposed computational model for rate dependent damage accumulation in carbon fiber reinforced epoxy composite laminates. IM7/977-3 composite specimens with three separate layups of unidirectional laminae were tested: (a) 0° specimens consisting of eight unidirectional plies with fibers oriented parallel to the coupon length; (b) 90° specimens consisting of sixteen unidirectional plies with the fibers oriented perpendicular to the coupon length; and (c) open-hole quasi-isotropic

specimens with a layup of $[+45, 0, -45, 90]_{2S}$ and hole diameter of 6mm. Specimen configurations are summarized in Table 5.2. The mean fiber volume fraction of the specimens was determined to be 65% based on acid digestion testing. Monotonic tension experiments were conducted on

Table 5.2: IM7/977-3 Nominal Specimen Dimensions.

Fiber orientation	Number Of plies	Length (mm)	Width (mm)	Thickness (mm)	# specimens tested
0°	8	250	13	1	12
90°	16	100	13	2	25
$[+45, 0, -45, 90]_{2S}$	16	250	38	2	6

the 0° specimens according to ASTM Standard D3039 [5] at a quasi-static displacement rate of 1.0 mm/min. Strain in the 0° specimens was measured using a centrally located extensometer. Applied load was measured directly from the testing machine and stress was calculated over the gross cross section of the specimen. Three point bend tests were performed on the 90° specimens with a span length of 44.7 mm at midpoint displacement rates of 0.1 mm/min, 1.0 mm/min, and 100 mm/min according to ASTM Standard D790 [11]. The midpoint displacement and applied load were measured directly from the testing machine. Stress and strain at the bottom of the beam at midspan were calculated from elastic beam theory. The quasi-isotropic specimens were tested according to ASTM Standard D5766 [10] at displacement rates of 1.0 mm/min and 100 mm/min. Strain was measured using a 1-inch long extensometer centered on the hole. Applied load was measured from the testing machine and stress was computed over the gross cross-sectional area of the specimen. All tests were performed on an MTS universal testing machine.

5.2.2 Calibration and Validation

Random failure parameters for the fiber and matrix constituents of IM7/977-3 composites were probabilistically calibrated using experimental data from the 0° and 90° unidirectional specimens at varying load rates. EHM with random failure parameters was employed to predict the failure strength for a quasi-isotropic IM7/977-3 laminated composite with an open hole under tension at

a fast and slow loading rate to demonstrate the rate-dependence and uncertainty quantification of the model. These results of the laminated composite predictions were compared to experimental results at two applied strain rates.

5.2.3 Model Calibration

The rate-dependent damage evolution model contains six parameters describing the failure evolution in a part. Every part that lays within the subdomain of the same constituent is associated with an identical parameter set. For instance, given $\boldsymbol{\psi}^{(m)} = \{a^{(m)}, b^{(m)}, \upsilon_0^{(m)}, p^{(m)}, q^{(m)}, c^{(m)}\}$ is the set of random parameters defining failure in the matrix and the set of random fiber failure parameters, $\boldsymbol{\psi}^{(f)}$, is defined similarly, then:

$$\begin{cases} \boldsymbol{\psi}^{(\gamma)} = \boldsymbol{\psi}^{(m)} & \text{if } \theta^{(\gamma)} \in \theta^{(m)} \\ \boldsymbol{\psi}^{(\gamma)} = \boldsymbol{\psi}^{(f)} & \text{if } \theta^{(\gamma)} \in \theta^{(f)} \end{cases} \tag{5.4}$$

where $\theta^{(m)}$ and $\theta^{(f)}$ denote the subdomains of the RVE occupied by the matrix and fiber, respectively. The set of random failure parameters of the proposed model is therefore:

$$\boldsymbol{\psi} = \{\boldsymbol{\psi}^{(m)}, \boldsymbol{\psi}^{(f)}\} \tag{5.5}$$

It is natural to consider the elastic moduli tensor of the constituent materials as random variables due to the presence of manufacturing induced defects in a composite microstructure. The effect of variability in elastic moduli of constituents on effective composite properties has been established in a number of publications (e.g. Refs. [23, 32, 50, 81, 88]). However, the focus of the present effort is on failure parameters only and therefore the moduli were set as deterministic, with values shown in Table 5.3. The fiber parameters were calibrated from the 0° tension tests as fiber breakage was the primary failure mode. Likewise, the 90° three point bending tests isolated matrix cracking as the failure mode and were used for matrix parameter calibration. The response of the two distinct microstructural materials were sufficiently isolated by calibrating the constituent components of the computational model in this manner.

Table 5.3: Elastic Parameters of Fiber and Matrix.

$E^{(m)}$ [GPa]	$E_1^{(f)}$ [GPa]	$E_2^{(f)}$ [GPa]	$G_{12}^{(f)}$ [GPa]	$v^{(m)}$	$v_{12}^{(f)}$	$v_{23}^{(f)}$
3.55	263.0	13.0	27.5	0.35	0.32	0.20

A total of 12 material parameters (6 for the matrix and 6 for the fiber) define the rate dependent failure behavior of the composite constituents, as outlined in Table 5.4. For both constituents, the damage thresholds ($\upsilon_0^{(m)}$ and $\upsilon_0^{(f)}$) were taken to vanish, implying that damage accumulation occurs from the onset of loading. The tension-compression anisotropy parameters ($c^{(m)}$ and $c^{(f)}$) were set such that damage accumulates only under tensile loading (compression loading is not considered in this study). Because carbon fibers do not exhibit significant rate dependence, $p^{(f)}$ and $q^{(f)}$ were set to 100 and 1, respectively, which mimics the rate independent limit. The remaining six parameters were calibrated using the proposed Bayesian approach. The results of the 0° monotonic tension tests were employed to calibrate the failure behavior of the fiber (i.e. $a^{(f)}$ and $b^{(f)}$) since fiber failure dominates the failure response in these experiments. The three point bending test results were used to calibrate the matrix failure parameters (i.e. $a^{(m)}$, $b^{(m)}$, $p^{(m)}$, and $q^{(m)}$). The quasi-isotropic specimens were used to validate the response predictions. The ROM representing the IM7/977-3 microstructure with 65% fiber volume fraction used in this study is described in Sec. 3.1.2.1.

Table 5.4: Material Properties Describing Rate Dependent Damage Evolution.

Property	Description	Equation
$a^{(\gamma)}$	Governs magnitude of failure	Eq. (2.46)
$b^{(\gamma)}$	Governs ductility of failure	Eq. (2.46)
$p^{(\gamma)}$, $q^{(\gamma)}$	Control rate-dependence	Eq. (2.49)
$c^{(\gamma)}$	Control compression/tension anisotropy	Eq. (2.37)
$\upsilon_0^{(\gamma)}$	Threshold value of $\upsilon^{(\gamma)}$ below which no damage occurs	Eq. (2.46)

The stress-strain curves from the twelve 0° monotonic tension tests are shown in Fig. 5.17. The experimental longitudinal mean failure stress, X_1, and failure strain, ϵ_1, were 2785 MPa and 1.64%, with standard deviations of 297.2 MPa and 0.185%, respectively. The range of failure stress

was [2435,3300]MPa, with failure strain in the range of [1.26%,1.87%]. All of the 0° tension tests failed under sudden and catastrophic fiber failure, as seen in Fig. 5.18.

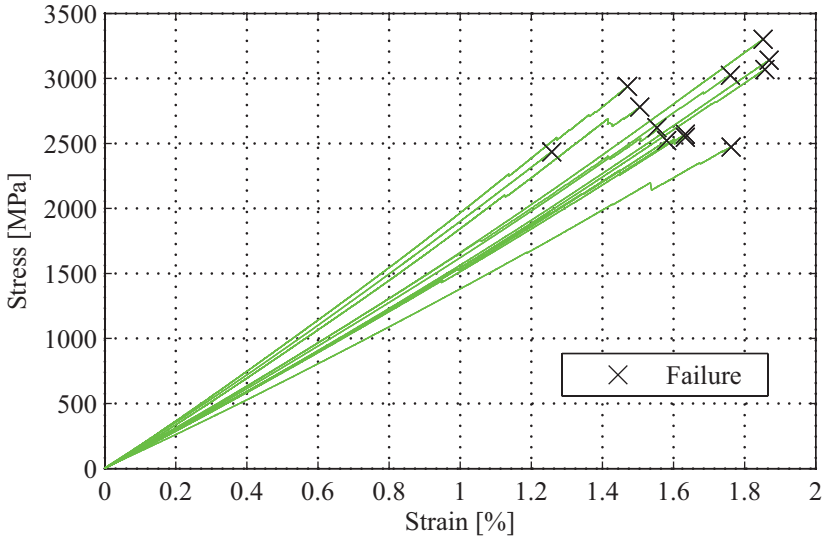

Figure 5.17: Stress vs. Strain Curves for 0° Tension Experiments.

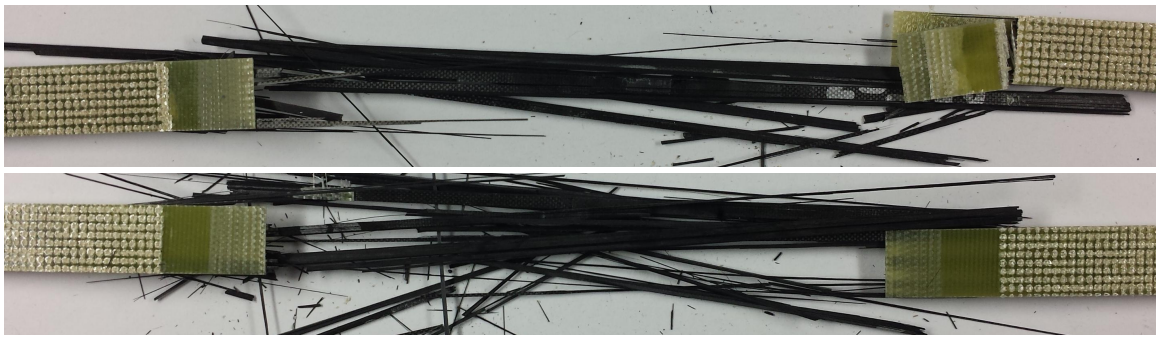

Figure 5.18: Failure Image from 0° Monotonic Tension Experiments.

The quantity of interest, ϕ_{lam}, employed in the calibration procedure for the fiber behavior was the ultimate stress of each replicate. The 12 failure stress values obtained from the 0° experiments were used to formulate the likelihood function (Eq. 4.11) in the MCMC calibration of the fiber damage evolution properties. Fifty multiscale finite element simulations were evaluated using EHM and the rate-dependent damage evolution law to train the GP surrogate model of the 0° tension test. The parameters for these simulations were selected using Latin hypercube sampling. One million MCMC steps were performed using the GP model and the resulting chain was used

to quantify the distributions of $a^{(f)}$ and $b^{(f)}$. From the sampled MCMC chains, probability density functions (PDFs) were computed using KS density estimation. The covariance matrix C of the parameters was calculated using Eq. (4.14). The posterior distributions for the fiber constituent parameters are displayed in Fig. 5.19 against the uniform prior distributions. The results for the

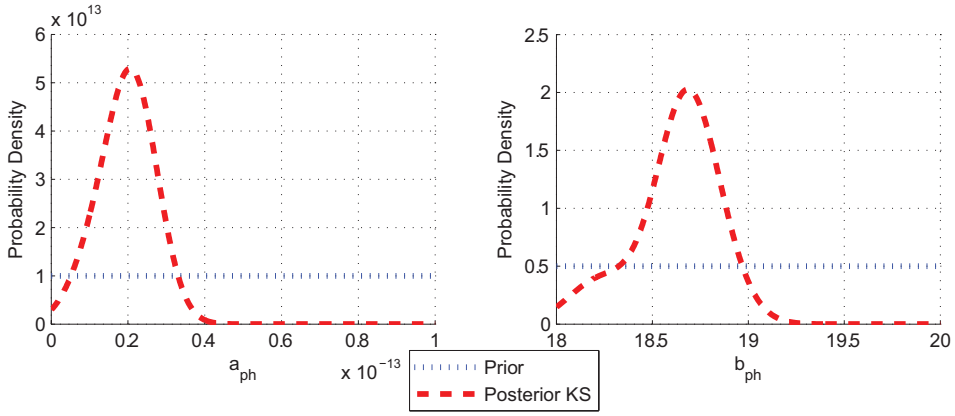

Figure 5.19: Calibrated Distributions for Fiber Parameters.

calibration of the matrix parameters are displayed in Fig. 5.20. The calibration of the matrix parameters from the three point bending experiments yields distinct peaks in probability for all four of the calibrated material parameters.

Since the calibration of the model was performed based on the GP model and the GP model is an approximation to the response surface generated by the actual multiscale model, it is necessary to "verify" the calibration procedure directly with the multiscale model predictions. Verification in this case refers to the comparison of the experimental data with full multiscale model simulations performed by drawing samples from the calibrated parameter distributions; i.e., that the calibration process achieved its intended result. The verification of the fiber parameter calibration was conducted by drawing ten thousand samples. The PDF of the verification result is plotted in Fig. 5.21 against the KS density distribution of experimental results. Tick marks indicate individual experimental values. The longitudinal failure stress and strain properties of the experiments and the calibrated model are summarized in Table 5.5. The calibrated distributions show good agreement in terms of the statistical mean and coefficient of variation for both stress and strain to failure. The

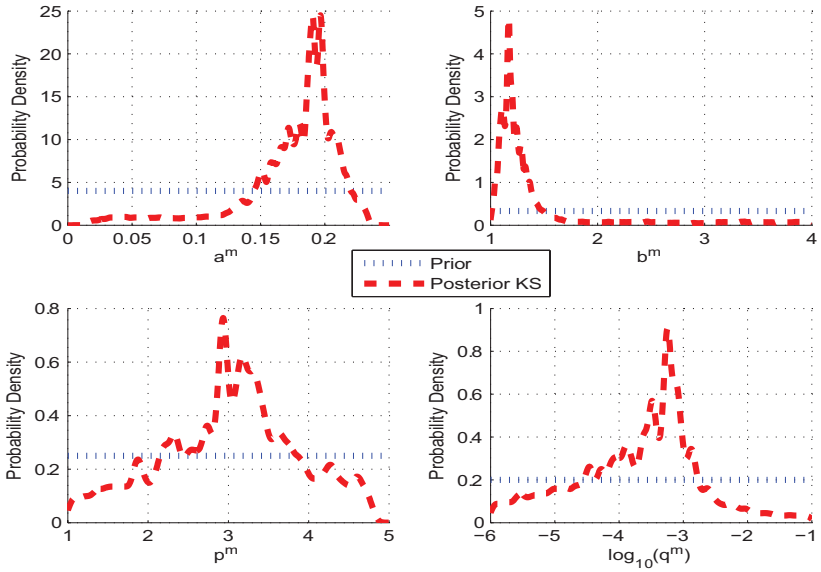

Figure 5.20: Calibrated Distributions for Matrix Parameters.

strain to failure data was not used in the generation of the likelihood function in the calibration process, but the resulting verification analysis shows good accuracy to this value.

Table 5.5: Experimental and Calibrated Failure Properties of 0° Tension Specimens.

		Experiments		Calibration	
Property		Mean	CoV	Mean	CoV
Longitudinal failure stress	X_1 [MPa]	2785	0.107	2752	0.124
Longitudinal failure strain	ϵ_1 [%]	1.64	0.113	1.74	0.125

The mean failure stress from the experiments and simulations were 2785 MPa and 2752 MPa, respectively, a difference of 1.2%. The standard deviation of the simulations, 340 MPa, is slightly higher than from the experiments, 297 MPa. The simulated results show a more exaggerated peak in probability near the cluster of experimental results around 2500 MPa. However, the tails of the PDFs of the failure stress for experiments and calibrated model (i.e. Fig. 5.21(b)) are in good agreement, indicating that the simulations captured the extreme values reasonably well. The mean failure strain from experiments was 1.64% while the simulations predicted a mean of 1.74%. This

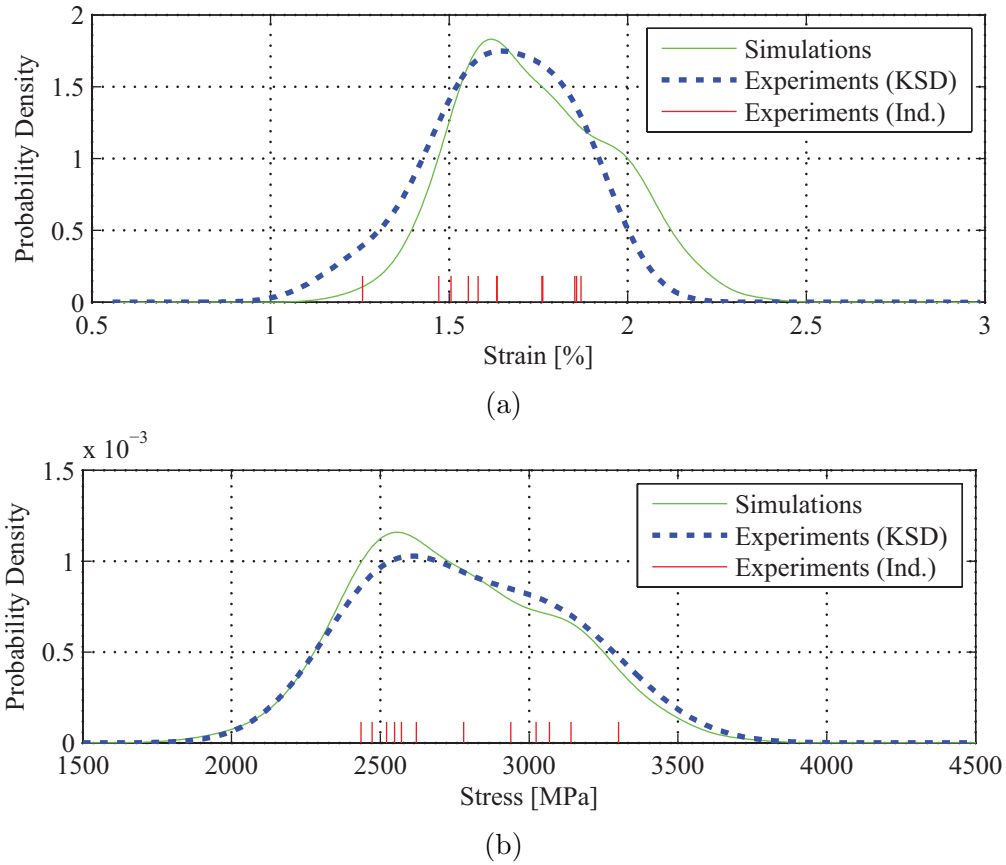

Figure 5.21: Experimentally Observed and Simulated PDFs from 0° Tension Specimens for (a) Failure Strain and (b) Failure Stress.

discrepancy is due to the fact that the damage evolution model was calibrated to match the failure stress only, as expressed above.

The failure parameters of the matrix were calibrated using the same procedure as the fiber parameters. The stress-strain curves of the unidirectional 90° specimens subjected to three point bending at three separate loading rates are shown in Fig. 5.22. The loading rate had a noticeable effect on the failure stress and strain to failure as further illustrated in Fig. 5.23. The mean transverse failure stress, X_2, of the specimens increased from 102.3 MPa at 0.1 mm/min to 118.3 MPa at 100 mm/min loading rates. Similarly, the mean transverse failure strain, ϵ_2, increased from 1.27% at 0.1 mm/min to 1.38% at 100 mm/min. The failure stress from all tests was in the range of [82 MPa,135 MPa] and the range of failure strains was [1.14%,1.61%]. The mode of failure for all of

the three point bending experiments was a single smooth matrix crack through the specimen at the midspan, under the loading point. The failure mode was consistent over all of the replicates at each of the loading rates.

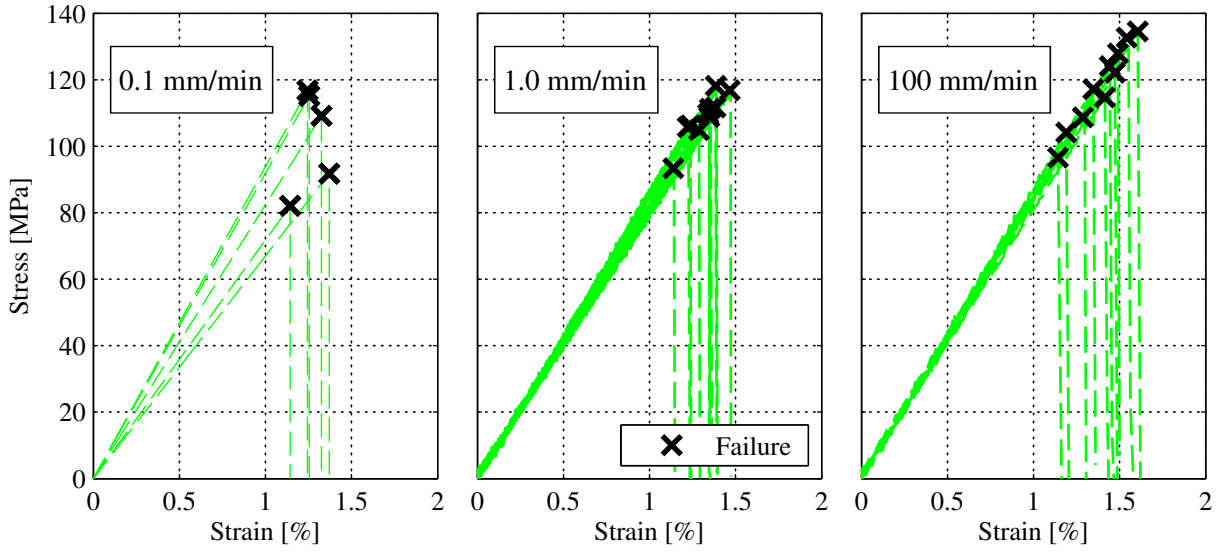

Figure 5.22: Stress vs. Strain Curves for 90° Three Point Bending Experiments for 0.1 mm/min, 1 mm/min, and 100 mm/min Displacement Rates.

The Bayesian calibration procedure was repeated to evaluate the distributions for the matrix failure parameters: $a^{(m)}$, $b^{(m)}$, $p^{(m)}$, and $q^{(m)}$. One hundred multiscale simulations were conducted using sampled training points to generate predictions with failure stresses within the range of 50 to 200 MPa and train the GP model. The failure behavior of the composite transverse to the fiber direction was idealized by modeling the critical region of the three point bending specimen at the bottom of the coupon at midspan. One million MCMC steps were performed using the GP model to generate the distributions of the failure parameters. In order to verify the calibration, random samples were drawn from the KS density distributions and ten thousand simulations were performed using the multiscale model.

Figure 5.24 compares PDFs of failure stress and failure strain of the three point bend specimens at the three loading rates from the multiscale model and the experimental data. The transverse failure stress and strain properties of the experiments and the calibrated model at each displacement rate are summarized in Table 5.6. The mean failure stresses in the simulations were 104.5, 108.7

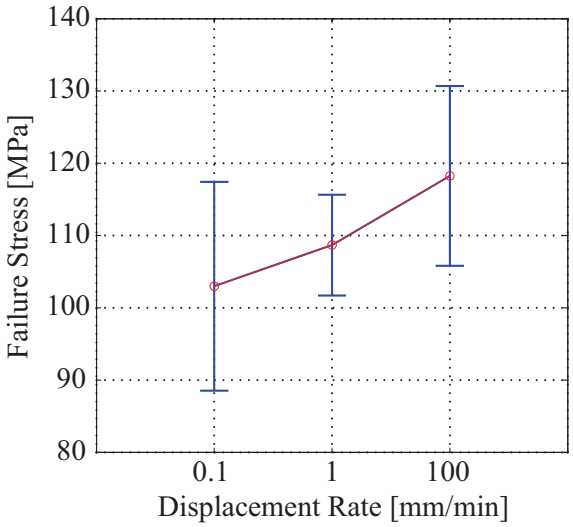

Figure 5.23: Effect of Loading Rate on Failure Stress in 90° Three Point Bending Specimens.

and 117.9 MPa for the 0.1 mm/min, 1 mm/min, and 100 mm/min displacement rates, respectively, compared with the experimental means of 102.3, 108.7, and 118.0 MPa. The average stress predictions were in good agreement with the average stress with percent errors of 2.2%, 0.0%, and 0.1% for the 0.1 mm/min, 1 mm/min, and 100 mm/min displacement rates, respectively. While ten experiments were used for the faster rate three point bend tests (1 mm/min and 100 mm/min), only five were available for the 0.1 mm/min rate, which partially explains the slightly higher discrepancy at the slowest rate. The mean failure strain for the slow, medium, and fast rate experiments respectively were 1.27, 1.32, and 1.38% compared to the mean from simulations of 1.22, 1.27, and 1.38%. The mean failure strain does not correspond to the peak of the PDFs shown in Fig. 5.22, which is the mode of the PDF and different than the mean for non-Gaussian distributions. The slight discrepancy in the failure strains is attributed to the fact that the likelihood function in the calibration process is computed based on the ultimate stress and not failure strain.

The standard deviations of failure stress from the experiments were 7.65, 6.97, and 12.44 MPa for the 0.1 mm/min, 1 mm/min, and 100 mm/min displacement rates, respectively. In the calibrated simulations, the standard deviations were 7.08, 6.62, and 8.37 MPa, respectively. The percent errors between predicted and experimental standard deviations were 7.4%, 5.0%, and 32.7%, respectively. The variance in the 0.1 mm/min and 1 mm/min displacement rates were in reasonable

agreement between the experiments and simulations. The experimental variance for the fastest displacement rate was much higher than for the slower two rates. This displacement rate was near the limits of the capabilities of the MTS testing machine. At the high rate of loading, the greater variance compared to the variance from the other experiments could be attributed to a greater degree of measurement error in the fastest displacement rate, as well as the presence of additional physical phenomena that were significant only at the highest loading rate. The standard deviation from the simulations performed at the fastest displacement rate was much closer to the simulations of the other two rates than was witnessed in the corresponding experiments.

The PDFs obtained through multiscale simulations with calibrated parameter distributions show some discrepancy with those obtained by the experiments. The primary reason for the discrepancies is the modeling error associated with the idealization of rate effects. The calibration of matrix material properties were performed to match behavior at three different load rates together. When parameters were allowed to vary from rate to rate (i.e., calibration performed using experiments loaded at a single rate), the experimental and simulated PDFs match to the same degree as Fig. 5.21. This result implies a better model is necessary to capture the rate effect compared to the power law used here. Nevertheless, a good match is observed between the primary distribution metrics (i.e. mean and variance).

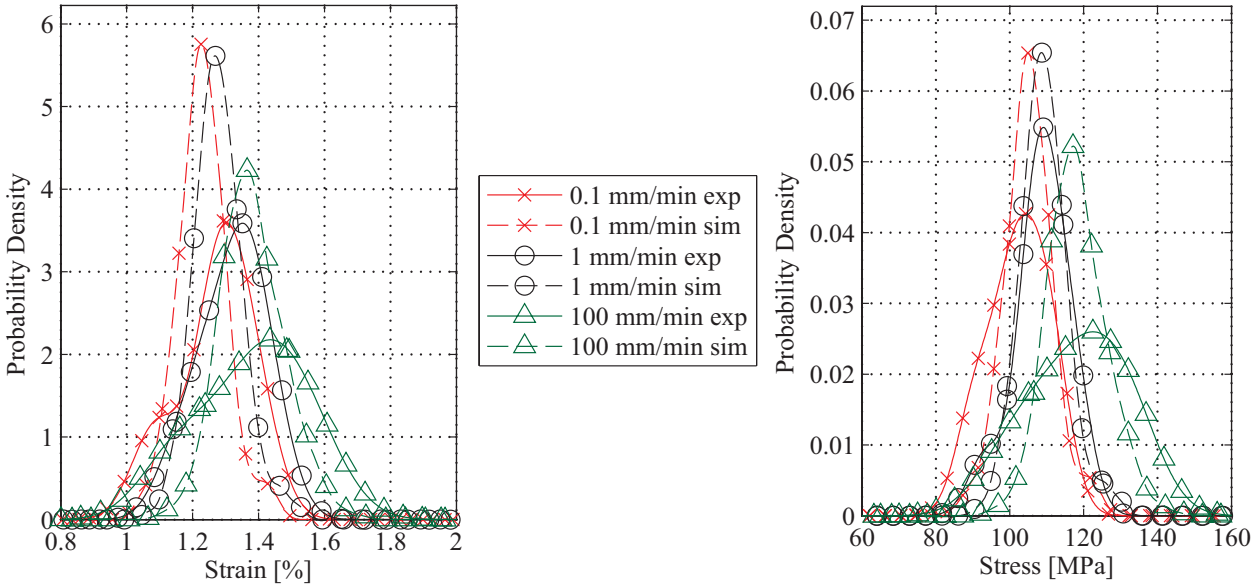

Figure 5.24: KS Density PDFs for Strain to Failure and Ultimate Stress for Experimental Results and Simulated Samples from Calibrated Parameter Distributions for 90° Monotonic Three Point Bending Tests.

Table 5.6: Experimental and Calibrated Failure Properties of 90° Three Point Bending Tests.

		Experiments		Calibration	
Property	Rate	Mean	CoV	Mean	CoV
X_f^2 [MPa]	0.1mm/min	102.3	0.075	104.5	0.068
	1 mm/min	108.7	0.064	108.7	0.061
	100 mm/min	118.3	0.105	117.9	0.071
ϵ_f^2 [%]	0.1mm/min	1.27	0.084	1.22	0.064
	1 mm/min	1.32	0.073	1.27	0.060
	100 mm/min	1.38	0.112	1.38	0.075

5.2.4 Model Validation

The calibrated EHM model with probabilistic material properties was employed to predict the failure response of open-hole quasi-isotropic [+45,0,-45,90]$_{2S}$ specimens subjected to uniaxial tension at two different strain rates and validated against the observed experimental data. Twenty random correlated parameter sets were drawn from the calibrated parameter distributions. These

parameters were used in multiscale simulations with the finite element discretization described in Section 3.1.2.2 and the IM7/977-3 ROM generated as in Section 3.1.2.1. The simulated stress strain curves at the loading rates of 1 mm/min and 100 mm/min are shown against the experiments in Fig. 5.25. The average failure stresses from the experiments were 471.2 and 486.8 MPa at the 1 mm/min and 100 mm/min loading rates, respectively. A consistent failure mechanism was observed in each of the open hole specimens, predominated by transverse matrix cracking at the hole in the 90° and $\pm 45^\circ$ plies and fiber failure in the 0° plies, as seen in Fig. 5.26. The corresponding average failure stresses predicted by the simulations was 476.5 MPa and 485.1 MPa. The predictions of the mean strength were in excellent agreement with the experimental observations. The standard deviation of failure stress from the experiments was 20.4 MPa and 31.2 MPa for the slow and fast loading rates, respectively, compared to 30.5 MPa and 34.1 MPa, respectively, from the calibrated predictions. It is noted that only three experiments were available for each loading rate and more comprehensive experimental datasets are needed to fully validate the proposed approach with regards to the standard deviation of the predictions.

The evolution of damage shown in Fig. 5.27 shows good qualitative agreement between the experimentally observed damage patterns and the predicted damage accumulation of the computational model. In the experiments, little damage was visible externally or with x-ray imaging before the load reached 80 percent of the failure stress. The images in Fig. 5.27 show the evolution from delaminations between plies inside the hole to surface cracks (transverse matrix failure) in the -45° ply, where the cracks propagate parallel to the fiber orientation in the ply. No noticeable differences were observed between the pattern of damage evolution for the two loading rates in either experiments or simulations, and the same patterns of damage were observed over each of the realizations.

The simulations shown in Fig. 5.25 considered the failure parameters of the composite constituents as randomly sampled from the calibrated distributions, but spatially uniform across the specimen. An additional investigation was performed to understand the effects of treating the material parameters as spatially varying over the specimen. The length scale parameter, l_r, was

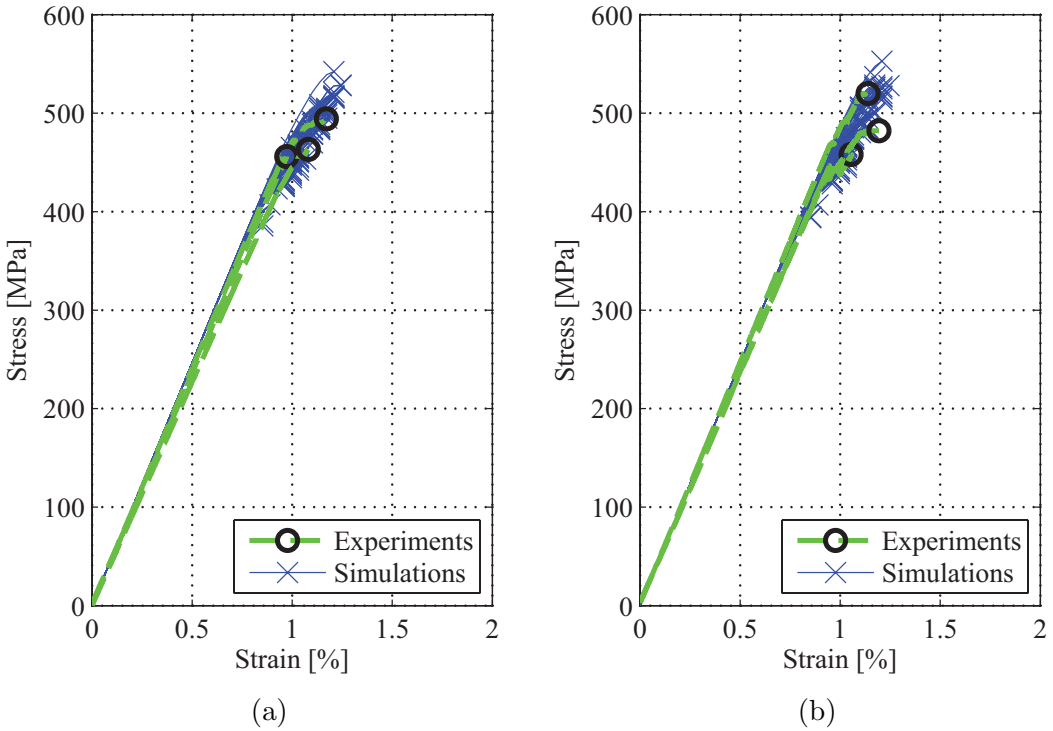

Figure 5.25: Stress vs. Strain Curves for Experiments and Simulations of Quasi-Isotropic Open Hole Specimens in Monotonic Tension at (a) 1 mm/min and (b) 100 mm/min.

introduced such that a structure with smaller l_r indicates more rapidly fluctuating parameter values across the specimen realization than one with a larger l_r. In this investigation, the random parameters were sampled for the structure in groups parallel to the fiber orientation of width equal to l_r, as shown in Fig. 5.28. This sampling method was selected as fiber properties were taken to be constant along the length of the fiber and the in situ matrix properties to be strongly dependent on the confining effects of fiber spacing, which was also taken to be constant along the length of the fibers.

The samples were drawn from the distributions determined from the MCMC calibration procedure. For each length scale parameter considered, 20 random, spatially varying parameter fields were generated and the EHM model was exercised to predict the ultimate failure for each realization. The resulting mean and standard deviation of the ultimate failure strength in the quasi-isotropic open hole coupon under tension at the slow loading rate is presented in Fig. 5.29. The

Figure 5.26: Images of Failure from $[+45, 0, -45, 90]_{2S}$ Quasi-Isotropic Open Hole Tension Tests at 1.0 mm/min and 100 mm/min.

sampling width does not have a significant impact on the mean failure strength of the coupon. However, there is a pronounced effect on the standard deviation of predicted failures. For realizations with a high sampling length, i.e. the parameters fluctuate at a lower frequency over the realization, the standard deviation is larger than the realizations with more rapidly fluctuating parameters. A logarithmic fit line for the standard deviation as a function of sampling length is included in Fig. 5.29(b).

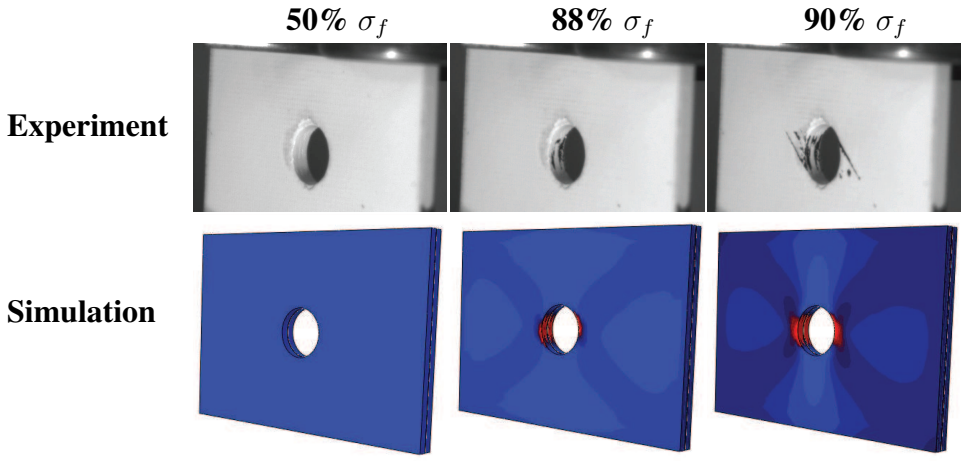

Figure 5.27: Evolution of Damage at 1mm/min

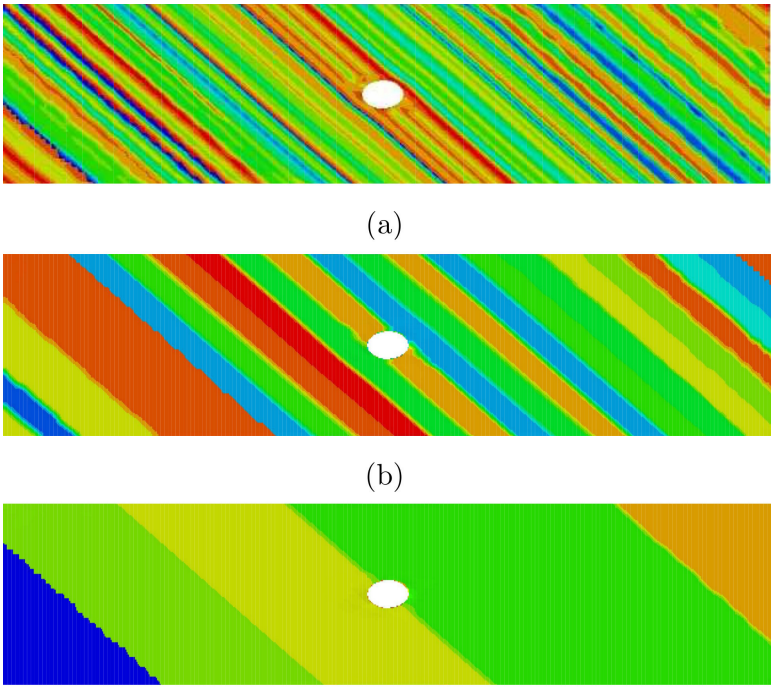

Figure 5.28: Sampled Parameter Groups for Spatial Variability with l_r = (a) 1mm, (b) 5mm, (c) 20mm

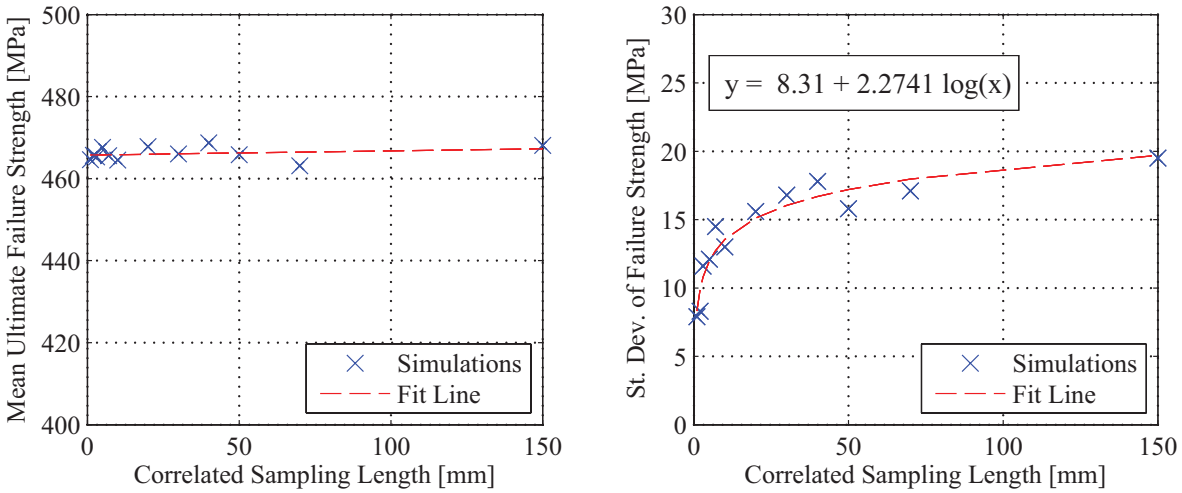

Figure 5.29: (a) Mean and (b) Standard Deviation of Ultimate Failure Strength as a Function of the Length of Correlated Sampling.

Chapter 6

FUTURE WORK AND CONCLUSIONS

6.1 Future Work

While the EHM approach implemented in the DTDP program performed well in the prediction of both static and fatigue behavior under a number of loading conditions, significant opportunities persist for improving the capabilities of this method. Additional experimental results on symmetric off-axis laminates would help to provide more precise fundamental understanding on the manner in which damage evolution in the composite is effected by mixed-mode loading behaviors and shed light onto additional damage mode interaction effect, particularly in the [60,0,-60]$_{3S}$ and [30,60,90,-60,-30]$_{2S}$ layups. Experimental data is available primarily for unidirectional or cross-ply, 0°, 90°, and 45° layups, but little data is available on configurations such as $[+30, -30]_{nS}$ or $[+60, -60]_{nS}$. An experimental investigation using these layups has been initiated at the AFRL to acquire this data, in part due to the recommendations of this research. From a modeling perspective, the manner in which delamination is addressed in the ROM could be further refined. Presently, when damage accumulates in the ROM part associated with delamination failure, a significant impact is observed on the stiffness of the RVE in the transverse direction. This effect is undesired as the development of delamination is a phenomenon localized to the ply interface. This could be alleviated by investigating new ROM partitions which use a thinner width of elements to represent the delamination part, such that the inelastic strain in the ROM due to delamination does not have as great of an influence on the transverse behavior.

An further opportunity for improvement is in the reduction of spurious residual forces present in the EHM model after part failure. Utilizing the concept of impotent eigenstrains in the formulation of additional sets of EHM coefficients to represent the post-failure state of the RVE could reduce the presence of residual stresses after failure. This would also permit the ROM to better

capture partial failure modes in the microscale, such as the case where delamination has occurred whilst the in-plane stiffness is preserved, or where the matrix material has failed while the fiber remains unbroken. The localization and kinematics of failure need to also be addressed using a macro-element approach. Currently the use of CDM in the EHM approach leads to mesh size dependence and mesh alignment bias in the failure of laminated composite specimens. Utilizing finite element formulations with enriched bases or a novel quadrature scheme in the formulation of elements to account for delamination and the localization of damaged regions would significantly improve the predictive capability of the EHM approach and also provide a means to predicting distinct cracks. Work has begun in this arena for composites such as the mesh independent cracking network proposed by Iarve et al. [48], cohesive zone models by Li et al. [58], or virtual crack closure technique [54]. The methods currently rely on analytical models of composite response to govern the behavior of discrete cracking events. The EHM framework could be leveraged in conjunction with these macroscale methods to provide higher fidelity representations of the microscale behavior governing the discrete cracks.

In addition to improving the mechanics of the EHM model, the application of the Bayesian calibration scheme presented could be extended to further applications in the prediction of composite response. One potential opportunity for future works would be the application of the Bayesian calibration approach of underlying material parameters over a larger set of experimental data, such as the data set provided in the DTDP program. Not only would the calibration require the consideration of additional interdependent material parameters, the verification and validation of the method would be strengthened by the additional number of experiments that EHM model is exercised in predicting. Calibration of random material parameters in this context would also move towards providing the methodology for developing a comprehensive design approach for composite materials considering the reliability of laminated composite components. In order to adequately account for uncertainty in the composite material system from sources beyond just material parameter uncertainty, more robust calibration techniques could be applied. Bayesian networks could be employed to extend the uncertainty quantification framework to consider uncertainty from addi-

tional scales, such as fiber alignment, fiber volume fraction, statistically representative volumes instead of unit cells, and ply thickness variability.

6.2 Conclusions

The developments presented in this dissertation present a meaningful addition to the state of the art in the prediction of the mechanical behavior of advanced composite materials, both from a deterministic and a probabilistic perspective. The goal of this dissertation was to demonstrate new fundamental understanding on the way in which microscale failure is propagated to macroscale discrete failure events in FRP composites, predict the monotonic and fatigue response of composites using the EHM approach, and quantify the effect of random constituent material properties of FRP composites on effective composite properties and laminated composite behavior. The inherent tension/compression anisotropy of stiffness exhibited in the unidirectional tape of many FRP composite materials was addressed using the new dual-ROM approach. A novel approach to predicting damage evolution under both uniaxial and shear-dominate loading conditions was presented using parameter weighting to modify the resulting ductility of the stress-strain relationship was also presented. These new predictive methods were employed in predicting a wide range of IM7/977-3 layups with open hole and unnotched configurations under tension, compression, and tension-tension fatigue in the DTDP program. These cases exhibited failure modes dominated by fiber breakage, matrix cracking from normal and shear-dominated failure, delamination, and combinations of these modes. The resulting predictions of the EHM from the DTDP program were in good agreement, both quantitatively and qualitatively, with the experimental data. This demonstrates the effectiveness of the model improvements presented herein. Additionally, the significant computational savings achieved by implementing EHM using parallel computational capabilities as opposed to the previous serial implementation were essential to providing predictions promptly and on the tight time schedule of the DTDP program.

The propagation of randomness across the scales of composites using Bayesian calibration of constituent parameters for S2-glass composites and IM7/977-3 carbon fiber composites con-

sidering rate-dependent failure behavior successfully quantified the effect of random constituent material properties of FRP composites on effective composite properties and laminated composite behavior. This work represented the first application of Bayesian parameter calibration to the prediction of laminated composite response using a CH based approach and is amongst the few published investigations directed towards the calibration of underlying material parameters as opposed to propagating probabilistic effects to larger scales from assumed parameter distributions. Overall the new contributions to both the prediction of physical behavior using multiscale computational mechanics and the quantification of uncertainty using Bayesian statistical methods provide new methods for the prediction of laminated composite behavior.

BIBLIOGRAPHY

[1] J. Aboudi. Micromechanical analysis of composites by the method of cells. *Appl. Mech. Rev.*, 42:193–221, 1989.

[2] J. Aboudi. The effect of evolving damage on the finite strain response of inelastic and viscoelastic composites. *Materials*, 2:1858–1894, 2009.

[3] R. K. Abu Al-Rub and R. K. Voyiadjis. A finite strain plastic-damage model for high velocity impact using combined viscosity and gradient localization limiters: Part i - theoretical formulation. *Int. J, Damage Mech.*, 15:293–334, 2006.

[4] J. Aronhime, H. Harel, A. Gilbert, and G Marom. The rate-dependence of flexural shear fatigue and uniaxial compression of carbon- and aramid-fibre composites and hybrids. *Compos. Part A-Appl. S.*, 43:105–116, 1992.

[5] ASTM Standard 3039. Standard test method for tensile properties of polymer matrix composite materials. ASTM International, West Conshohocken, PA, 2008.

[6] ASTM Standard 3518. Standard test method for in-plane shear response of polymer matrix composite materials by tensile test of a +/-45° laminate. ASTM International, West Conshohocken, PA, 2007.

[7] ASTM Standard 7078. Standard test method for shear properties of composite materials by v-notched rail shear method. ASTM International, West Conshohocken, PA, 2005.

[8] ASTM Standard D3410. Standard test method for compressive properties of polymer matrix composite materials with unsupported gage section by shear loading. ASTM International, West Conshohocken, PA, 2008.

[9] ASTM Standard D5528. Standard test method for mode i interlaminar fracture toughness

of unidirectional fiber-reinforced polymer matrix composites. ASTM International, West Conshohocken, PA, 2007.

[10] ASTM Standard D5766. Standard test method for open-hole tensile strength of polymer matrix composite laminates. ASTM International, West Conshohocken, PA, 2011.

[11] ASTM Standard D790. Standard test methods for flexural properties of unreinforced and reinforced plastics and electrical insulating materials. ASTM International, West Conshohocken, PA, 2010.

[12] I. Babuska. Homogenization and application. mathematical and computational problems. In B. Hubbard, editor, *Numerical Solution of Partial Differential Equations - III, SYNSPADE*. Academic Press, 1975.

[13] A. Benssousan, J. L. Lions, and G. Papanicolaou. *Asymptotic Analysis for Periodic Structures*. North-Holland, Amsterdam, 1978.

[14] M. J. Bogdanor, S. Mahadevan, and C. Oskay. Uncertainty quantification in damage modeling of heterogeneous materials. *Int. J. Multiscale Comp. Eng.*, 11:287–307, 2013.

[15] M.J. Bogdanor, R.D. Crouch, S.B. Clay, and C. Oskay. Modeling rate dependent damage evolution in composite structures. *Proceedings of the 54th AIAA Structures, Structural Dynamics, and Materials*, 2013.

[16] M.J. Bogdanor, , and C. Oskay. Application of reduced order multiscale homogenization to assess and quantify the benefits of applying damage tolerant design principles to advanced composite aircraft structures. *Proceedings of the 56th AIAA Structures, Structural Dynamics, and Materials*, 2015.

[17] M.J. Bogdanor, C. Oskay, and S.B. Clay. Multiscale modeling of failure in composites under model parameter uncertainty. *Comput. Mech.*, 56:389–404, 2015.

[18] M.J. Bogdanor, , and C. Oskay. Prediction of progressive damage and strength of im7/977-3 composites using the eigendeformation based homogenization approach: Static loading. *J. Compos. Mater.*, In Progress.

[19] M.J. Bogdanor, , and C. Oskay. Prediction of progressive damage and strength of im7/977-3 composites using the eigendeformation based homogenization approach: Fatigue loading. *J. Compos. Mater.*, In Progress.

[20] J. L. Chaboche. Continuum damage mechanics: Present state and future trends. *Nucl. Eng. Des.*, 105:19–33, 1987.

[21] J.L. Chaboche. Continuum damage mechanics: Part I - general concepts. *J. Appl. Mech.*, 55:59–64, 1988.

[22] C. C. Chamis. Failure criteria for filamentary composites. Technical report, DTIC Document, 1969.

[23] C. C. Chamis. Probabilistic simulation of multi-scale composite behavior. *Theor. Appl. Fract. Mec.*, 41:51–61, 2004.

[24] H.S. Chen, S.F. Hwang, and H.S. Chen. Accelerated fatigue properties of unidirectional carbon/epoxy composite materials. *Polym. Compos.*, pages 138–146, 2006.

[25] A. Clement, C. Soize, and J. Yvonnet. Uncertainty quantification in computational stochastic multiscale analysis of nonlinear elastic materials. *Comput. Meth. Appl. Mech. Eng.*, 254: 61–82, 2013.

[26] R. Crouch and C. Oskay. Symmetric mesomechanical model for failure analysis of heterogeneous materials. *Int. J. Multiscale Comp. Eng.*, 8:447–461, 2010.

[27] R. Crouch and C. Oskay. Experimental and computational investigation of progressive damage accumulation in CFRP composites. *Compos. Part B-Eng.*, 48:59–67, 2013.

[28] R. Crouch and C. Oskay. Accelerated time integrator for multiple time scale homogenization. *Int. J. Numer. Meth. Eng.*, 101:1019–1042, 2015.

[29] R. Crouch, C. Oskay, and S. Clay. Multiple spatio-temporal scale modeling of composites subjected to cyclic loading. *Comput. Mech.*, 2013.

[30] G. J. Dvorak. Transformation field analysis of inelastic composite materials. *Proc. Roy. Soc. London Ser. A*, 437:311–327, 1992.

[31] G.J. Dvorak, A.M. Wafa, and Y.A. Bahei-El-Din. Implementation of the transformation field analysis for inelastic composite materials. *Comput. Mech.*, 14:201–228, 1994.

[32] M. M. S. Dwaikat, C. Spitas, and V. Spitas. Effect of the stochastic nature of the constituents parameters on the predictability of the elastic properties of fibrous nano-composites. *Compos. Sci. Technol.*, 2012.

[33] T.R. Emery, J.M. Dulieu-Barton, J.S. Earl, and P.R. Cunningham. A generalized approach to the calibration of orthotropic materials for thermoelastic stress analysis. *Compos. Sci. Technol.*, 68:743–752, 2008.

[34] J. Fish. *Practical multiscaling*. John Wiley & Sons, 2013.

[35] J. Fish and Q. Yu. Computational mechanics of fatigue and life predictions for composite materials and structures. *Comput. Meth. Appl. Mech. Eng.*, 191:4827–4849, 2002.

[36] J. Fish, K. Shek, M. Pandheeradi, and M. S. Shephard. Computational plasticity for composite structures based on mathematical homogenization: Theory and practice. *Comput. Meth. Appl. Mech. Eng.*, 148:53–73, 1997.

[37] D. Geman and S. Geman. Stochastic relaxation, gibbs distributions, and the bayesian restoration of images. *IEEE Trans. Pattern Anal. Machine Intell.*, 14:721–741, 1984.

[38] S. Ghosh. *Micromechanical analysis and multi-scale modeling using the Voronoi cell finite element method*. CRC Press, 2011.

[39] A. Gilat, R. K. Goldberg, and G. D. Roberts. Strain rate sensitivity of epoxy resin in tensile and shear loading. *J. Aero. Eng.*, 2007.

[40] M. S. Greene, H. Xu, S. Tang, W. Chen, and W. K. Liu. A generalized uncertainty propagation criterion from benchmark studies of microstructured material systems. *Comput. Meth. Appl. Mech. Eng.*, 254:271–291, 2013.

[41] Z. Hashin and S. Shtrikman. A variational approach to the theory of the effective magnetic permeability of multiphase materials. *J. Appl. Phys.*, 33:3125–3131, 1962.

[42] W.K. Hastings. Monte carlo sampling methods using markov chains and their applications. *Biometrika*, 57:97, 1970.

[43] R1 Hill. A self-consistent mechanics of composite materials. *Journal of the Mechanics and Physics of Solids*, 13:213–222, 1965.

[44] O. Hoffman. The brittle strength of orthotropic materials. *Journal of Composite Materials*, 1:200–206, 1967.

[45] V. Hombal and S. Mahadevan. Bias minimization in gaussian process surrogate modeling for uncertainty quantification. *Int. J. Uncertain. Quantif.*, 1:321–349, 2011.

[46] T. Y. Hou and X.-H. Wu. A multiscale finite element method for elliptic problems in composite materials and porous media. *J. Comput. Phys.*, 134:169–189, 1997.

[47] T. Hui and C. Oskay. Computational modeling of polyurea-coated composites subjected to blast loads. *J. Compos. Mater.*, 46:2167–2178, 2012.

[48] E. V. Iarve, M. R. Gurvich, D. H. Mollenhauer, C. A. Rose, and C. G. Davila. Mesh-independent matrix cracking and delamination modeling in laminated composites. *Int. J. Numer. Meth. Eng.*, 88:749–773, 2011.

[49] L. Kachanov. *Introduction to continuum damage mechanics*, volume 10. Springer Science & Business Media, 2013.

[50] M. Kamiński and M. Kleiber. Perturbation based stochastic finite element method for homogenization of two-phase elastic composites. *Comput. Struct.*, 78:811–826, 2000.

[51] M.C. Kennedy and A. O'Hagan. Bayesian calibration of computer models. *J. Roy. Stat. Soc. B*, 63:425–464, 2001.

[52] V. G. Kouznetsova. *Computational Homogenization for the multi-scale Analysis of multi-phase materials*. 2002.

[53] A. Krishnan and C. Oskay. Modeling compression-after-impact response of polymer matrix composites subjected to seawater aging. *J. Compos. Mater.*, 46:2851–2861, 2012.

[54] R. Krueger. Virtual crack closure technique: history, approach, and applications. *Appl. Mech. Rev.*, 57:109–143, 2004.

[55] D.J. Lekou and T.P. Philippidis. Mechanical property variability in FRP laminates and its effect on failure prediction. *Compos. Part B-Eng.*, 39:1247–1256, 2008.

[56] J. Lemaitre. *A course on damage mechanics*. Springer Science & Business Media, 2012.

[57] J. Lemaitre and J.L. Chaboche. *Mechanics of Solid Materials*. Cambridge University Press, 1994.

[58] S. Li, M. D. Thouless, A. M. Waas, J. A. Schroeder, and P. D. Zavattieri. Use of mode-I cohesive-zone models to describe the fracture of an adhesively-bonded polymer-matrix composite. *Compos. Sci. Technol.*, 65:281–293, 2005.

[59] B. Liang and S. Mahadevan. Error and uncertainty quantification and sensitivity analysis in mechanics computational models. *Int. J. Uncertain. Quantif.*, 1:147–161, 2011.

[60] S. C. Lin. Reliability predictions of laminated composite plates with random system parameters. *Probab. Eng. Mech.*, 15:327–338, 2000.

[61] J. D. Littell, C. R. Ruggeri, R. K. Goldberg, G. D. Roberts, W. A. Arnold, and W. K. Binienda. Measurement of epoxy resin tension, compression, and shear stress–strain curves over a wide range of strain rates using small test specimens. *J. Aero. Eng.*, pages 162–173, 2008.

[62] P.A.M. Lopes, H.M. Gomes, and A.M. Awruch. Reliability analysis of laminated composite structures using finite elements and neural networks. *Compos. Struct.*, 92:1603–1613, 2010.

[63] N. Metropolis, A.W. Rosenbluth, M.N. Rosenbluth, A.H. Teller, and E. Teller. Equation of state calculations by fast computing machines. *J. Chem. Phys.*, 21:1087–1092, 1953.

[64] C. Miehe, J. Schröder, and J. Schotte. Computational homogenization analysis in finite plasticity simulation of texture development in polycrystalline materials. *Comput. Meth. Appl. Mech. Eng.*, 171:387–418, 1999.

[65] T Mori and K Tanaka. Average stress in matrix and average elastic energy of materials with misfitting inclusions. *Acta Metall.*, 21:571–574, 1973.

[66] R.M. Neal. Slice sampling. *Ann. Stat.*, 31:705–767, 2003.

[67] J. A. Nelder and R. Mead. A simplex method for function minimization. *Comput. J.*, 7: 308–313, 1965.

[68] C. Oskay. Two-level multiscale enrichment methodology for modeling of heterogeneous plates. *Int. J. Numer. Meth. Eng.*, 80:1143–1170, 2009.

[69] C. Oskay and J. Fish. Fatigue life prediction using 2-scale temporal asymptotic homogenization. *Int. J. Numer. Meth. Eng.*, 61:329–359, 2004.

[70] C. Oskay and J. Fish. Eigendeformation-based reduced order homogenization for failure analysis of heterogeneous materials. *Comput. Meth. Appl. Mech. Eng.*, 196:1216–1243, 2007.

[71] C. Oskay and J. Fish. On calibration and validation of eigendeformation-based multiscale models for failure analysis of heterogeneous systems. *Comput. Mech.*, 42:181–195, 2008.

[72] C. Oskay and G. Pal. A multiscale failure model for analysis of thin heterogeneous plates. *Int. J. Damage Mech.*, 19:575–610, 2009.

[73] M. H. J. W. Paas, P. J. G. Schreurs, and W. A. M. Brekelmans. A continuum approach to brittle and fatigue damage: Theory and numerical procedures. *Int. J. Solids. Struct.*, 30: 579–599, 1993.

[74] Ill Kyung Park, Kook Jin Park, and Seung Jo Kim. Rate-dependent damage model for polymeric composites under in-plane shear dynamic loading. *Comput. Mater. Sci.*, 96:506–519, 2015.

[75] E. Parzen. On estimation of a probability density function and mode. *Ann. Math. Stat.*, 33: 1065–1076, 1962.

[76] J. Raghavan and M. Meshii. Time-dependent damage in carbon fibre-reinforced polymer composites. *Compos. Part A-Appl. S.*, 27:1223–1227, 1996.

[77] C. Rasmussen and C. Williams. *Gaussian Processes for Machine Learning*. Springer, New York, 2006.

[78] K. L. Reifsnider. The critical element model - a modeling philosophy. *Eng. Fract. Mech.*, 25:739–749, 1986.

[79] P.M. Reilly and H. Patino-Leal. A bayesian study of the error-in-variables model. *Technometrics*, 23:221–231, 1981.

[80] M. Rosenblatt. Remarks on some nonparametric estimates of a density function. *Ann. Math. Stat.*, 27:832–837, 1956.

[81] S. Sakata, F. Ashida, T. Kojima, and M. Zako. Three-dimensional stochastic analysis using a perturbation-based homogenization method for elastic properties of composite material considering microscopic uncertainty. *Int. J. Solids Struct.*, 45:894–907, 2008.

[82] S. Sakata, F. Ashida, and M. Zako. Kriging-based approximate stochastic homogenization analysis for composite materials. *Comput. Meth. Appl. Mech. Eng.*, 197:1953–1964, 2008.

[83] S. Sakata, F. Ashida, and K. Enya. Stochastic analysis of microscopic stress in fiber reinforced composites considering uncertainty in a microscopic elastic property. *J. Solid Mech. Mater. Eng.*, pages 568–577, 2010.

[84] M. Salavatian and L.V. Smith. An investigation of matrix damage in composite laminates using continuum damage mechanics. *Compos. Struct.*, 131:565 – 573, 2015.

[85] E. Sanchez-Palencia. *Non-homogeneous media and vibration theory*, volume 127 of *Lecture notes in physics*. Springer-Verlag, Berlin, 1980.

[86] S. Sankararaman. *Uncertainty Quantification and Integration in Engineering Systems*. PhD thesis, Vanderbilt University, 2012.

[87] S. Sankararaman, Y. Ling, and S. Mahadevan. Uncertainty quantification and model validation of fatigue crack growth prediction. *Eng. Fract. Mech.*, 78:1487–1504, 2011.

[88] A. Shaw, S. Sriramula, P. D. Gosling, and M. K. Chryssanthopoulos. A critical reliability evaluation of fibre reinforced composite materials based on probabilistic micro and macro-mechanical analysis. *Compos. Part B-Eng.*, 41:446–453, 2010.

[89] M. C. Shiao and C. C. Chamis. Probabilistic evaluation of fuselage-type composite structures. *Probab. Eng. Mech.*, 14:179–187, 1999.

[90] B. W. Silverman. *Density estimation for statistics and data analysis*, volume 26. CRC press, 1986.

[91] J. C. Simo and J. W. Ju. Strain- and stress-based continuum damage models - i. formulation. *Int. J. Solids. Struct.*, 23:821–840, 1987.

[92] K. Song, Y. Li, and C. A. Rose. Continuum damage mechanics models for the analysis of progressive failure in open-hole tension laminates. *52nd AIAA Structures Structural Dynamics and Materials Conference*, 1861:1–18, 2011.

[93] P. Sparks and C. Oskay. Identification of optimal reduced order homogenization models for failure and of heterogeneous and materials. *Int. J. Multiscale Comp. Eng.*, 2013.

[94] S. M. Spearing and P. W. R. Beaumont. Fatigue damage mechanics of composite materials. I: Experimental measurement of damage and post-fatigue properties. *Compos. Sci. Technol.*, 44:159–168, 1992.

[95] S. M. Spearing, P. W. R. Beaumont, and M.F. Ashby. Fatigue damage mechanics of composite materials. II: A damage growth model. *Compos. Sci. Technol.*, 44:169–177, 1992.

[96] S. Sriramula and M. K. Chryssanthopoulos. Quantification of uncertainty modelling in stochastic analysis of FRP composites. *Compos. Part A-Appl. S.*, 40:1673–1684, 2009.

[97] P. M. Suquet. Elements of homogenization for inelastic solid mechanics. In E. Sanchez-Palencia and A. Zaoui, editors, *Homogenization Techniques for Composite Media*. Springer-Verlag, 1987.

[98] K. Terada and N. Kikuchi. Nonlinear homogenization method for practical applications. In S. Ghosh and M. Ostoja-Starzewski, editors, *Computational Methods in Micromechanics*, volume AMD-212/MD-62, pages 1–16. ASME, 1995.

[99] S.V. Thiruppukuzhi and C.T. Sun. Models for the strain-rate-dependent behavior of polymer composites. *Compos. Sci. Technol.*, 61:1–12, 2001.

[100] M. Tootkaboni and L. Graham-Brady. A multi-scale spectral stochastic method for homogenization of multi-phase periodic composites with random material properties. *Int. J. Numer. Meth. Eng.*, 83:59–90, 2010.

[101] S. W. Tsai. Strength characteristics of composite materials. Technical report, DTIC Document, 1965.

[102] S. W. Tsai and E. M. Wu. A general theory of strength for anisotropic materials. *J. Compos. Mater.*, 5:58–80, 1971.

[103] G. Z. Voyiadjis. *Advances in Damage Mechanics: Metals and Metal Matrix Composites: Metals and Metal Matrix Composites*. Elsevier, 2012.

[104] H. Yan, C. Oskay, A. Krishnan, and L.R. Xu. Compression after impact response of woven fiber-reinforced composites. *Compos. Sci. Technol.*, 70:2128–2136, 2010.

[105] R. Zhang and S. Mahadevan. Model uncertainty and bayesian updating in reliability-based inspection. *Struct. Saf.*, 22:145–160, 2000.